New Physics Beyond the Standard Model with Weakly Interacting Particles

by

Chien-Yi Chen

Submitted in partial fulfillment of the
requirements for the degree of
Doctor of Philosophy
at
Carnegie Mellon University
Department of Physics
Pittsburgh, Pennsylvania

Advised by Professor Lincoln Wolfenstein

August 24, 2012

Abstract

In this thesis, two of the most exciting areas in high energy physics nowadays are studied: neutrino physics and collider physics, which play important roles in the intensity and energy frontiers, respectively.

For neutrino physics, assuming that the neutrino mass matrix is dominated by a term with the permutation symmetry S_3, it is possible to explain neutrino data only if the masses are quasi-degenerate. A sub-dominant term with an approximate $\mu - \tau$ symmetry leads to an approximate tri-bimaximal form. Experimental consequences are discussed.

In this thesis several channels that contain missing-energy signal in the final states will be investigated with minimal model assumptions. Channels of this type are very challenging to analyze at the Large Hadron Collider (LHC), since this approach offers only a few kinematical handles.

I start with a channel that has a clean signal of two leptons and missing energy. This signature generally arises from pair production of heavy charged particles which each decay into a lepton and a weakly interacting stable particle. This class of processes is analyzed with minimal model assumptions by considering all possible combinations of spin 0, $\frac{1}{2}$ or 1, and of weak iso-singlets, -doublets, or -triplets for the new particles. Adding to existing work on mass and spin measurements, two new variables for spin determination and an asymmetry for the determination of the couplings of the new particles are introduced. It is shown that these observables allow one to independently determine the spin and the couplings of the new particles, except for a few cases that turn out to be indistinguishable at the LHC. These findings are corroborated by results of an alternative analysis strategy based on an automated likelihood test.

I then study decays of the form $C \to \ell^+\ell^- A$ ($\ell = e, \mu$), including the possibility that this three-body decay is preceded by an additional decay step $D \to jC$. Here A, C and D are heavy new-physics particles and j stands for a quark jet. It is assumed that A escapes direct detection in a collider experiment, so that one cannot kinematically reconstruct the momenta of the new particles. Instead, information about their properties can be obtained from invariant-mass distributions of the visible decay products, *i. e.* the di-lepton ($\ell\ell$) and jet-lepton ($j\ell$) invariant-mass distributions. All possible spin configurations and renormalizable couplings of the new particles are considered, and explicit expressions for the invariant-mass distributions are derived, in a formulation that separates the coupling parameters from the spin and kinematic information. In a numerical analysis, it is shown how these properties can be determined independently from a fit to the $m_{\ell\ell}$ and $m_{j\ell}$ distributions.

Finally, I will take a model-independent approach to searching for new physics involving the top quark. The experimental signatures for new physics involving top

quarks at the LHC may be characteristic, yet challenging to disentangle. I systematically parameterize generic interactions of a new particle that couples to the top quark and optimize the search strategy for the new particles at the LHC and propose the study for their properties. Several variables are proposed and a detailed numerical study is performed for the determination of spins and couplings of new heavy particles.

Acknowledgments

First of all, I would like to express my sincerest gratitude to my advisor, Prof. Lincoln Wolfenstein, for his support, patience, and encouragement. He taught me how to explore the unknown and appreciate the beauty of physics. I enjoyed many stimulating discussions with him and thank him for always keeping his door open when I needed him. I am extremely grateful for his mentoring and advising. His guidance has been irreplaceable in my research and in my life.

Next, I would like to thank Prof. Ayres Freitas, who participated extensively in advising me. His intuitive insights and helpful suggestions assist me to shape out the research ideas and directions. In particular, I thank him for his will to listen to my wrong ideas and putting up with many of my dumb questions. I am greatly indebted to him for his continuous guidance and encouragement.

I am also privileged to work with Prof. Tao Han. He has enriched my understanding and broadened my vision in physics tremendously. I have also greatly benefited from his course, Collider Physics. I thank him for always giving me invaluable advices and encouragement when I have questions about my research.

Thanks are also due to other professors who I was fortunately able to interact with, Professors Daniel Boyanovsky, Roy Briere, Gregg Franklin, Richard Holman, Adam Leibovich, Ling-Fong Li, Manfred Paulini, Ira Rothstein, Eric Swanson for their helps and support during my Ph.D. study. Special thanks to Prof. Cheng-Wei Chiang and Prof. Otto Kong in Taiwan for bring me into contact with high energy physics community.

I would also like to thank my colleagues and friends, Aristotle Calamba, Philip Cheung, Mannie Chiu, Neil Christensen, Bhupal Dev, Haw Zan Goh, Yi-Cheng Huang, Jimmy Hutasoit, You-Cyuan Jhang, Doojin Kim, Wai Kin Lai, Keith Lee, Ye Li, Chang-You Lin, Xiao-Hui Liu, Zhen Liu, Duff Neill, Richard Ruiz, Zhen Tang, Ricy Wong, Jiang-Hao Yu, from whom I have learned a lot of physics. Many thanks to all my classmates and instructors in PreSUSY 2011 and TASI 2011 summer schools for many interesting discussions. I also thank the staff members in the Physics Department for taking care of all of the administrative works. Finally, I am also grateful to my parents and my sister for their understanding and unconditional love and support.

Contents

List of Tables

List of Figures

Chapter 1

Introduction

In this thesis, I will discuss two of the most exciting areas in high energy physics nowadays: neutrino physics and collider physics, which play important roles in the intensity [1] and energy frontiers [2], respectively.

Neutrino physics is one of the main focuses of intensity-frontier physics. Recent discoveries make the study of the properties of neutrinos an important area of research. Measurements of the properties of neutrinos are fundamental to understanding physics beyond the Standard Model (BSM) and have profound consequences for the evolution of the universe.

A lot of evidence for neutrino oscillations has been collected from various sources, including the sun, the atmosphere, accelerators and reactors. The effects of neutrino oscillations were first detected by Raymond Davis's Homestake Experiment [3] in the late 1960s. A deficit in the flux of solar neutrinos with respect to the prediction of the Standard Solar Model was observed based on a chlorine-based detector. This is called the solar neutrino problem. In 1998, Super-Kamiokande [4] in Japan, which utilized a large water Cherenkov detector, also found that neutrino fluxes were much below the values predicted by the Standard Solar Model. Later on, in 2001 the SNO experiment [5] in Canada used a heavy water Cherenkov detector to deliver the final confirmation of neutrino oscillations, which is not predicted by the standard model of particle physics.

Neutrino oscillation implies that the mass differences of neutrinos are non-zero and therefore neutrinos are massive particles. Recently, new results on θ_{13} have been announced by T2K [6], MINOS [7], and Double Chooz [8] in 2011, pointing to θ_{13} is not zero. More recently, Daya Bay [9] and RENO [10], announced about 5 σ evidence that $\sin^2 2\theta_{13} \simeq 0.092$. A non-zero value of θ_{13} has many profound implications for BSM physics, such as CP violation in the leptonic sector, and its relation to CP violation in the quark sector.

In this thesis, I will address two important questions in neutrino physics. One is how to explain neutrino oscillation data by assuming that the neutrino mass matrix obeys a discrete symmetry. The other is how to generate a non-zero θ_{13}. Furthermore,

its phenomenological consequences will be discussed.

With the discovery era ushered in by the LHC, data-driven phenomenology is now possible. Two detectors at the LHC, ATLAS and CMS, have collected large amounts of data and will be able to discover or rule out many of the new physics models such as supersymmetry, extra dimensions or strong-dynamics models. Model-independent searches become not only important but also pressing. I aim to find a systematic method to determine the properties of the new particles, such as masses, spins, and couplings. For the mass determination, there already exist good observables such as Cambridge M_{T2} [11] and its variants. Therefore, my focus is mainly on the spin and coupling determination. Spin determination is very important to distinguish one model from another because the new massive particles in these models may have different spins. For instance, supersymmetry predicts that the superpartner of SM leptons are scalars, *i.e.* they have spin equal to 0, while universal extra dimensions (UED) [12] predicts the Kaluza-Klein (KK) partner of leptons to be spin $\frac{1}{2}$ fermions. As a result, it is possible to distinguish supersymmetry from UED as long as one can discriminate the spins of these new particles. Coupling determination is also crucial because it can tell us the group representation of the new particles. For instance, if these particles have SU(2) symmetry, their couplings will depend on the SU(2) group representation of these particles, i.e. whether they are SU(2) singlets, doublets or triplets.

Motivated by the existence of cold dark matter, which accounts for 23% of the mass-energy density of the observable universe, many new-physics scenarios incorporate some global discrete symmetries to ensure the existence of a massive stable neutral particle. Well-known examples include R-parity in supersymmetry, KK-parity in UED models and T-parity in little Higgs models [13]. These stable neutral particles escape detection and hence become missing-energy signals of detectors. The existence of such a neutral particle at the end of the decay chain results in large missing-energy events in which new-physics particles are produced. The main focus of chapter 4, 5 and 6 will be on channels that contain missing-energy signals in the final states. Since such missing particles escape detectors, it is very difficult to fully reconstruct the energy and momenta of the final-state particles. Thus, determination of spin and couplings of heavy new particles in these channels is highly nontrivial and challenging.

In this thesis, I will investigate a few channels that contain missing particles in the final states. The first channel that I am interested in involves signals with two leptons and missing energy at the LHC. I focus on Drell-Yan–type production of a pair of charged heavy particles $Y^{\pm}$, which each subsequently decay into a lepton $\ell^{\pm}$ ($\ell = e, \mu$), and a neutral heavy particle X^0, i.e. $pp \to Y^+Y^- \to \ell^+\ell^- X^0 \bar{X}^0$, where p stands for a proton. I then considered all possible spin and SU(2) representations of new particles X and Y. The second channel to be discussed is the decay chain with three-body decays involving missing energy. Decays of the form $C \to \ell^+\ell^- A$ ($\ell = e, \mu$) are studied, including the possibility that this three-body decay is preceded

by an additional decay step $D \to jC$. Here A, C and D are heavy new-physics particles and j stands for a quark jet. It is assumed that A leads to missing energy in the detector so that one cannot kinematically reconstruct the momenta of the new particles. Instead, information about their properties can be obtained from invariant-mass distributions of the visible decay products, *i. e.* the di-lepton ($\ell\ell$) and jet-lepton ($j\ell$) invariant-mass distributions. I have developed a framework for extracting the mass of the intermediate particle and the spin and couplings of new particles.

Finally, I will take a model-independent approach to searching for new physics involving the top. Recent results from LHC [14] have rather stringently excluded a large part of the squark and gluino parameter space. However, it is possible that not all the squarks are at the same mass scale. In a typical supersymmetric grand unification theory (GUT), the squark that is the partner of the heaviest SM quark runs fastest in renormalization group evolution (RGE) and hence becomes lightest at the low-energy scale. As a result, the stop can be much lighter than other squarks. I consider the possibility that stop decays into top and the lightest neutralino dominates over other channels. The final-state signal in this scenario would be the decay product of top quarks and missing energy. We extend this idea to a model-independent approach by considering different spin configurations (0, 1/2, and 1) of a light new particle pair-produced in pp collisions to determine how one can distinguish between different scenarios and extract the spin of the new particles.

In the next section I will review the standard model of particle physics and also introduce notations that will be used in the following chapters.

1.1 The Standard Model

Despite the fact that the Standard Model (SM) has been so successful in agreeing with experimental data, many people believe that it is not complete for reasons I will explain in the next section. The SM accounts for our current understanding of strong, electromagnetic, and weak interactions based on a gauge symmetry $SU(3)_C \times SU(2)_L \times U(1)_Y$. Each gauge group associates with its own gauge bosons, which mediate forces between particles.

The Lagrangian for these gauge boson is

$$\mathcal{L}_{\text{gauge}} = -\frac{1}{4}(G_a^{\mu\nu} G_{a\,\mu\nu} + W_a^{\mu\nu} W_{a\,\mu\nu} + B^{\mu\nu} B_{\mu\nu}) \tag{1.1}$$

where

$$G_a^{\mu\nu} \equiv \partial^\mu G_a^\nu - \partial^\nu G_a^\mu - g_3\, f_{abc}\, G_b^\mu\, G_c^\nu \tag{1.2}$$

$$W_a^{\mu\nu} \equiv \partial^\mu W_a^\nu - \partial^\nu W_a^\mu - g_2\, \epsilon_{abc}\, W_b^\mu\, W_c^\nu \tag{1.3}$$

$$B^{\mu\nu} \equiv \partial^\mu B^\nu - \partial^\nu B^\mu \tag{1.4}$$

with eight $SU(3)_C$ gluon fields G_a^ν and three $SU(2)_L$ isotriplet bosons W_a^ν and $U_Y(1)$ hypercharge boson B^μ. f_{abc} and ϵ_{abc} are structure constants of the $SU(3)_C$ and

Names		SM fermions	$SU(3)_C$, $SU(2)_L$, $U(1)_Y$
Quarks	Q^I	$(u_L^I \quad d_L^I)$	$(\mathbf{3}, \mathbf{2}, \frac{1}{6})$
($\times$3 families)	u^I	u_R^I	$(\mathbf{3}, \mathbf{1}, \frac{2}{3})$
	d^I	d_R^I	$(\mathbf{3}, \mathbf{1}, -\frac{1}{3})$
Leptons	L^I	$(\nu^I \quad e_L^I)$	$(\mathbf{1}, \mathbf{2}, -\frac{1}{2})$
($\times$3 families)	e^I	e_R^I	$(\mathbf{1}, \mathbf{1}, -1)$

Table 1.1: *Fermion content of the Standard Model.*

$SU(2)_L$ groups, respectively. g_3 and g_2 are coupling constants of the $SU(3)_C$ and $SU(2)_L$ groups, respectively. The Lagrangian for the fermionic sector is

$$\mathcal{L}_{\text{fermion}} = i\bar{Q}_L^I \gamma^\mu D_\mu Q_L^I + i\bar{L}_L^I \gamma^\mu D_\mu L_L^I + i\bar{u}_R^I \gamma^\mu D_\mu u_R^I + i\bar{d}_R^I \gamma^\mu D_\mu d_R^I + i\bar{\ell}_R^I \gamma^\mu D_\mu \ell_R^I, \quad (1.5)$$

where the superscript I indicates that the fermion fields are in the interaction eigenstates. Also, the generation indices are suppressed for simplicity and the particle contents and the corresponding quantum numbers are summarized in Table 1.1. In order to ensure that the Lagrangian is gauge invariant, the covariant derivative is introduced and defined as

$$D^\mu = \partial^\mu + ig_3\, G_a^\mu \frac{\lambda_a}{2} + ig_2\, W_a^\mu \frac{\sigma_a}{2} + ig_1\, B^\mu Y, \quad (1.6)$$

where λ_a and σ_a are Gell-Mann and Pauli Matrices, respectively. The SM gauge group is broken down to $SU(3)_C \times U(1)_{EM}$ due to the Higgs mechanism, which I will explain in detail below.

The Lagrangian for the scalar sector is

$$\mathcal{L}_{\text{scalar}} = (D_\mu H)^\dagger\, D^\mu H + \mu^2 H^\dagger H - \frac{\lambda}{4}(H^\dagger H)^2, \quad (1.7)$$

where H is a scalar doublet field, also called the Higgs field.

$$H = \begin{pmatrix} H^+ \\ H^0 \end{pmatrix}. \quad (1.8)$$

After the spontaneous symmetry breaking in the Higgs potential, the Higgs field acquires a vacum expectation value (VEV)

$$< H >= \begin{pmatrix} 0 \\ \frac{v}{\sqrt{2}} \end{pmatrix} \text{ and } v = \sqrt{\frac{\mu^2}{\lambda}}. \quad (1.9)$$

The mass terms of gauge bosons come from the first term of $\mathcal{L}_{scalar}$, which is proportional to

$$\frac{v^2}{8}(g_2|W^1 - iW^2|^2 + (g_1\, B_\mu - g_2 W_\mu^3)^2). \quad (1.10)$$

The mass eigenstates and eigenvalues of the charged gauge bosons are

$$W_\mu^\pm = \frac{W_\mu^1 \mp W_\mu^2}{\sqrt{2}}, \text{ with } \mathrm{M_{W^\pm}} = \frac{\mathrm{g_2}\, v}{2}. \tag{1.11}$$

The mass eigenstates and eigenvalues of neutral gauge bosons are

$$Z_\mu = \frac{-g_1 B_\mu + g_2 W_\mu^3}{\sqrt{g_1^2 + g_2^2}}, \text{ with } \mathrm{M_Z} = \frac{v}{2}\sqrt{\mathrm{g_1^2 + g_2^2}} \tag{1.12}$$

$$A_\mu = \frac{g_2 B_\mu + g_1 W_\mu^3}{\sqrt{g_1^2 + g_2^2}}, \text{ with } \mathrm{M_A} = 0. \tag{1.13}$$

Finally, the interaction between scalars and fermions, namely Yukawa interactions are given by

$$\mathcal{L}_{\text{Yukawa}} = -Y_{ij}^U\ \bar{Q}_{Li}^I\ \widetilde{H}\ u_{Rj}^I - Y_{ij}^D\ \bar{Q}_{Li}^I\ H\ d_{Rj}^I - Y_{ij}^L\ \bar{L}_{Li}^I\ H\ \ell_{Rj}^I + h.c., \tag{1.14}$$

where $\widetilde{H} = i\sigma_2 H^*$ and (i,j) are the usual family indices (going from 1 to 3). $\mathcal{L}_{\text{Yukawa}}$ leads to fermion mass terms after substituting the VEV in Eq. 1.9.

$$\mathcal{L}_{\text{Matter}} = -M_{ij}^U\ \bar{u}_{Li}^I\ \widetilde{H}\ u_{Rj}^I - M_{ij}^D\ \bar{d}_{Li}^I\ H\ d_{Rj}^I - M_{ij}^L\ \bar{\ell}_{Li}^I\ H\ \ell_{Rj}^I + h.c., \tag{1.15}$$

where $M_f = vY^f$. One can always diagonalize M_f by rotating the flavor eigenstates $f_{L,R}^I$ to the mass eigenstates $f_{L,R}$,

$$f_L = V_L^f f_L^I \tag{1.16}$$

$$f_R = V_R^f f_R^I. \tag{1.17}$$

This leads to a diagonal and real matrix

$$M_f^{diag} = V_L^f M_f V_R^{f\,\dagger}. \tag{1.18}$$

Using the mass eigenstates, the charged current interaction involving $W^\pm$ and quarks is

$$\mathcal{L}_{\text{CC}} = \frac{g_2}{\sqrt{2}}\ \bar{u}_{Li}\ \gamma^\mu\ V_{CKM\,ij}\ d_{Lj}\ W_\mu^+ + h.c., \tag{1.19}$$

where

$$V_{CKM} = V_{uL}\ V_{dL}^\dagger \tag{1.20}$$

is the Cabbibo-Kobayashi-Maskawa(CKM) mixing matrix, which is a unitary matrix and is the only origin of the CP violation phase in the SM if the neutrino masses are neglected. This unitary matrix consists of 9 real parameters (3 mixing angles and 6 phases). Since quarks are Dirac fields 5 phases can be absorbed by redefining phases

of the quark fields. Eventually, only 3 mixing angles and 1 phase, which is called the Dirac phase, have physical meaning. The matrix element of V_{CKM} is often written as

$$V_{CKM} = \begin{pmatrix} V_{ud} & V_{us} & V_{ub} \\ V_{cd} & V_{cs} & V_{cb} \\ V_{td} & V_{ts} & V_{tb} \end{pmatrix}. \tag{1.21}$$

In terms of three angles $\theta_{12}, \theta_{23}, \theta_{13}$ and one phase δ, one can parameterize the V_{CKM} as follows,

$$V_{CKM} = \begin{pmatrix} c_{12}c_{13} & s_{12}c_{13} & s_{13}e^{-i\delta} \\ -c_{23}s_{12} - c_{12}s_{23}s_{13}e^{i\delta} & c_{12}c_{23} - s_{12}s_{23}s_{13}e^{i\delta} & c_{13}s_{23} \\ s_{23}s_{12} - c_{12}c_{23}s_{13}e^{i\delta} & -c_{12}s_{23} - s_{12}c_{23}s_{13}e^{i\delta} & c_{23}c_{13} \end{pmatrix}, \tag{1.22}$$

where $s_{ij} \equiv \sin\theta_{\rm ij}, {\rm c_{ij}} \equiv \cos\theta_{\rm ij}$.

The matrix elements of CKM matrix can be measured by experiments. The general feature of V_{CKM} is that it is almost diagonal and the diagonal elements are approximately one. Also, it has very clear hierarchical structure and is almost symmetric. Based on these observations L. Wolfenstein [15] parametrized V_{CKM} using a different set of parameters: A, λ, ρ and η. Dropping terms above $\mathcal{O}(\lambda^3)$, one obtains

$$V_{CKM} \sim \begin{pmatrix} 1 - \frac{\lambda^2}{2} & \lambda & A\lambda^3(\rho - i\,\eta) \\ -\lambda & 1 - \frac{\lambda^2}{2} & A\lambda^2 \\ A\lambda^3(1 - \rho - i\,\eta) & -A\lambda^2 & 1 \end{pmatrix}. \tag{1.23}$$

where $\lambda \equiv s_{12} \approx 0.23$ is the sine of the Cabbibo angle and

$$A\,\lambda^2 \equiv s_{23} \tag{1.24}$$

$$A\,\lambda^3(\rho - i\,\eta) \equiv s_{13}\,e^{-i\delta}. \tag{1.25}$$

1.2 Problems with the SM

There are many problems that cannot be explained by the SM and one needs to resort to new physics models. In the following I will list some of these major problems, which motivate us to propose new physics.

- **Hierarchy Problem:** The fact that gravity is much weaker than other forces implies the existence of two vastly different energy scales: $\Lambda_{\rm Planck} \sim 1/\sqrt{G} = 10^{19}$ GeV where gravity gets strong, and the electroweak scale $\Lambda_{\rm EW} \sim \mathcal{O}(100$ GeV). G stands for Newton's constant. If the SM is a complete theory and holds all

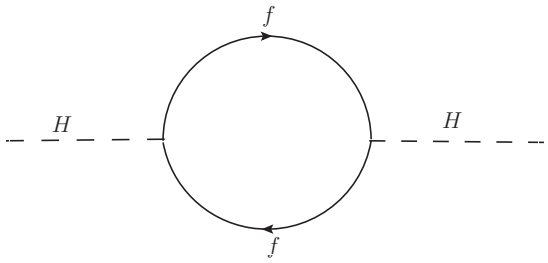

Figure 1.1: *One-loop correction to the Higgs (H) squared mass parameter m_H^2. f denotes a fermion field.*

the way up to the Planck scale, then one necessarily would have to deal with a fine-tuning problem in order to keep the mass of the Higgs light for reasons to be discussed later. The mass of the Higgs is subjected to large radiative correction, since it is a scalar particle. Unlike fermions, the scalar particle mass is not protected by chiral symmetry; the masses of the gauge bosons are protected by gauge symmetries. The physical Higgs mass m_H can be defined as

$$m_H^2 = m_0^2 + m_{rad}^2, \tag{1.26}$$

where m_0 represents bare mass and m_{rad} is the radiative correction to the Higgs mass. In the SM, Fig. 1.1 alone gives the largest correction to the Higgs mass,

$$m_{rad}^2 \;=\; -\frac{|Y^f|^2}{8\pi^2}(\Lambda_{UV}^2 - 3\; m_f^2\; ln\,\frac{\Lambda_{UV}}{m_f}), \tag{1.27}$$

which is quadratically divergent to the scale where new physics is believed to occur. Y^f is the Yukawa coupling in Eq. 1.14. The dominant contribution comes from the top quark in the loop in Fig. 1.1 since it has the largest Yukawa coupling to the Higgs boson. If the SM is a complete theory that is correct all the way up to the Planck scale, then it implies that in order to obtain a physical Higgs mass $m_H \simeq \Lambda_{\rm EW}$, m_0 must be of order $\Lambda_{\rm Planck}$. Since the ratio $\Lambda_{\rm EW}^2/\Lambda_{\rm Planck}^2 \simeq (100\,{\rm GeV}/10^{19}\,{\rm GeV})^2 = 10^{-34}$ is so small the cancellation must be extremely precise.

- **Gauge unification:** In the SM, there are three gauge couplings g_1, g_2, and g_3. Why are there so many gauge couplings instead of one? Can they be unified just like electromagnetic and weak interaction, which are unified at the electroweak scale? Some BSM models such as supersymmetry might be able to achieve it.

- **Dark matter:** Another problem that the SM cannot resolve is the dark matter problem. Many observations including the velocity curve of stars in galaxies and gravitational lensing studies of the Bullet Cluster provided strong evidence for

the existence of dark matter. We know that there must be something else that exists in addition to the matter that we observed. Many BSM models have proposed their own DM candidates, which will be discussed in more details in the next chapter.

Chapter 2

Physics beyond the Standard Model

In this thesis, I will utilize a model-independent approach to determine the spin and coupling of new heavy particles in some channels and only make minimal assumptions. However, there are some models that have been widely discussed in the literature and will be used as examples for my analyses. In this chapter I will discuss two of these BSM models, supersymmetry and UED models.

2.1 Minimal Supersymmetric Standard Model

Supersymmetry is one of the most promising BSM models. It can not only provide a solution to the hierarchy problem but also allows for the unification of gauge couplings. In addition, it also provides a candidate for dark matter. All these nice properties let many people believe that supersymmetry is too good not to be true. The original motivation of introducing supersymmetry, however, was not to resolve the hierarchy problem or all other nice features but was because of the Coleman-Mandula theorem [16], which shows the impossibility of combining space-time and internal symmetries in any but a trivial way. However, it can be circumvented by introducing symmetries whose algebra satisfy anti-commutation relations beyond the internal symmetries and the Poincare symmetry. In general, the number N of independent supersymmetric charges can be larger than 1 but in this thesis I will just discuss the minimal supersymmetric standard model (MSSM). In other words, only the case N=1 is considered.

The particle content of the MSSM is listed in Table 2.1 and Table 2.2. Every SM particle and their superpartner are denoted by the same notation except that the supersymmetric particle has an additional tilde $\tilde{}$. Supersymmetry describes the symmetry between fermions and bosons. The supersymmetric charge Q varies the

Names		spin 0	spin 1/2	$SU(3)_C$, $SU(2)_L$, $U(1)_Y$
squarks, quarks	Q	$(\widetilde{u}_L \;\; \widetilde{d}_L)$	$(u_L \;\; d_L)$	$(\mathbf{3}, \mathbf{2}, \frac{1}{6})$
	$\overline{u}$	$\widetilde{u}^*_R$	$u^\dagger_R$	$(\overline{\mathbf{3}}, \mathbf{1}, -\frac{2}{3})$
	$\overline{d}$	$\widetilde{d}^*_R$	$d^\dagger_R$	$(\overline{\mathbf{3}}, \mathbf{1}, \frac{1}{3})$
sleptons, leptons	L	$(\widetilde{\nu} \;\; \widetilde{e}_L)$	$(\nu \;\; e_L)$	$(\mathbf{1}, \mathbf{2}, -\frac{1}{2})$
	$\overline{e}$	$\widetilde{e}^*_R$	$e^\dagger_R$	$(\mathbf{1}, \mathbf{1}, 1)$
Higgs, higgsinos	H_u	$(H^+_u \;\; H^0_u)$	$(\widetilde{H}^+_u \;\; \widetilde{H}^0_u)$	$(\mathbf{1}, \mathbf{2}, +\frac{1}{2})$
	H_d	$(H^0_d \;\; H^-_d)$	$(\widetilde{H}^0_d \;\; \widetilde{H}^-_d)$	$(\mathbf{1}, \mathbf{2}, -\frac{1}{2})$

Table 2.1: *Chiral supermultiplets in the MSSM. The number of generations is three for fermions and sfermions.*

spin of the particle by 1/2.

$$Q|\text{boson}>=|\text{fermion}>\,;\;\text{Q}|\text{boson}>=|\text{fermion}> \tag{2.1}$$

Applying a supersymmetric operator on SM particles gives rise to their corresponding supersymmetric partners, whose spins differ from their SM partners by a half integer. The SM particles and their superpartners can be placed in a supermultiplet. There are two types of supermultiplets:

- Chiral supermultiplet: Each scalar particle in the SM has a fermion partner and together they form a chiral supermultiplet. Similarly, each SM fermion and their scalar partner are embedded in a chiral supermultiplet. Note that the left- and right-handed pieces of the quarks and leptons transform differently under the SM gauge groups so each must have its own complex scalar partner. For example in Table 2.1 a left-handed up quark u_L and its superpartner $\tilde{u}_L$ are in the same supermultiplet.

- Gauge supermultiplet: Each SM gauge boson and its superpartner are in one gauge supermultiplet. For instance, gluon and its superpartner gluino are embedded in the same gauge supermultiplet as shown in Table 2.2.

2.1.1 Motivation of introducing MSSM

As mentioned in the last chapter, the MSSM can solve the hierarchy problem. In the SM, the fermion loop diagram on the left hand side of Fig. 2.1 gives rise to m^2_{rad} in Eq. 1.27, which is quadratically divergent. However, in the MSSM there is an additional diagram as shown on the right hand side of Fig. 2.1 that also contributes to the quantum correction to the Higgs mass

$$m^2_{rad} \;\; = 2\,\tfrac{Y^{\tilde{f}}}{16\pi^2}(\Lambda^2_{UV} - 2\,\widetilde{m}^2_f\; ln\,\tfrac{\Lambda_{UV}}{\widetilde{m}_f}) \tag{2.2}$$

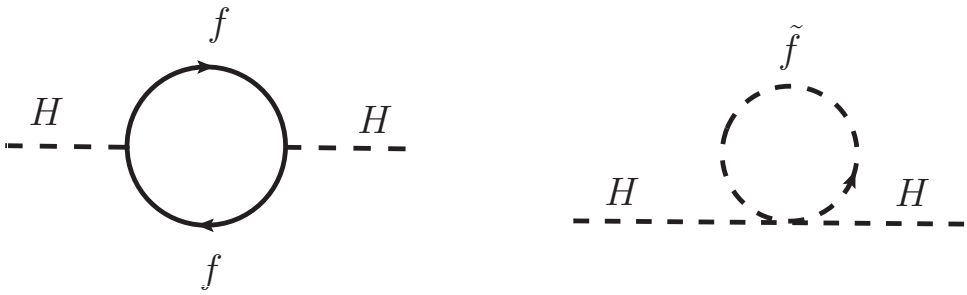

Figure 2.1: *One-loop correction to the Higgs (H) squared mass parameter m_H^2. The diagram on the left already exists in the SM. f denotes a fermion field. The diagram on the right is a new contribution from the MSSM. $\widetilde{f}$ represents a scalar fermion field. Two diagrams have opposite sign resulting in the cancellation of the UV divergence.*

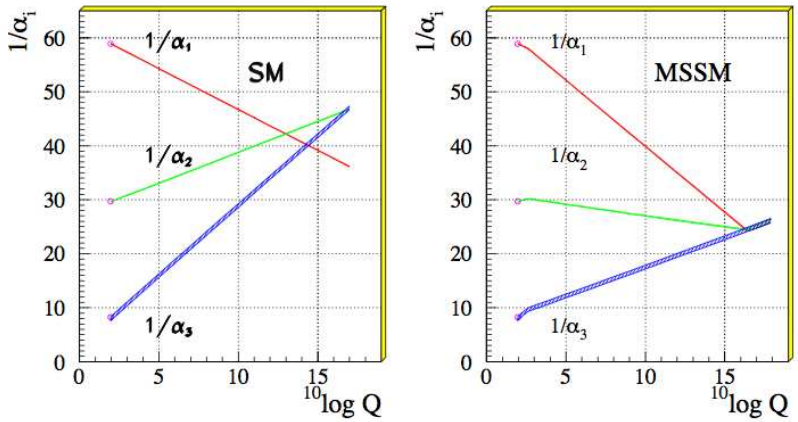

Figure 2.2: *The renormalization group evolution of the inverse gauge couplings $1/\alpha_1$, $1/\alpha_2$, and $1/\alpha_3$, which correspond to $U(1)_Y$, $SU(2)_L$, and $SU(3)_C$ gauge groups, in the SM (left) and MSSM (right). Q stands for RG scale. (This figure is taken from Ref. [17])*

Names	spin 1/2	spin 1	$SU(3)_C$, $SU(2)_L$, $U(1)_Y$
gluino, gluon	$\widetilde{g}$	g	(**8**, **1** , 0)
winos, W bosons	$\widetilde{W}^{\pm}$ $\widetilde{W}^{0}$	$W^{\pm}$ W^{0}	(**1**, **3** , 0)
bino, B boson	$\widetilde{B}^{0}$	B^{0}	(**1**, **1** , 0)

Table 2.2: *Gauge supermultiplets in the MSSM.*

where $Y^{\tilde{f}}$ stands for the coupling of the Higgs to the scalar fermions and $Y^{\tilde{f}} = |Y^{f}|^2$ due to the symmetry between fermions and bosons. It turns out in the MSSM, the two quadratic divergent terms cancel out and only the logarithmic terms survive. In order to keep the radiative corrections to the Higgs masses of order 100 GeV the mass of the scalar fermion $\widetilde{m}_f$ has to be less then 1 TeV. Note that due to the anticommutative nature of fermions, the sign of the fermion loop contribution is opposite to that of the scalar loop contribution. Moreover, the cancellation of quadratic divergences not only works in the MSSM but also in any supersymmetric theory.

In addition, in the MSSM the unification of the three gauge couplings of the SM at some high scale becomes possible. As can be seen in Fig. 2.2, in contrast to the SM the RG running of the three gauge couplings in the MSSM is changed due to the loop contributions from supersymmetric particles. It turns out that the three couplings unify at a scale $M_{GUT} \sim 2 \times 10^{16}$ GeV. However, for other supersymmetric theories the gauge-coupling unification depends on the details of the model.

2.1.2 Superpotential

The most general renormalizable superpotential with the spectrum of minimal superfields can be written as

$$\begin{aligned} W \;=\; & \varepsilon_{ab}\left[\mu H_u^a H_d^b + h_{ik}^u Q_i^a H_u^b \overline{u}_k + y_{jk}^d H_d^a Q_j^b \overline{d}_k + \frac{1}{2}\, y_{jk}^e H_d^a L_j^b \overline{e}_k\right] \\ & + \varepsilon_{ab}\left[\frac{1}{2}\lambda^{ijk} L_i L_j \overline{e}_k + \lambda'^{ijk} L_i Q_j \overline{d}_k + \mu'^i L_i H_u\right] + \frac{1}{2}\,\lambda''_{ijk}\overline{u}_i \overline{d}_j \overline{d}_k \;, \end{aligned} \tag{2.3}$$

where (a, b) are $SU(2)$ indices, (i, j, k) are the usual family (flavor) indices (going from 1 to 3). ε_{ab} is an antisymmetric tensor and $\varepsilon_{12} = -\varepsilon_{21} = 1$. The first line corresponds to baryon number and lepton number conservation terms while the first three terms of the second line break baryon number (B) by 1 and the last term breaks the lepton number (L) by 1. In the MSSM only terms in the first line is relevant in order to protect proton from decay. To exclude the baryon and lepton number violating terms a Z_2 symmetry called R-parity is introduced and defined as

$$P_R = (-1)^{3(B-L)+2S} \tag{2.4}$$

where S denotes the spin of the particle. The baryon number assignment are B=1 for Q_i , B=-1 for $\overline{u}_i$ and $\overline{d}_i$, and B=0 for all others. The lepton number assignments are L = 1 for L_i, L = -1 for $\overline{e}$, and L=0 for all others. All ordinary particles have even R-parity; all supersymmetric partners have odd R-parity. R-parity can not only prevent proton decay but also it ensures that supersymmetric particles are produced in pairs at colliders and that the lightest supersymmetric particle (LSP) is stable. If the LSP is not only stable but also electrically and color neutral it interacts only weakly with the SM particles. Therefore it might be a good dark matter candidate. For example, the lightest neutralino $\tilde{\chi}_1^0$ is an attractive dark matter candidate in many supersymmetric models.

2.1.3 Soft supersymmetry breaking terms

Since we have not yet found any supersymmetric particles, supersymmetry must be broken at some higher energy scale above the electroweak scale. We know that the particle responsible for the supersymmetry breaking cannot be particle content of the MSSM due to the existence of mass sum rules [18]. Hence the origin of supersymmetry breaking is often transferred to a hidden sector of particles that do not interact directly with MSSM particles. Therefore how to construct a realistic supersymmetry breaking scenario and understand the mechanism of the supersymmetry breaking mediation from hidden sector to visible sector become important. Many models usually assume that there is a messenger field that communicates between the hidden sector and the visible sector. More realistic models will be discussed in the Sec. 2.1.5. However, it is possible to simply add the explicit supersymmetry breaking terms in the effective MSSM Lagrangian. The non-renormalization theorem [19] requires that the supersymmetry-breaking coupling should be soft, *i.e.* the couplings must have positive mass dimension, to ensure that there is no quadratic divergent term similar to Eq. 1.27 that appears in the theory. The most general soft supersymmetry breaking part of the Lagrangian can be written as follows:

$$\begin{aligned} V_{\text{soft}} &= \epsilon_{ab}\, b\, H_u^a H_d^b + \epsilon_{ab}\left[A_{ij}^u\, \tilde{Q}_i^a H_u^b \tilde{\bar{u}}_j + A_{ij}^d H_d^a \tilde{Q}_i^b \tilde{\bar{d}}_j + A_{ij}^e H_d^a \tilde{L}_i^b \tilde{\bar{e}}_j \right] + \text{h.c.} \\ &+ \tilde{Q}^\dagger \mathbf{\tilde{m}_Q^2}\, \tilde{Q} + \tilde{\bar{u}}^\dagger \mathbf{\tilde{m}_u^2}\, \tilde{\bar{u}} + \tilde{\bar{d}}^\dagger \mathbf{\tilde{m}_d^2}\, \tilde{\bar{d}} + \tilde{L}^\dagger \mathbf{\tilde{m}_L^2} \tilde{L} + \tilde{\bar{e}}^\dagger \mathbf{\tilde{m}_e^2}\, \tilde{\bar{e}} + \tilde{m}_{H_u}^2 |H_u|^2 + \tilde{m}_{H_d}^2 |H_d|^2 \\ &+ \frac{M_1}{2}\tilde{B}\tilde{B} + \frac{M_2}{2}\tilde{W}\tilde{W} + \frac{M_3}{2}\tilde{g}\tilde{g} + \text{h.c.}\,. \end{aligned} \tag{2.5}$$

In Eq. 2.5, b is a complex scalar, which stands for the biliear interactions for the Higgs doublets H_u and H_d. A_{ij}^u, A_{ij}^d and A_{ij}^e are trilinear coupling of the Higgs to the scalar partners of the right-handed and left-handed fermions. i and j are family indices going from 1 to 3. $\mathbf{\tilde{m}_Q^2}, \mathbf{\tilde{m}_u^2}, \mathbf{\tilde{m}_d^2}, \mathbf{\tilde{m}_L^2}$, and $\mathbf{\tilde{m}_e^2}$ are 3×3 hermitian matrices, which contribute to the masses of the scalar partners of fermions with the same handedness. $\tilde{m}_{H_u}^2$ and $\tilde{m}_{H_d}^2$ are squared-mass terms of Higgs fields H_u and H_d, respectively, and are real parameters. M_1, M_2, and M_3 are the bino, wino, and gluino mass terms.

2.1.4 The mass spectrum of the MSSM

Tables 2.1 and 2.2 show the gauge eigenstates of supersymmetric particles (sparticles). These sparticles obtain their masses via soft supersymmetry breaking terms introduced in the previous subsection and after spontaneous breaking of the electroweak symmetry, some of these sparticles mix together due to the Higgs VEVs. Here I will just briefly summarize the mass eigenstates of the particles in the MSSM. For detailed derivations please see Ref [20].

There are two Higgs doublets H_u and H_d, which both acquire non-zero VEV v_u and v_d in the minimum of the scalar potential. The ratio of them is written as

$$\tan\beta \equiv \frac{v_u}{v_d}.$$

The total number of real fields in H_u and H_d is eight. The mixing of these eight real scalar fields in the gauge eigenstates forms five scalar Higgs fields in mass eigenstates h^0, H^0, A^0 and $H^\pm$ and three Goldstone bosons. Similar to the SM, these three Goldstone bosons are eaten by the gauge bosons Z^0 and $W^\pm$. Note that h^0 and H^0 are even while A^0 is odd under CP transformation.

For sfermions, because the Yukawa couplings for the first and second generation fermions are small, it is a good approximation to ignore the mixing between the gauge eigenstates $\widetilde{f}_L$ and $\widetilde{f}_R$. As a consequence, for the first and second generation sfermions, their mass eigenstates are the same as the gauge eigenstates. However, since the third generation fermions have larger Yukawa couplings, the mixing between $\widetilde{f}_L$ and $\widetilde{f}_R$ is no longer negligible. Hence the mass eigenstates of the third generation sfermions $\widetilde{f}_1$ and $\widetilde{f}_2$ are linear combinations of $\widetilde{f}_L$ and $\widetilde{f}_R$. For instance, the mass eigenstates of scalar top are $\widetilde{t}_1$ and $\widetilde{t}_2$. Note that by convention $M_{\widetilde{f}_2}$ and $M_{\widetilde{f}_1}$ always refers to the heavier and the lighter between two mass eigenstates, respectively. In the gauge eigenstate basis, there are two neutral gauginos, $(\widetilde{B}, \widetilde{W})$, and two neutral higgsinos, $(\widetilde{H}_u^0, \widetilde{H}_d^0)$, whose linear combinations form the mass eigenstates called neutralinos $(\widetilde{\chi}_i^0, i = 1 \sim 4)$. By convention we define $M_{\widetilde{\chi}_4} > M_{\widetilde{\chi}_3} > M_{\widetilde{\chi}_2} > M_{\widetilde{\chi}_1}$. Similarly, the charged gauginos $\widetilde{W}^\pm$ and higgsinos $(\widetilde{H}_u^+, \widetilde{H}_d^-)$ form mass eigenstates called charginos $(\widetilde{\chi}_i^\pm, i = 1 \sim 2)$ and $M_{\widetilde{\chi}_2^\pm} > M_{\widetilde{\chi}_1^\pm}$. For the gluino, since it is the only gaugino that is color octet and electrically neutral, the mass eigenstates are the same as the gauge eigenstates.

2.1.5 Supersymmetry breaking scenarios

As discussed in Sec. 2.1.3, a realistic supersymmetry breaking scenario is very helpful to study the weak scale phenomenology. There are large amount of free parameters in the MSSM. Some reasonable assumptions can considerably reduce the number of parameters For instance, ignoring all the CP violations sources or assuming flavor diagonal in the scalar sector of the MSSM. However, the number of free parameters is still intractable. There are several supersymmetry breaking schemes. The three most

widely discussed in the literature are gravity-mediated (mSUGRA), gauge-mediated (GMSB), and anomaly-mediated (AMSB) supersymmetry breaking models. In these scenarios, the large amount of unknown supersymmetry parameters can be reduced to about five parameters. They provide realistic supersymmetric models and make the phenomenological study of the MSSM possible.

In mSUGRA the supersymmetry breaking is mediated by gravitational interaction. There are four free parameters and the sign of μ at the Planck or GUT scale.

$$M_3 = M_2 = M_1 = m_{1/2}, \tag{2.6}$$

$$\mathbf{m_Q^2} = \mathbf{m_{\bar{u}}^2} = \mathbf{m_{\bar{d}}^2} = \mathbf{m_L^2} = \mathbf{m_{\bar{e}}^2} = m_0^2\,\mathbf{1}, \qquad m_{H_u}^2 = m_{H_d}^2 = m_0^2, \tag{2.7}$$

$$\mathbf{a_u} = A_0\mathbf{y_u}, \qquad \mathbf{a_d} = A_0\mathbf{y_d}, \qquad \mathbf{a_e} = A_0\mathbf{y_e}, \tag{2.8}$$

and b, the bilinear term in the soft terms, which is usually re-expressed in terms of tanβ. Also the sign of μ in the superpotential is undetermined, but the magnitude of it can be constrained by the requirement of electroweak symmetry breaking. m_0^2 and $m_{\frac{1}{2}}$ are universal gaugino and scalar masses. A_0 is the trilinear coupling.

The low energy supersymmetric parameters can be obtained by running down the RGE. The typical mSUGRA mass spectrum can be found in Ref [21]. In the typical mSUGRA, SPS1a gives the parameters:

$$m_0 = 100\,\text{GeV}, m_{\frac{1}{2}} = 250\,\text{GeV}, \tag{2.9}$$

$$A_0 = -100\,\text{GeV},\ \tan\beta = 10,\ \mu > 0. \tag{2.10}$$

In this scenario the LSP is always χ_1^0, which is mainly Bino-like and the next-to-the LSP (NLSP) is usually χ_2^0, which is mainly wino-like. The sleptons is usually lighter than the squarks.

2.2 Universal Extra Dimensions

There are many extra dimension models, among which UED models [12] have many interesting phenomenological implications and have been widely discussed in the literature. The mass spectrum of particles in these models are very similar to that in supersymmetry and therefore how to distinguish one model from the other at colliders such as the LHC becomes very important and pressing. In this thesis I will discuss UED with one and two extra dimensions.

2.2.1 Five-dimensional UED

In the UED all fields are allow to propagate in the bulk in contrast to other extra dimensional models. This is also the reason why it is called "universal". The extra dimension is compactified on a circle of radius R. From now on, I will use notation x for the four ordinary space-time dimensions and y for the extra dimension. In

order to have chiral fermions in the low energy limit, an S_1/Z_2 orbifold is introduced. S_1 stands for a one-dimensional torus, *i.e.* a circle. An identification $y \to -y$ is introduced, and $y = 0$ and $y = \pi$ are fixed points. This identification indicates that there exists a Z_2 symmetry or KK-parity P_{KK} on the extra dimension. By introducing this symmetry one can project out the unwanted zero modes that do not exist in the SM. The KK-parity is defined as

$$P_{KK} = (-1)^n, \tag{2.11}$$

where n denotes KK number. I will explain in detail below that all the SM particles have n=0 and are even under KK-parity while particles in the first KK-excitation state are odd under KK-parity. Similar to R-parity in the MSSM, KK-parity can ensure that the new heavy particles are produced in pairs. It also guarantees the existence of a stable lightest KK particle (LKP) which is also a good dark matter candidate. The LKP in most of the UED theories is KK-photon $B^0_{\mu,(1)}$.

Let us start with the simplest case, namely, scalar fields in five-dimensional UED (UED5). The Lagrangian for scalar fields in the five dimensional space-time reads

$$\begin{aligned} \mathcal{L} &= \partial^M \phi \partial_M \phi + m^2 \phi \\ &= \partial^\mu \phi \partial_\mu \phi + \partial^5 \phi \partial_5 \phi + m^2 \phi, \end{aligned} \tag{2.12}$$

where M = 0, 1, 2, 3, and 5 are 5D indices while μ=0, 1, 2, 3 are 4D indices. Since the extra dimension is compactified on a circle, $\phi(x, y)$ is a periodic function of y and can be decomposed into different Fourier modes. It is also called KK-decomposition. The even functions satisfy the Neumann boundary conditions at 0 and π

$$\partial_5 \phi^+(x, y) = 0, \tag{2.13}$$

where

$$\phi^+(x, y) = \frac{1}{\sqrt{2\pi R}} \phi_0^+(x) + \frac{1}{\sqrt{\pi R}} \sum_{n=1}^{\infty} \phi_n^+(x) \cos\frac{ny}{R}. \tag{2.14}$$

n denotes the KK number and the SM mode corresponds to n=0 mode. The odd functions satisfy the Dirichlet boundary conditions at 0 and π

$$\phi^-(x, y) = 0, \tag{2.15}$$

where

$$\phi^-(x, y) = \frac{1}{\sqrt{\pi R}} \sum_{n=1}^{\infty} \phi_n^-(x) \sin\frac{ny}{R}. \tag{2.16}$$

One can then obtain the mass of n-th excitation state

$$m_n^2 = (\frac{n}{R})^2 + m_0^2. \tag{2.17}$$

Thus, the mass spectrum at tree-level of the n-th KK-state is almost degenerate.

For fermions, the orbifold gives rise to the chiral structure of the zero modes particles so that the UED5 agrees with SM in the low energy limit. In the SM, fermions are in an SU(2) doublet if they are left-handed or in an SU(2) singlet if they are right-handed. I start with decomposing an SU(2) singlet states $\psi_R(x,y)$

$$\psi_R^+(x,y) = \frac{1}{\sqrt{2\pi R}}\psi_R^0(x) + \frac{1}{\sqrt{\pi R}}\sum_{n=1}^{\infty}\psi_R^n(x)\cos\frac{ny}{R}, \tag{2.18}$$

$$\psi_R^-(x,y) = \frac{1}{\sqrt{\pi R}}\sum_{n=1}^{\infty}\psi_L^n(x)\sin\frac{ny}{R}, \tag{2.19}$$

where $\psi_R^0(x)$ corresponds to the right-handed SU(2) singlet fermion. One can also see that for $n>0$ the KK-excitation states $\psi_R^n(x)$ and $\psi_L^n(x)$ both exist and together they form a vector-like fermion.

Similarly left-handed SU(2) doublet fermions reads

$$\mathbf{\Psi}_L^+(x,y) = \frac{1}{\sqrt{2\pi R}}\mathbf{\Psi}_L^0(x) + \frac{1}{\sqrt{\pi R}}\sum_{n=1}^{\infty}\mathbf{\Psi}_L^n(x)\cos\frac{ny}{R}, \tag{2.20}$$

$$\mathbf{\Psi}_L^-(x,y) = \frac{1}{\sqrt{\pi R}}\sum_{n=1}^{\infty}\mathbf{\Psi}_R^n(x)\sin\frac{ny}{R}, \tag{2.21}$$

where $\mathbf{\Psi}_L^0(x)$ corresponds to the left-handed SU(2) doublet fermion. Similarly, for $n>0$ the KK-excitation states $\mathbf{\Psi}_L^n(x)$ and $\mathbf{\Psi}_R^n(x)$ both exist and together they form a vector-like fermion.

In this thesis I will use $\mathbf{\Psi}_D^n(x)$ to stand for the n-th KK-excitation state of a left-handed SU(2) doublet fermion and $\psi_S^n(x)$ to represent the n-th KK-excitation state of a right-handed SU(2) singlet fermion.

For gauge field $A_M(x,y)=(A_\mu, A_5)$ the orbifold compactification forces the first four components to be even under P_{KK} and hence satisfies the Neumann boundary condition; A_5 is odd under P_{KK} and therefore satisfies the Dirichlet boundary condition.

$$A_\mu(x,y) = \frac{1}{\sqrt{\pi R}}(\,A_\mu^0(x) + \frac{1}{\sqrt{\pi R}}\sum_{n=1}^{\infty}A_\mu^n(x)\cos\frac{ny}{R}\,), \tag{2.22}$$

$$A_5(x,y) = \frac{2}{\sqrt{\pi R}}\sum_{n=1}^{\infty}A_5^n(x)\sin\frac{ny}{R}. \tag{2.23}$$

A summary of the particle contents in the UED5 is listed in Table 2.3.

2.2.2 Six-dimensional UED

Six-dimensional UED (UED6) is similar to UED5, but now there are two extra dimensions that are compactified. Hence the particles listed in Table 2.3 obtain one

Names	KK modes ($n > 0$)	$SU(3)_C$, $SU(2)_L$, $U(1)_Y$
Quark doublet	$(U_{D,(n)} \;\; D_{D,(n)})$	$(\,\mathbf{3},\,\mathbf{2}\,,\,\frac{1}{6})$
Quark singlet	$u_{S,(n)}$	$(\,\mathbf{3},\,\mathbf{1},\,\frac{2}{3})$
	$d_{S,(n)}$	$(\,\mathbf{3},\,\mathbf{1},\,-\frac{1}{3})$
Lepton doublet	$(\nu_{D,(n)} \;\; \ell_{D,(n)})$	$(\,\mathbf{1},\,\mathbf{2}\,,\,-\frac{1}{2})$
Lepton singlet	$\ell_{S,(n)}$	$(\,\mathbf{1},\,\mathbf{1},\,-1)$
Higgs	$(H_n^+ \;\; H_n^0)$	$(\,\mathbf{1},\,\mathbf{2}\,,\,+\frac{1}{2})$
gluon	$G_{\mu,(n)}$	$(\,\mathbf{8},\,\mathbf{1}\,,\,0)$
weak bosons	$W^{\pm}_{\mu,(n)}\,,\,W^0_{\mu,(n)}$	$(\,\mathbf{1},\,\mathbf{3}\,,\,0)$
B boson	$B^0_{\mu,(n)}$	$(\,\mathbf{1},\,\mathbf{1}\,,\,0)$

Table 2.3: *Particle contents of UED5. The subscript D stands for SU(2) doublet states while S denotes SU(2) singlet states.*

more degree of freedom and carry two indices (m,n). Similar to UED5 the KK-parity in UED6 can be defined as

$$P_{KK} = (-1)^{(n+m)}, \quad \text{for (n, m) KK} - \text{excitation states.} \tag{2.24}$$

Throughout this thesis the (0, 1) mode will be the focus and it will be denoted by (1) for simplicity. UED6 is well-motivated not only because protons have long lifetime in this theory [22] but also it provides an explanation of the number of fermion generations [23]. One of the characteristics of this model is the presence of scalar adjoint particles, the KK modes of gauge bosons polarized along extra dimensions. Therefore, for each vector boson there exists the corresponding scalar partner. In this thesis I will use $G_{H,(n)}, W^{\pm}_{H,(n)}, W^0_{H,(n)}$, and $B^0_{H,(n)}$ to stand for the scalar partners of $G_{\mu,(n)}, W^{\pm}_{\mu,(n)}, W^0_{\mu,(n)}$, and $B^0_{\mu,(n)}$, respectively.

Chapter 3

Neutrino Physics

The existing experimental neutrino data have provided us with compelling evidence that neutrinos are massive and they change flavors while traveling from the source to the detector. Analogous to the CKM matrix in the quark sector, the Pontecorvo-Maki-Nakagawa-Sakata (PMNS) matrix governs the mixing between mass eigenstates and flavor eigenstates in the lepton sector. It can be written as

$$U_{PMNS} = \begin{pmatrix} U_{e1} & U_{e2} & U_{e3} \\ U_{\mu 1} & U_{\mu 2} & U_{\mu 3} \\ U_{\tau 1} & U_{\tau 2} & U_{\tau 3} \end{pmatrix} \tag{3.1}$$

which is a unitary matrix and can be parametrized by three angles θ_{ij} ($ij = 12, 13,$ and 23), and three phases δ, ρ and σ.

$$U_{PMNS} = \begin{pmatrix} c_{12}c_{13} & s_{12}c_{13} & s_{13}e^{-i\delta} \\ -c_{23}s_{12} - c_{12}s_{23}s_{13}e^{i\delta} & c_{12}c_{23} - s_{12}s_{23}s_{13}e^{i\delta} & c_{13}s_{23} \\ s_{23}s_{12} - c_{12}c_{23}s_{13}e^{i\delta} & -c_{12}s_{23} - s_{12}c_{23}s_{13}e^{i\delta} & c_{23}c_{13} \end{pmatrix} \begin{pmatrix} e^{i\rho} & & \\ & e^{i\sigma} & \\ & & 1 \end{pmatrix} \tag{3.2}$$

where $s_{ij} \equiv \sin\theta_{ij}, c_{ij} \equiv \cos\theta_{ij}$. Notice that if neutrinos are Dirac fermions, the Majorana phases ρ and σ can be rotated away by redefining the right-handed neutrino fields.

If θ_{13} is very small then the CP violation effect in the lepton sector would be negligible even if the Dirac phase is non-zero. New results on θ_{13} have been announced by several experiments. The recent result by the Daya Bay collaboration gives $\theta_{13} \simeq 8.8^\circ \pm 0.8^\circ$ or

$$\sin^2 2\theta_{13} = 0.092 \pm 0.016(\text{stat}) \pm 0.005(\text{syst}) \tag{3.3}$$

which is not only non-zero but also "large". As a result, if the CP violation in the lepton sector is not small we would be able to observe this CP violating phase in the future.

For the other two angles the latest global analysis of neutrino oscillation data yields

$$\sin^2\theta_{12} = 0.312^{+0.017}_{-0.015} \tag{3.4}$$

$$\sin^2\theta_{23} = 0.52 \pm 0.06 \tag{3.5}$$

Many papers have proposed various approaches to understand the observed mixing. Some of them utilize models with different discrete flavor symmetries, such as $S_3, S_4, A_4,$ and A_5, dihedral groups etc. [24, 25], to produce several mixing patters including democratic, bi-maximal, tri-bimaximal, hexagonal or golden ratio. Among these mixing patterns tri-bimaximal mixing seems to have better agreement with the current oscillation data. Therefore in this thesis I will focus on the realization of this mixing pattern in the model with S_3 symmetry.

3.1 Consequences of Approximate S_3 Symmetry of the Neutrino Mass Matrix

Early solar neutrino data suggested that one neutrino eigenstate could be

$$S = \frac{1}{\sqrt{3}}\left(\nu_e + \nu_\mu + \nu_\tau\right) \ . \tag{3.6}$$

This led to the consideration of an S_3 symmetry [26]. Today the MSW solution to the solar neutrino problem has the higher-energy neutrinos emerging from the sun in a state given to a good approximation by S. Here I consider the possibility that the neutrino mass matrix is dominated by a term with S_3 symmetry leading to S as an eigenstate. I then consider possible perturbations that violate the symmetry.

My assumption is that neutrino mass is due to new physics not directly related to the origin of the masses of other particles. A large number of papers [25] have presented detailed models based on S_3 symmetry. Here I do not consider a model but simply try to relate possible symmetries of the new physics to observations. The most general Majorana mass matrix invariant under S_3 is

$$M_0 = \begin{pmatrix} A & B & B \\ B & A & B \\ B & B & A \end{pmatrix} \ . \tag{3.7}$$

The eigenstates are necessarily [26] a singlet given by S and a degenerate doublet D which can be chosen as

$$D_a = \frac{\nu_\mu - \nu_\tau}{\sqrt{2}} \ , \tag{3.8a}$$

$$D_b = \sqrt{\frac{2}{3}}\,\nu_e - \sqrt{\frac{1}{6}}\left(\nu_\mu + \nu_\tau\right) \ . \tag{3.8b}$$

The masses are

$$m_{_S} = A + 2B \ , \tag{3.9a}$$

$$m_{_D} = A - B \ . \tag{3.9b}$$

The eigenstates in Eq.(3.6) and Eq.(3.8) are those of the tri-bimaximal form of the mixing matrix discussed in many papers [27] as a fit to neutrino oscillation data. However, in the fit the largest mass splitting is that between $D_{_a}$ and $D_{_b}$ responsible for the atmospheric neutrino oscillation with smaller splitting between S and $D_{_b}$ associated with the solar neutrino oscillation. I assume that the breaking of the degeneracy is due to the perturbation that breaks $S_{_3}$. In order that the $S_{_3}$ term dominate I require that all three masses start out approximately equal by choosing

$$B = -2A + b \ , \tag{3.10a}$$

with $b \ll B$ so that

$$m_{_D} \approx -m_{_S} \approx 3A \ . \tag{3.10b}$$

The minus sign means that the state S has the opposite CP eigenvalue from that of D. I have assumed here for simplicity that A and B are real; otherwise D and S would have a relative Majorana phase. The sub-dominant mass matrix $M_{_1}$ that breaks $S_{_3}$ has the result of raising the mass of one D state above $m_{_S}$ and leaving the mass of the other slightly below $m_{_S}$. These mass values then correspond to what is called the "quasi-degenerate" case for neutrino masses.

I now assume that the perturbing matrix $M_{_1}$, which is added to $M_{_0}$, breaks $S_{_3}$ but retains a $S_{_2}$ symmetry between $\nu_{_\mu}$ and $\nu_{_\tau}$.

$$M_1 \ = \ \begin{pmatrix} e & f & f \\ f & t & \epsilon \\ f & \epsilon & t \end{pmatrix} \tag{3.11}$$

As a result of the symmetry $D_{_a}$ remains an eigenstate and the parameter known as $\theta_{_{13}}$ vanishes. In addition to providing the mass splitting between $D_{_a}$ and $D_{_b}$, $M_{_1}$ causes a small mixing of $D_{_b}$ with S. The parameters e and f can be absorbed into A and B and so they are set to zero in what follows. Matrices of the form $M_{_0} + M_{_1}$, with four parameters are discussed in many papers [28].

I now identify the states which start out as $(D_{_a}, S, D_{_b})$ as $(3, 2, 1)$. The mass $m_{_2}$ is understood to be positive although $m_{_S}$ is negative (assuming A is positive). The mass differences are

$$m_{_3} - m_{_1} = \frac{2}{3} \ (t - 2\epsilon) \, , \tag{3.12a}$$

$$m_{_2} - m_{_1} = -\left(b + t + \epsilon\right) \ . \tag{3.12b}$$

The small value of $m_2 - m_1$ required to fit the data involves the fine-tuning of the value of b. The resulting deviation of the factor $\frac{1}{\sqrt{3}}$ for ν_e in S is given approximately by

$$\Delta = \frac{2}{3\sqrt{3}} \left(\frac{t+\epsilon}{6A} \right) = \frac{k}{\sqrt{3}} \left(\frac{m_3 - m_1}{2m_2} \right) , \tag{3.13}$$

$$k = \frac{t+\epsilon}{t-2\epsilon} ,$$

$$\sin^2 \theta_{12} = (\frac{1}{\sqrt{3}} + \Delta)^2 .$$

Since by our assumption of a quasi-degenerate neutrino mass spectrum the mass ratio in Eq.(3.13) is small so that Δ is predicted to be small. To obtain the doublet mass splitting without large parameters I choose $\frac{\epsilon}{t}$ to be negative. As $\frac{\epsilon}{t}$ varies from 0 to a large negative value k varies from 1 to $-\frac{1}{2}$; for $\frac{\epsilon}{t} = -1$, $\Delta = 0$ and I obtain the tri-bimaximal form. Choosing values for the mass-splittings fitted from oscillation data [29]

$$\begin{aligned} m_3^2 - m_2^2 &= 2.6 \times 10^{-3} eV^2 , \\ m_2^2 - m_1^2 &= 8 \times 10^{-5} eV^2 , \end{aligned} \tag{3.14}$$

	m_1 (eV)	m_2 (eV)	m_3 (eV)
1	0.1845	0.1847	0.1913
2	0.1247	0.1250	0.1350
3	0.0512	0.0520	0.0729

Table 3.1: *Three sets of mass values.*

I give in table 3.1 three sets of mass values. The largest values (like set 1) are limited by cosmology [30] whereas the smallest values(like set 3) are limited by the requirement that the magnitude of M_1 is smaller than M_0. For each of these I show in Fig. 3.1 the solar neutrino survival $\sin^2 \theta_{12}$ for the higher energy neutrinos for the LMA-MSW solution as a function of $\frac{\epsilon}{t}$. Note that the sign of the deviation from $\frac{1}{3}$ can be either positive or negative. I have shown the case of the"normal hierarchy" with $(m_3 - m_1)$ positive. In the case of the inverse hierarchy the curves are flipped about the $\sin^2 \theta_{12} = \frac{1}{3}$ axis. Assuming negligible Majorana phases the mass that enters the double beta-decay formula is

$$m_{ee} = -\sin^2 \theta_{12}\, m_2 + \cos^2 \theta_{12}\, m_1 \approx (1 - 2\sin^2\, \theta_{12})\, m_2 , \tag{3.15}$$

given the small difference between m_2 and m_1.

I finally consider a possible small violation of $\mu - \tau$ symmetry by changing the 22 element in Eq.(3.11) to $t + \frac{\delta}{2}$ and the 33 element to $t - \frac{\delta}{2}$. The main effect is to mix D_a and D_b or the states now labeled 3 and 1. There is also a small mixing of 2 and 1 but this is suppressed by the "mass difference" 6A. The important result is a non-zero value of θ_{13}, the ν_e amplitude in state 3. Directly correlated with θ_{13} there is a deviation of θ_{23}, the ν_μ amplitude in state 3, from $\frac{\pi}{4}$.

Starting with the tri-bimaximal mixing, corresponding to the limit $\frac{\epsilon}{t} = -1$, this correlation is given by

$$\tan^2\theta_{23} = 1 - 2\sqrt{2}X + 4X^2 \ \ , X = \sin\theta_{13}\left(\frac{1+2\lambda}{1-\lambda}\right) \ \ , \lambda = \frac{m_3 - m_1}{m_2 + m_1} \ , \qquad (3.16)$$

to order X^2. In Fig. 3.2, I show $(\tan^2\theta_{23} - 1)$ as a function of $\sin\theta_{13}$. Different values of $\frac{\epsilon}{t}$ makes only small changes since they are proportional to $\lambda\Delta$.

3.2 Conclusions

In this chapter I have looked at possible experimental signatures of the assumption that the physics yielding the neutrino mass matrix has a predominant S_3 symmetry. I further assume a sub-dominant term which breaks S_3 but has an S_2 $\mu - \tau$ symmetry. This leads to

(1) The neutrino masses must be quasi-degenerate. Therefore this theory would be ruled out if cosmological analysis convincingly gave a very low limit on the sum of the masses. Considering case 3 in Table 1 as barely quasi-degenerate the sum of the masses should not be less than 0.17 eV.

(2) θ_{13}, the ν_e component in the atmospheric mixing, vanishes and the mixing is maximal.

(3) The high-energy solar neutrino survival, governed by the LMA-MSW solution, deviates only a little from $\frac{1}{3}$ as illustrated in Fig. 3.1.

(4) In the absence of significant Majorana phases the mass m_{ee} governing double beta decay is approximately equal to $\frac{m_2}{3}$. Thus the theory would be ruled out if the value of m_{ee} was found to be too large. For example, if the cosmological limit on the sum of the masses was 0.4 eV consistent with case 2 in Table 1 the value of m_{ee} must be less than 0.05 eV.

If I further allow a small term involving only ν_μ and ν_τ that violates the S_2 symmetry then there is a non-zero θ_{13}. In this case the atmospheric mixing angle is no longer maximum and its value is directly correlated with θ_{13} as shown in Eq.(3.16) and Fig. 3.2. However, the latest values of θ_{23} and θ_{13} would disfavor this approach since in Fig. 3.2 the current value of $\sin\theta_{13} \sim 0.153$, which corresponds to a deviation of $\tan^2\theta_{23}$ from 1 by 0.25, and thus is disfavored by current experiments.

An alternative to generating nonzero θ_{13}, is to assume that the leptonic mixing matrix U_{PMNS} is the product of the Hermitian conjugate of the charged lepton mixing matrix $U_\ell^\dagger$ and the neutrino mixing matrix U_ν [31]. Since charged leptons, like

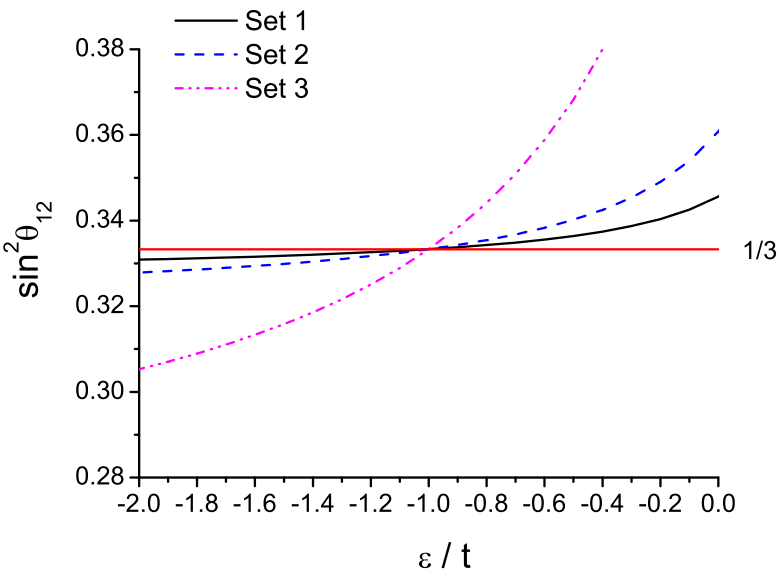

Figure 3.1: *The solar neutrino survival* $\sin^2\theta_{12}$ *for the higher energy neutrinos for the LMA-MSW solution as a function of* $\frac{\epsilon}{t}$.

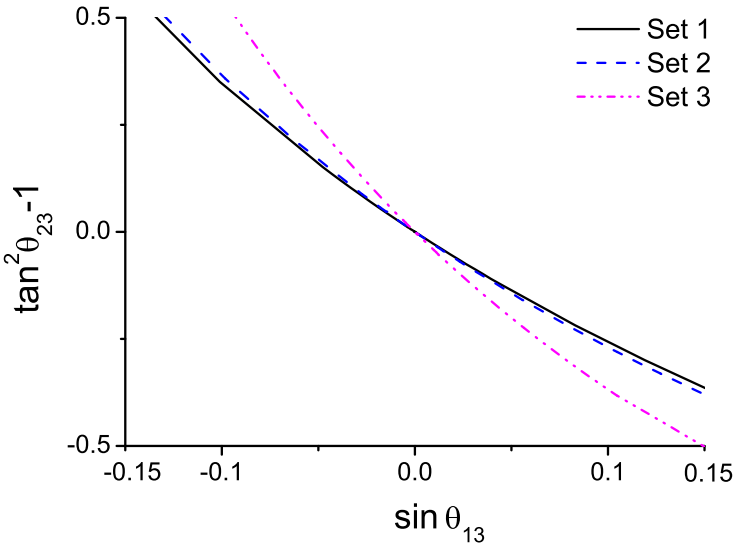

Figure 3.2: *Diagram with* $\tan^2\theta_{23} - 1$. *v.s* $\sin\theta_{13}$.

quarks, are Dirac fermions while in many new physics scenarios neutrinos are Majorana fermions, it is tempting to assume that U_ℓ is a CKM-like matrix, which has a hierarchical structure and is parameterized by a small quantity λ, whereas U_ν is of tribimaximal form. This leads to $\sin\theta_{13} \sim -\frac{\lambda}{\sqrt{2}} = -0.156$ and $\tan\theta_{23} \sim -1.057$ for $\lambda \sim 0.22$, which agree very well with the current experimental data.

Chapter 4

General analysis of signals with two leptons and missing energy at the LHC

4.1 Introduction

Many BSM models include stable weekly interacting massive particles which could be constituents of dark matter. Since the stability of these particles is generally related to some symmetry, they can be produced only in pairs at colliders, leading to challenging signatures with at least two invisible objects in the detector. At hadron accelerators like the LHC such a signal is not sufficiently kinematically constrained to use direct reconstruction techniques, and thus it is very difficult to uniquely determine the properties of the produced particles.

One of the most challenging cases are processes with a low-multiplicity final state of only two visible objects, which is the focus of this chapter. In particular I will consider the production of a pair of oppositely charged heavy new particles $Y^{\pm}$ at the LHC, which each decay into a SM lepton and an invisible neutral massive particle X^0:

$$pp \to Y^+Y^- \to \ell^+\ell^- X^0 \bar{X}^0, \qquad (\ell = e, \mu). \tag{4.1}$$

Several methods for determining the Y and X masses in processes of this type have been proposed in the literature [11, 32–34]. Furthermore, a number of authors have studied how to extract spin information from angular distributions [35–37] and the total production rate [38]. The latter method, while potentially being very powerful, requires knowledge of the branching fractions of $Y^{\pm}$, which are *a priori* unknown without model assumptions. To the best of my knowledge, however, the problem of determining the couplings of the new particles, which are related to their gauge group representations, has not yet been considered.

The goal of this chapter is to analyze the process (4.1) in a more model-independent approach by considering all possible assignments for spins (up to spin one) and SU(2)

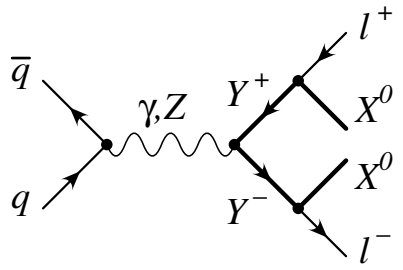

Figure 4.1: *Basic diagram topology for the new physics processes under consideration. Thick lines indicate new particles, while thin lines denote SM particles.*

representations (up to triplets) for the particles X and Y. To discriminate between these template model combinations, I discuss several variables for the measurement of masses, spins, and interactions of the new particles, including two new spin-sensitive observables and one new observable for the coupling determination. To minimize model dependence, the total cross section is not considered in this set of variables.

Besides using dedicated observables, I also study an alternative analysis strategy based on an automated likelihood test. This method matches the observed lepton momenta in a sample of events to the corresponding momenta of a theoretically calculated matrix element in a given model and calculates a likelihood from that [14,39]. Note that the two approaches based on specific observables and on the automated likelihood test are complementary. The latter often reaches a higher statistical significance due to the fact that no information is lost by projecting onto a some variable, but it does not permit a straightforward separation between individual particle properties, such as spin and couplings.

After characterizing all relevant spin and coupling representations in section 4.2 and identifying 11 independent model combinations, I present observables for the measurement of particle properties in section 4.3 and demonstrate their usefulness in a Monte-Carlo study. Section 4.4 is devoted to the analysis of the same set of template models with the likelihood test method. Finally, the conclusions are given in section 4.5.

4.2 Setup

The class of processes under consideration each involve Drell-Yan–type production of a pair of charged heavy particles $Y^{\pm}$, which each subsequently decay into a lepton $\ell^{\pm}$ ($\ell = e, \mu$) and a neutral heavy particle X^0, see Fig. 4.1. It is assumed that the $Y^{\pm}$ and X^0 are charged under some discrete symmetry, such that they can be produced only in pairs and the lighter new particle (X^0) is stable and escapes from the detector without leaving a signal. The observable signature thus consists of two same-flavor opposite-sign leptons and missing momentum: $\ell^+\ell^- + \not{E}$. For this process it is insubstantial whether X^0 is self-conjugate or not. For the purpose of this work it

is assumed that no other new heavy particles play a role in the s- or t-channel of the Y^+Y^- production process [note, however, that if Y is a vector boson this assumption is not valid, as will be explained below]. In fact, LHC data itself will be able to set a strong lower bound on such particles: searches for di-jet resonances could rule out s-channel resonances that couple to light quarks up to several TeV, and any new particles in the t-channel need to be colored and thus could be produced directly with large cross sections unless their masses are larger than 2–3 TeV [2][1]. Therefore, if the LHC does not see any such signals, one can safely neglect the presence of extra particles in the s- and t-channel of Y^+Y^- production.

Table 4.1 lists 16 possible combinations of spins up to spin one and singlet, doublet, or (adjoint) triplet representations under the weak SU(2) for the fields X and Y. I do not consider complex SU(2) triplets, since they contain doubly charged particles, which would lead to a clearly distinguishable signature.

Also shown are the structure of the couplings between the Y and the Z boson and between X, Y, and SM charged leptons. The γYY couplings has the same form as the ZYY coupling. The coupling constants for the ZYY coupling are shown in Table. 4.2, given in terms of the ratio with respect to the γYY coupling, $R_{\mathrm{ZA}} \equiv g(ZYY)/e$. The strength of the $XY\ell$ coupling depends on the detail of the given model, and it is only relevant for the overall decay branchings, but not for the shapes of distributions. I neglect corrections from electroweak symmetry breaking to the masses and interactions of X and Y. As a result, if Y is a spin-1/2 fermion it couples to the Z boson only through non-chiral vector couplings.

For illustration, Tab. 4.1 also gives examples for concrete realizations of all 16 spin and gauge group assignments within the Minimal Supersymmetric Standard Model (MSSM) or models with universal extra dimensions. However, many of these combinations can also be realized in other models.

A comment is on order regarding the combination 11 in the table. Taking only the s-channel diagrams in Fig. 4.1, the cross section for spin-1 Y pair production grows unboundedly for increasing partonic center-of-mass energy. This is a result of incomplete SU(2) gauge cancellations. Gauge invariance requires the presence of an additional new particle in the t-channel, which interferes negatively with the s-channel contribution and thus preserves perturbative unitarity. In the case of universal extra dimensions this rôle is played by the KK-quarks. Therefore, for model 11 we include a new colored fermion $\hat{Q}$ that is charged under the same discrete symmetry as X and Y. The coupling strength of the $q\hat{Q}Y$ interaction is prescribed by gauge invariance: $g(\bar{q}\hat{Q}Y) = g$. While for consistency it is necessary to incorporate this particle in the cross-section calculation, it is still possible that it is too massive to be seen directly at the LHC, *i. e.* $m_{\hat{Q}} > \mathcal{O}(\mathrm{TeV})$.

The cross sections for the Drell-Yan–type process in Fig. 4.1 for the different models in Tab. 4.1 range from a few fb to several hundred fb for a center-of-mass energy of $\sqrt{s} = 14$ TeV and X/Y masses of a few hundred GeV, see appendix A. As

[1] These estimated bounds pertain to the LHC with a center-of-mass energy of 14 TeV.

	Y s, $I_{\mathrm{SU}(2)}$	X s, $I_{\mathrm{SU}(2)}$	ℓ $I_{\mathrm{SU}(2)}$	ZYY coupling	$XY\ell$ coupling	sample model and decay $Y^- \to \ell^- X$
1	0, **1**	$\frac{1}{2}$, **1**	**1**	$Z^\mu Y^* \overleftrightarrow{\partial_\mu} Y$	$\overline{X}\frac{1+\gamma_5}{2}\ell\, Y^*$	MSSM $\tilde{\ell}^-_{\mathrm{R}} \to \ell^- \tilde{B}^0$
1a	0, **1**	$\frac{1}{2}$, **2**	**2**	$Z^\mu Y^* \overleftrightarrow{\partial_\mu} Y$	$\overline{X}\frac{1-\gamma_5}{2}\ell\, Y^*$	MSSM $\tilde{\ell}^-_{\mathrm{R}} \to \ell^- \tilde{H}^0$
2	0, **2**	$\frac{1}{2}$, **1**	**2**	$Z^\mu Y^* \overleftrightarrow{\partial_\mu} Y$	$\overline{X}\frac{1-\gamma_5}{2}\ell\, Y^*$	MSSM $\tilde{\ell}^-_{\mathrm{L}} \to \ell^- \tilde{B}^0$
2a	0, **2**	$\frac{1}{2}$, **2**	**1**	$Z^\mu Y^* \overleftrightarrow{\partial_\mu} Y$	$\overline{X}\frac{1+\gamma_5}{2}\ell\, Y^*$	MSSM $\tilde{\ell}^-_{\mathrm{L}} \to \ell^- \tilde{H}^0$
2b	0, **2**	$\frac{1}{2}$, **3**	**2**	$Z^\mu Y^* \overleftrightarrow{\partial_\mu} Y$	$\overline{X}\frac{1-\gamma_5}{2}\ell\, Y^*$	MSSM $\tilde{\ell}^-_{\mathrm{L}} \to \ell^- \tilde{W}^0$
3	0, **3**	$\frac{1}{2}$, **2**	**2**	$Z^\mu Y^* \overleftrightarrow{\partial_\mu} Y$	$\overline{X}\frac{1-\gamma_5}{2}\ell\, Y^*$	UED6 $W^-_{H,(1)} \to \ell^- \nu_{(1)}$
4	$\frac{1}{2}$, **1**	0, **1**	**1**	$\overline{Y} \not{Z} Y$	$\overline{Y}\frac{1+\gamma_5}{2}\ell\, X$	UED6 $\ell^-_{S,(1)} \to \ell^- B^0_{H,(1)}$
5	$\frac{1}{2}$, **1**	0, **2**	**2**	$\overline{Y} \not{Z} Y$	$\overline{Y}\frac{1-\gamma_5}{2}\ell\, X$	UED $\ell^-_{S,(1)} \to \ell^- H^0_{(1)}$
6	$\frac{1}{2}$, **1**	1, **1**	**1**	$\overline{Y} \not{Z} Y$	$\overline{Y} \not{X} \frac{1+\gamma_5}{2}\ell$	UED $\ell^-_{S,(1)} \to \ell^- B^0_{\mu,(1)}$
7	$\frac{1}{2}$, **2**	0, **1**	**2**	$\overline{Y} \not{Z} Y$	$\overline{Y}\frac{1-\gamma_5}{2}\ell\, X$	UED6 $\ell^-_{D,(1)} \to \ell^- B^0_{H,(1)}$
7a	$\frac{1}{2}$, **2**	0, **3**	**2**	$\overline{Y} \not{Z} Y$	$\overline{Y}\frac{1-\gamma_5}{2}\ell\, X$	UED6 $\ell^-_{D,(1)} \to \ell^- W^0_{H,(1)}$
8	$\frac{1}{2}$, **2**	0, **2**	**1**	$\overline{Y} \not{Z} Y$	$\overline{Y}\frac{1+\gamma_5}{2}\ell\, X$	MSSM $\tilde{H}^- \to \ell^- \tilde{\nu}$
9	$\frac{1}{2}$, **2**	1, **1**	**2**	$\overline{Y} \not{Z} Y$	$\overline{Y} \not{X} \frac{1-\gamma_5}{2}\ell$	UED $\ell^-_{D,(1)} \to \ell^- B^0_{\mu,(1)}$
9a	$\frac{1}{2}$, **2**	1, **3**	**2**	$\overline{Y} \not{Z} Y$	$\overline{Y} \not{X} \frac{1-\gamma_5}{2}\ell$	UED $\ell^-_{D,(1)} \to \ell^- W^0_{\mu,(1)}$
10	$\frac{1}{2}$, **3**	0, **2**	**2**	$\overline{Y} \not{Z} Y$	$\overline{Y}\frac{1-\gamma_5}{2}\ell\, X$	MSSM $\tilde{W}^- \to \ell^- \tilde{\nu}$
11	1, **3**	$\frac{1}{2}$, **2**	**2**	$S[Z, Y, Y^*]$	$\overline{X} \not{Y}^* \frac{1-\gamma_5}{2}\ell$	UED $W^-_{\mu,(1)} \to \ell^- \nu_{(1)}$

$$A \overleftrightarrow{\partial_\mu} B \equiv A(\partial_\mu B) - (\partial_\mu A) B,$$
$$S[Z, Y, Y^*] \equiv Z_\mu\, Y^*_\nu \overleftrightarrow{\partial^\mu} Y^\nu + Y_\mu\, Z_\nu \overleftrightarrow{\partial^\mu} Y^{*\nu} + Y^*_\mu\, Y_\nu \overleftrightarrow{\partial^\mu} Z^\nu$$

Table 4.1: *List of different assignments of spin s and SU(2) representations for the charged field Y and the neutral field X. I define Y^-/Y^+ to be the particle/anti-particle. Also shown are the structure of the couplings to the Z boson and to SM leptons, as well as examples for realizations of these assignments in known models. MSSM refers to the Minimal Supersymmetric Standard Model, UED to (at least) one universal extra dimension, and UED6 to (at least) two universal extra dimensions. $\tilde{\ell}^-_{\mathrm{R}}$, $\tilde{\ell}^-_{\mathrm{L}}$, $\tilde{\nu}$, $\tilde{B}^0$, $\tilde{W}^{0,\pm}$, and $\tilde{H}$ denote the superpartners of the right-handed charged lepton, left-handed charged lepton, neutrino, U(1) gauge field, SU(2) gauge fields, and Higgs boson, respectively. $\ell^-_{S,(1)}$, $\ell^-_{D,(1)}$, $\nu_{(1)}$, $B^0_{\mu,(1)}$, $W^{0,\pm}_{\mu,(1)}$, and $H_{(1)}$, respectively, are the first-level KK-excitations of these fields. $B^0_{H,(1)}$ and $W^0_{H,(1)}$ are scalars stemming from one of the extra components of the higher-dimensional gauge fields in UED. More details of these models can be found in Refs. [12, 20].*

$I_{\mathrm{SU(2)}}$	R_{ZA}
1	$-\tan\theta_W \approx -0.548$
2	$\cot(2\theta_W) \approx 0.638$
3	$\cot\theta_W \approx 1.824$

Table 4.2: *Ratio R_{ZA} of the ZYY to γYY coupling strength for different SU(2) representations of Y.*

a result, one can expect between 1000 and several 10,000 events being produced with a total luminosity of 100 fb^{-1}. Note that, as mentioned in the introduction, the total event rate will not be considered to discriminate between models in this chapter.

At the LHC it is not possible to determine the polarizations of the final-state leptons and X particles. As a result, several pairs of combinations in Tab. 4.1 are indistinguishable from each other, since after summing over the spins of the external legs their squared matrix elements are identical. Those sets of look-alikes are (1, 1a), (2, 2a, 2b), (7, 7a), and (9, 9a). This leaves a total of 11 potentially distinguishable combinations, which will be explored in more detail in the following.

These 11 combinations have been implemented into CompHEP 4.5.1 [40] and representative samples with a few thousand parton-level events have been generated for each of them. Since I will not consider the total cross sections as a discriminative quantity, the exact values for the $XY\ell$ coupling and the widths of the Y particles are irrelevant. However, the Y widths have been chosen small enough so that diagrams with off-shell Y particles can be safely neglected, *i. e.* $\Gamma_Y/M_Y \ll 1\%$.

As a first step, initial-state radiation and detector acceptance effects have been ignored in the following analysis, but I discuss these contributions in section 4.3.5.

4.3 Observables for Determination of Particle Properties

The experimental information in the signature $\ell^+\ell^- + \not{E}$ consists of the 3-momenta of the leptons ℓ^+ and ℓ^-, which can be parametrized in terms of their transverse momentum p_{T}, pseudorapidity η and azimuthal angle ϕ. Since the system is invariant under overall azimuthal rotations, one can construct five independent non-trivial

observables from this data. In this work we will focus on the following five quantities:

$$M_{\mathrm{T2}} = \min_{\mathbf{p}_{\mathrm{T},\mathrm{X}_1}+\mathbf{p}_{\mathrm{T},\mathrm{X}_2}=\not{\mathbf{p}}_{\mathrm{T}}} \left\{ \max\left(m_{\mathrm{T}}^{\ell^+,X_1}, m_{\mathrm{T}}^{\ell^-,X_2} \right) \right\}, \tag{4.2}$$

$$\cos\theta^*_{\ell\ell} = \tanh\frac{|\eta_{\ell^+} - \eta_{\ell^-}|}{2} = \tanh\frac{\Delta\eta_{\ell\ell}}{2}, \tag{4.3}$$

$$M_{\mathrm{eff}} = p_{\mathrm{T},\ell^+} + p_{\mathrm{T},\ell^-} + \not{p}_{\mathrm{T}}, \tag{4.4}$$

$$\Delta\phi_{\ell\ell} = \phi_{\ell^+} - \phi_{\ell^-}, \tag{4.5}$$

$$A_{\ell^+\ell^-} = \frac{N(E_{\ell^-} > E_{\ell^+}) - N(E_{\ell^+} > E_{\ell^-})}{N(E_{\ell^-} > E_{\ell^+}) + N(E_{\ell^+} > E_{\ell^-})}. \tag{4.6}$$

Here

$$\left(m_{\mathrm{T}}^{\ell^\pm,X_i}\right)^2 \equiv m_X^2 + 2\left(p_{\mathrm{T},\ell^\pm}\sqrt{m_X^2 + p_{\mathrm{T,X_i}}^2} - \mathbf{p}_{\mathrm{T},\ell^\pm}\cdot\mathbf{p}_{\mathrm{T,X_i}}\right)$$

is the transverse mass of the lepton $\ell^\pm$, assumed to be massless, and one neutral heavy particle X_i, $i = 1, 2$. Furthermore, $\theta^*_{\ell\ell}$ is the polar angle between one lepton and the beam axis in a frame in which the pseudorapidities of the two leptons obey $\eta^*_{\ell^+} = -\eta^*_{\ell^-}$, and $N(E_{\ell^-} > E_{\ell^+})$ denotes the number of events for which ℓ^- has a larger energy than ℓ^+.

This choice of observables is guided by their rôle in determining different particle properties. The first observable in eq. (4.2) is useful for mass measurement, eqs. (4.3)–(4.4) are sensitive to the spins of the new particles, and eq. (4.6) provides information about their couplings.

4.3.1 Mass determination

The variable M_{T2} has been proposed for the measurement of particle masses in events with two or more invisible objects in the final state [11]. M_{T2} and similar variables have been studied extensively in the literature [32], and it was shown that in favorable circumstances one can use these variables to determine both the parent mass m_Y as well as the mass of the invisible child m_X, in particular by including information about initial-state radiation [33]. In this chapter, therefore, mass determination will not be discussed any further, and the reader is referred to Refs. [11, 32, 33] for more details.

4.3.2 Spin determination

A useful observable for determining the spin s_Y of the Y particles in the process in eq. (4.1) is $\cos\theta^*_{\ell\ell} = \tanh(\Delta\eta_{\ell\ell}/2)$, see eq. (4.3), which was introduced by Barr in Ref. [37]. It is based on the observation that the final state leptons $\ell^\pm$ tend to go in the same direction as their parent particles $Y^\pm$, since on average the $Y^\pm$ are produced

with a sizable boost if $m_Y \ll \sqrt{s}$. As a result, the distribution of the lepton polar angle $\theta^*_{\ell\ell}$, in the frame where the pseudorapidities of the two leptons are equal in magnitude, is strongly correlated to the production angle θ^* between one of the Y and the beam axis in the center-of-mass frame.

The θ^* distribution is closely connected to s_Y. For the spin-0 and spin-1/2 cases one finds a characteristic difference which is immediately visible in the formulas

$$\text{scalar } Y \text{ (spin 0):} \qquad \frac{d\sigma}{d\cos\theta^*} \propto 1 - \cos^2\theta^*, \tag{4.7}$$

$$\text{fermion } Y \text{ (spin } \tfrac{1}{2}\text{):} \qquad \frac{d\sigma}{d\cos\theta^*} \propto 2 + \beta_Y^2(\cos^2\theta^* - 1), \tag{4.8}$$

where β_Y is the velocity of the produced Y particles. For spin-1 pair production the situation is more complex since here one necessarily needs to take into account a new particle $\hat{Q}$ in the t-channel. Depending on its mass $m_{\hat{Q}}$, the observable $\theta^*_{\ell\ell}$ distribution can be similar to the spin-0 case or to the spin-1/2 case, or different from both, as can be seen from the numerical results shown in section 5.3.2. Therefore, in general, the observable (4.3) alone does not unambiguously distinguish spin-1 from spin-0 or spin-1/2.

One advantage of the definition (4.3) is that it is invariant under longitudinal boost, *i. e.* the value of $\tanh(\Delta\eta_{\ell\ell}/2)$ does not depend on the momentum fractions carried by the quark and anti-quark in the collision.

Here we propose two other observables for the determination of the Y spin: the effective mass M_{eff} and the difference between the azimuthal angles of the leptons, $\Delta\phi_{\ell\ell}$, see eqs. (4.4) and (4.5). The connection between these variables and s_Y can be understood from the threshold behavior of the partonic cross section $q\bar{q} \to Y^+Y^-$. If Y^+ and Y^- are scalars they are produced in a p-wave and the cross section behaves like $\sigma \sim \beta_Y^3$ near threshold. For fermionic Y, instead, the cross section grows faster near threshold, $\sigma \sim \beta_Y$. Therefore the cross section for fermionic Y pair production reaches its maximum at lower values of the Y^+Y^- invariant mass, m_{YY}, than the cross section for scalar Y pair production. The effective mass M_{eff} is strongly correlated to the Y-pair invariant mass, and thus the M_{eff} distribution will peak at larger values for fermionic Y than for scalar Y (assuming that m_Y is equal in both cases and known from measuring the M_{T2} distribution).

The dependence of the cross section on m_{YY} also leaves a characteristic imprint on the $\Delta\phi_{\ell\ell}$ distribution. Scalar Y pairs will on average be produced with a larger boost than fermionic Y pairs. This leads to a more pronounced peak at $\Delta\phi_{\ell\ell} \sim \pi$ in the scalar case, since the larger boost is more likely to produce a back-to-back configuration for the final-state leptons, see Fig. 4.2

If $Y^\pm$ are vector particles, the M_{eff} and $\Delta\phi_{\ell\ell}$ distributions depend on the mass $m_{\hat{Q}}$ of the particle in the t-channel. For $m_{\hat{Q}} \gg m_Y$, the Y^+Y^- pair production cross section reaches its maximum at larger values of m_{YY} than both the spin-0 and spin-1/2 cases, since the s-channel contribution alone grows monotonically with the

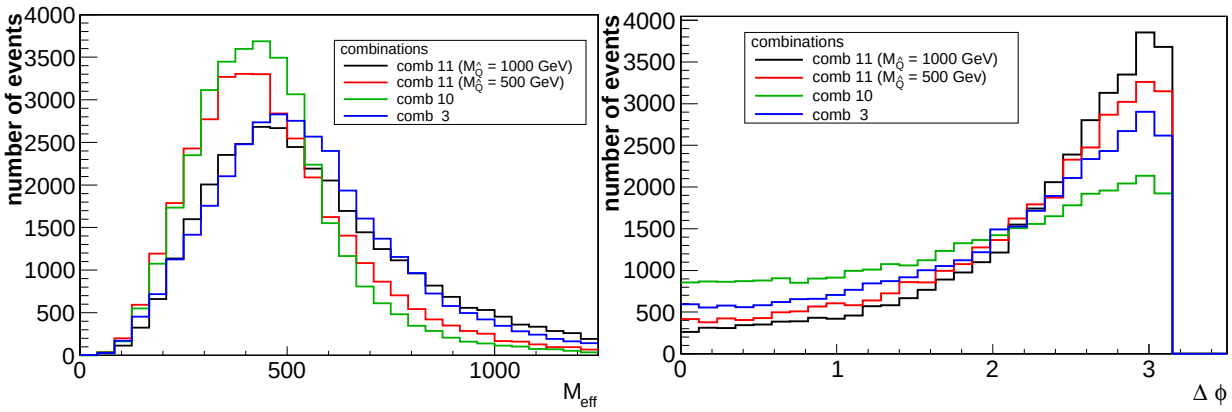

Figure 4.2: *Distributions for M_{eff} (left) and $\Delta\phi_{\ell\ell}$ (right), for combinations 3, 10, and 11 in Tab. 4.1, which correspond to Y particles with spin 0, $\frac{1}{2}$, and 1, respectively. The plot is based on 35000 parton-level events for each combinations without cuts and detector effects, and using the mass values $m_Y = 300$ GeV and $m_X = 100$ GeV. For combination 11, two choices of the mass of the t-channel particles are shown, $m_{\hat{Q}} = 1000$ GeV and 500 GeV.*

center-of-mass energy. In this case, the M_{eff} distribution for vector Y particles will peak at larger values than the other two cases, and the $\Delta\phi_{\ell\ell}$ distribution will be very strongly peaked at π. On the other hand, Fig. 4.2 shows that for $m_{\hat{Q}}$ of the same order as m_Y the M_{eff} distribution can be similar to either the spin-0 or spin-1/2 cases, depending on the precise value of $m_{\hat{Q}}$. Nevertheless, even for a relatively low value $m_{\hat{Q}} = 500$ GeV[2] the $\Delta\phi_{\ell\ell}$ distribution is still distinctly different for spin-1 compared to the other spin cases. By using all three observables (4.3)–(4.5) in combination one therefore obtains the best discrimination power and can unambiguously distinguish between $s_Y = 0$, $\frac{1}{2}$, and 1.

Similar to $\tanh(\Delta\eta_{\ell\ell}/2)$, also $\Delta\phi_{\ell\ell}$ and M_{eff} are invariant under longitudinal boosts, and thus very well suited for hadron colliders.

It needs to be pointed out that the three variables, $\tanh(\Delta\eta_{\ell\ell}/2)$, $\Delta\phi_{\ell\ell}$ and M_{eff}, are primarily sensitive to the spin of the parent particle Y, but not of the child particle X. Indeed, as can be seen from the numerical results in sections 5.3.2 and 4.4, it is very difficult to independently determine the X spin.

4.3.3 Coupling determination

Experiments at LEP and SLC have determined the couplings of the Z boson to SM fermions with very high precision, in particular by measuring various left-right and forward-backward asymmetries [41].

[2]For such low values of $m_{\hat{Q}}$ one should see a signal from direct production of the $\hat{Q}$ particle at the LHC.

Similarly, for the class of processes corresponding to Fig. 4.1, one can in principle try to extract information about the ZYY coupling by constructing a forward-backward asymmetry for $pp \to Y^+Y^-$ at the LHC. Although the initial pp state is symmetric, the incoming quark for a $q\bar{q}$-initiated process will often stem from one of the valence quarks of the protons and thus tends to have a larger momentum than the incoming anti-quark. Therefore one can define the forward direction by the direction of the overall longitudinal boost of an event. However, since I neglect effects from electroweak symmetry breaking in the new physics sector, all combinations in Tab. 4.1 have parity-even ZYY couplings and the forward-backward asymmetry for $pp \to Y^+Y^-$ is exactly zero.

However, the coupling between the incident $q\bar{q}$ pair and Z boson has a parity-odd axial-vector part, which results in the Y^+Y^- pair being produced with a non-vanishing *polarization* asymmetry (unless $Y^\pm$ are scalars). This polarization asymmetry can be probed through the decay $Y^\pm \to \ell^\pm X^0$, since the interaction responsible for the decay is either left- or right-handed and thus sensitive to the Y polarization, see Tab. 4.1.

In the center-of-mass frame of the Y^+Y^- system this leads to a forward-backward asymmetry for the final-state leptons. As mentioned above, in the lab frame the forward direction is defined by the overall boost of an event, which is closely correlated to the direction of the more energetic of the two leptons. Therefore I define the following observable given in eq. (4.6),

$$A_{\ell^+\ell^-} = \frac{N(E_{\ell^-} > E_{\ell^+}) - N(E_{\ell^+} > E_{\ell^-})}{N(E_{\ell^-} > E_{\ell^+}) + N(E_{\ell^+} > E_{\ell^-})}. \tag{4.6}$$

The asymmetry is partially washed out by the mass m_Y, which can cause a spin flip before the Y decays, but I expect a non-vanishing result as long as $m_Y \ll \sqrt{s}$.

Eq. 4.6 is mostly useful for discriminating between combinations with $s_Y = \frac{1}{2}$, since scalars do not carry any polarization and lead to a vanishing asymmetry, and there is only one combination with vector Y particles in Tab. 4.1. The value of $A_{\ell^+\ell^-}$ is connected to the size of the ratio $R_{\mathrm{ZA}} = g(ZYY)/e$ between the ZYY and γYY couplings and to the sign of the γ_5 term in the $XY\ell$ coupling. This is illustrated in Fig. 4.3 for the case that Y is a fermion and X is a vector boson. As evident from the plot, there is a strong correlation between R_{ZA} and $A_{\ell^+\ell^-}$, but one can encounter a two- to three-fold ambiguity when trying to determine R_{ZA} from the measured value of $A_{\ell^+\ell^-}$.

4.3.4 Numerical results

Using CompHEP I have generated parton-level events for all 11 combinations in Tab. 4.1 for a center-of-mass energy of $\sqrt{s} = 14$ TeV and $m_Y = 300$ GeV and $m_X = 100$ GeV. For the following discussion I will assume that the Y and X masses are known from observables like M_{T2} and for simplicity the uncertainty in the mass determination will be neglected.

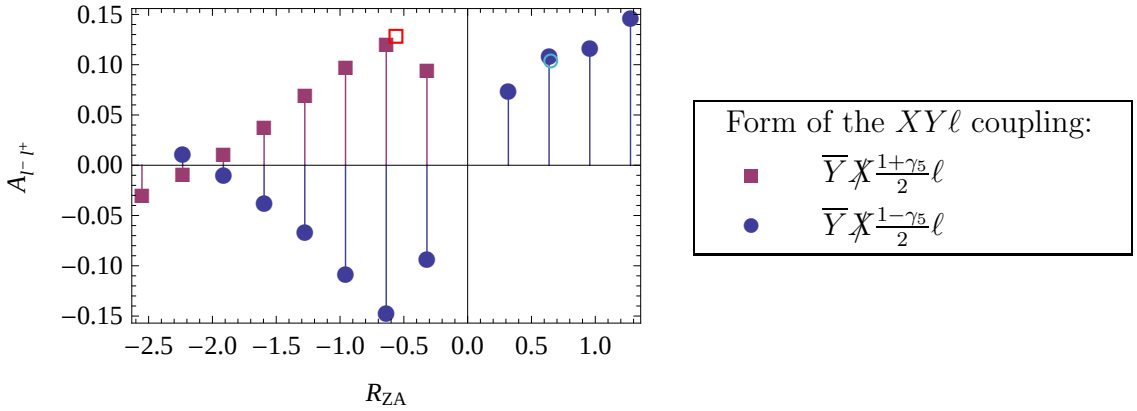

Figure 4.3: *Relationship between the coupling ratio $R_{\mathrm{ZA}} = g(ZYY)/e$ and the asymmetry $A_{\ell^+\ell^-}$, for two different chiralities of the interaction in the $Y^\pm \to \ell^\pm X^0$ decay, where Y is a fermion and X is a vector boson. The combinations 6 and 9 in Tab. 4.1 are indicated by the open square and circle, respectively. The plot is based on parton-level results without cuts and detector effects, and using the mass values $m_Y = 300$ GeV and $m_X = 100$ GeV.*

As discussed in the previous section, the observables $\tanh(\Delta\eta_{\ell\ell}/2)$, M_{eff}, and $\Delta\phi_{\ell\ell}$, see eqs. (4.3)–(4.5) can be used to determine the spin s_Y of the parent particle Y. I have checked this by performing a 5-bin χ^2 analysis for a sample of 5000 events for each model combination, assuming Poisson statistics for the statistical error. Table 4.3 shows the results for combinations 3 (with scalar Y), 10 (with fermion Y), and 11 (with vector Y) as examples. For the case of vector Y particles, results for two sample values of the t-channel fermion mass $m_{\hat{Q}}$ are given. As evident from the table, by combining the three observables, one can distinguish all three spin combinations from each other with a significance of more than 18 standard deviations, for the given choice of masses and total event count. This is true even for relatively small values of $m_{\hat{Q}} \sim \mathcal{O}(0.5\ \mathrm{TeV})$.

I have checked that the results are very similar if combinations 3 or 10 are replaced by any of the other combinations with spin-0 or spin-1/2 Y particles, respectively. Furthermore, for any two models with identical s_Y the distributions for all three variables are statistically consistent, irrespective of the spin of X.

To discriminate between models with identical s_Y but different SU(2) representations of the Y and X particles one can take advantage of the charge asymmetry $A_{\ell^+\ell^-}$ in (4.6). As explained in the previous section, one cannot obtain a non-zero asymmetry if the Y particles are scalars, and I have confirmed this statement explicitly with my simulation results. However, for $s_Y = \frac{1}{2}$, $A_{\ell^+\ell^-}$ can yield useful information about the structure of the ZYY and $XY\ell$ couplings. Results for the total asymmetry, without cuts or acceptance effects, are given in Tab. 4.4 for all combinations with fermionic Y in Tab. 4.1.

In general, $A_{\ell^+\ell^-}$ becomes maximal for events with large values of $\cos\theta^*_{\ell\ell} =$

Variable	(model A, model B)				
	(3,10)	(3,11) [$M_{\hat{Q}}$=1 TeV]	(3,11) [$M_{\hat{Q}}$=0.5 TeV]	(10,11) [$M_{\hat{Q}}$=1 TeV]	(10,11) [$M_{\hat{Q}}$=0.5 TeV]
$\tanh(\Delta\eta_{\ell\ell}/2)$	19.0	18.6	26.0	2.4	8.0
$M_{\rm eff}$	37.5	3.9	25.1	30.7	9.5
$\Delta\phi_{\ell\ell}$	16.3	21.4	10.7	41.1	29.0
All combined	37.5	18.6	26.0	41.1	29.0

Table 4.3: *$\sqrt{\chi^2}$ values for a 5-bin χ^2-test to discriminate between pairs of model combinations with different spin of the parent Y particle. The combinations 3, 10, and 11 from Tab. 4.1 have been chosen as examples of models with Y particles of spin 0, $\frac{1}{2}$, and 1, respectively.* Model B *is assumed to represent the simulated "data", while* model A *is the test hypothesis. The results are based on samples of 5000 parton-level events without cuts and detector effects, and using the input values m_Y = 300 GeV, m_X = 100 GeV, and $\sqrt{s}$ = 14 TeV.*

Combination from Tab. 4.1	4	5	6	7	8	9	10
$A_{\ell^+\ell^-}$	0.20	−0.22	0.13	0.17	−0.18	0.10	0.20

Table 4.4: *Values for the asymmetry $A_{\ell^+\ell^-}$ for combinations with fermionic Y in Tab. 4.1 based on simulated parton-level events for m_Y = 300 GeV, m_X = 100 GeV, and $\sqrt{s}$ = 14 TeV.*

$\tanh(\Delta\eta_{\ell\ell}/2)$ close to 1, *i. e.* when the Y^+Y^- pair is produced in the forward/backward direction. However, this correlation between $A_{\ell^+\ell^-}$ and $\tanh(\Delta\eta_{\ell\ell}/2)$ depends to a lesser extent also on spin effects in the decay $Y \to \ell X$ and thus can be markedly different for models with opposite chirality of the $XY\ell$ vertex. As a result, the significance for distinction between such models is increased by performing a binned analysis for the distribution $dA_{\ell^+\ell^-}/d\tanh(\Delta\eta_{\ell\ell}/2)$. It turns out that the highest sensitivity is obtained by using just two bins.

Table 4.5 lists the statistical significances for discriminating between any pair of the combinations 4–10 from Tab. 4.1 based on this observable. Models that have different signs for $A_{\ell^+\ell^-}$ can be distinguished with more than 20 standard deviations for an signal event sample of 5000 events (bold face numbers in the table).

However, the combinations 4, 7, and 10, as well as 6 and 9, are indistinguishable at the three-sigma level (gray italic numbers in the table). It turns out that also when considering any other variables in eqs. (4.2)–(4.5) one cannot achieve a higher significance for discriminating between these models.

Note that the variable $A_{\ell^+\ell^-}$ has some sensitivity to distinguish between models which differ only through the spin of the X particle, *i. e.* between combinations 4 and

		model A					
		4	5	6	7	8	9
model B	5	**36**					
	6	4.9	**29**				
	7	*1.6*	**33**	2.9			
	8	**32**	3.5	**26**	**29**		
	9	6.7	**27**	*1.5*	4.7	**23**	
	10	*0.3*	**37**	5.8	*2.2*	**33**	7.6

Table 4.5: *Statistical significance, in units of standard deviations, for the discrimination between combinations with fermionic Y in Tab. 4.1 using the differential asymmetry $dA_{\ell^+\ell^-}/d\tanh(\Delta\eta_{\ell\ell}/2)$. Numbers in bold face indicate a difference of at least 20 standard deviations, while gray italic numbers denote a significance of less than three standard deviations. The results are based on samples of 5000 parton-level events without cuts and detector effects, and using the input values $m_Y = 300$ GeV, $m_X = 100$ GeV, and $\sqrt{s} = 14$ TeV.*

6, or 7 and 9 in Tab. 4.1. Assuming a signal sample of 5000 events, as in Tab. 4.5, a discrimination significance of about five standard deviations or more can be achieved for these pairs.

4.3.5 Simulation results

The analysis in the previous section does not take into account detector effects and signal selection cuts. To determine how these might affect the results I have passed the parton-level events generated by CompHEP [40] through Pythia 6.4 [42] and PGS4 [43]. By including initial-state radiation and parton showering in the Pythia simulation one can furthermore evaluate whether fluctuations of the initial-state transverse momentum might wash out the characteristic features for the model discrimination.

In Ref. [37] it has been shown that the selection cuts

$$\begin{aligned} &N(\ell^+) = N(\ell^-) = 1, \quad m_{\ell\ell} > 150 \text{ GeV}, \quad \max\{p_{\text{T},\ell^\pm}\} > 40 \text{ GeV}, \quad \min\{p_{\text{T},\ell^\pm}\} > 30 \text{ GeV}, \\ &\not{p}_\text{T} > 100 \text{ GeV}, \quad M_{\text{T}2} > 100 \text{ GeV}, \quad |\not{\mathbf{p}}_\text{T} + \mathbf{p}_{\text{T},\ell^+} + \mathbf{p}_{\text{T},\ell^-}| < 100 \text{ GeV}, \\ &p_{\text{T,j}} < 100 \text{ GeV}, \quad N_b = 0, \end{aligned} \tag{4.9}$$

reduce the SM background rate to about 1.6 fb. Here $N(\ell^\pm)$ denotes the number of visible leptons $\ell^\pm = e^\pm, \mu^\pm$ in the central detector, N_b denotes the number of vertex b tags, $m_{\ell\ell}$ is the di-lepton invariant mass, and $p_{\text{T,j}}$ refers to the transverse momentum of any reconstructed jets. With these cuts one obtains a selection efficiency for the

Variable	(model A, model B)				
	(3,10)	(3,11) [$M_{\hat{Q}}$=1 TeV]	(3,11) [$M_{\hat{Q}}$=0.5 TeV]	(10,11) [$M_{\hat{Q}}$=1 TeV]	(10,11) [$M_{\hat{Q}}$=0.5 TeV]
$\tanh(\Delta\eta_{\ell\ell}/2)$	23.2	20.1	30.6	6.3	10.1
M_{eff}	40.0	9.7	24.2	36.8	12.6
$\Delta\phi_{\ell\ell}$	27.2	15.5	6.0	40.7	23.8
All combined	40.0	20.1	30.6	40.7	23.8

Table 4.6: *$\sqrt{\chi^2}$ values for a 5-bin χ^2-test to discriminate between pairs of model combinations with different spin of the parent Y particle, for a sample of 5000 events passing the detector simulation and selection cuts in eq.* (4.9)*. The notation and input parameters are the same as in Tab. 4.3.*

signal process $pp \to Y^+Y^- \to \ell^+\ell^- XX$ between 27% and 40%, depending on the specific type of Y and X particle. As listed in the appendix A, this corresponds to measurable signal cross sections between about 1 fb and 200 fb. For concreteness I will assume 5000 observed events, which corresponds to the expected yield of model combination 7 for an integrated luminosity of 200 fb^{-1}. In comparison, the SM background of about 300 events is small and can be neglected.

Tables 4.6 and 4.7 summarize the significance for distinguishing between models with different Y spin and with different couplings, assuming 5000 measured events for $\sqrt{s} = 14$ TeV, $m_Y = 300$ GeV and $m_X = 100$ GeV. Overall, the obtained significances for the spin discrimination are comparable to the parton-level results in Tab. 4.3, and in a few cases the significance is even higher. This seemingly surprising outcome is related to the fact that I compare the same number of "observed" events in the previous section and in this section, but in the latter case the cuts remove part of the phase space, leaving a higher event yield in the remaining phase-space region.

For the coupling determination one finds that the asymmetry $A_{\ell^+\ell^-}$ is washed out noticeably by the cuts, leading to substantially reduced significances in Tab. 4.7 compared to Tab. 4.5. Nevertheless, models with different sign for $A_{\ell^+\ell^-}$ can still be distinguished with at least 17 standard deviations.

In summary, for most cases, selection cuts and smearing effects only moderately affect the capability for identifying particle properties with the described observables. Of course the selection cuts reduce the overall event number, which however also depends on the model-dependent total cross section and thus is left as a free parameter here.

		model A					
		4	5	6	7	8	9
model B	5	**23**					
	6	3.3	**20**				
	7	*2.0*	**22**	*1.6*			
	8	**22**	*2.1*	19	**21**		
	9	3.7	19	*1.7*	3.3	17	
	10	*1.3*	**25**	4.1	*2.1*	**23**	5.3

Table 4.7: *Statistical significance, in units of standard deviations, for the discrimination between combinations with fermionic Y using $dA_{\ell^+\ell^-}/d\tanh(\Delta\eta_{\ell\ell}/2)$. The results are based on a sample of 5000 events passing the detector simulation and selection cuts in eq.* (4.9)*, with notation and input parameters are the same as in Tab. 4.5.*

4.4 Comparison with Automated Likelihood Analysis

An alternative approach is an automated likelihood test for a sample of measured events. With such a computerized analysis method it is in general not possible to clearly separate properties like spin and couplings, but it offers the advantage of reaching a higher sensitivity by using the complete event information instead of specific observables. A very appealing realization of an automated likelihood analysis is the Matrix Element Method (MEM) [39], which uses parton-level matrix elements to specify the theoretical model that is compared with the data. The method can be used to measure one or several parameters of the model by finding the maximum of the likelihood for a sample of events as a function of the parameters. As of today, the MEM achieves the most precise determination of the top-quark mass [14] and new-physics particle masses [34].

For each single event, with observed momenta $\mathbf{p}_i^{\text{vis}}$, the MEM defines a likelihood measure that it agrees with a model for a given set of model parameters α:

$$\mathcal{P}(\mathbf{p}_i^{\text{vis}}|\alpha) = \frac{1}{\sigma_\alpha}\int dx_1 dx_2\, \frac{f_1(x_1)f_2(x_2)}{2sx_1x_2}\left[\prod_{i\in\text{final}}\int\frac{d^3p_i}{(2\pi)^3 2E_i}\right]|M_\alpha(p_i)|^2\prod_{i\in\text{vis}}\delta(\mathbf{p}_i-\mathbf{p}_i^{\text{vis}}). \tag{4.10}$$

Here f_1 and f_2 are the parton distribution functions, M_α is the theoretical matrix element, and σ_α is the total cross section, computed with the same matrix element. The three-momenta $\mathbf{p}_i^{\text{vis}}$ of the visible measured objects are matched with the corresponding momenta $\mathbf{p}_i$ of the final state particles in the matrix element, while the

(model A, model B)				
(3,10)	(3,11) [$M_{\hat{Q}}$=1 TeV]	(3,11) [$M_{\hat{Q}}$=0.5 TeV]	(10,11) [$M_{\hat{Q}}$=1 TeV]	(10,11) [$M_{\hat{Q}}$=0.5 TeV]
60	59	61	85	87

Table 4.8: *Statistical significance, in units of standard deviations, for the discrimination between pairs of model combinations with different spin of the parent Y particle, based on the MEM. A sample of 5000 parton-level events without cuts and detector effects has been used. The notation and input parameters are the same as in Tab. 4.3.*

momenta of invisible particles (weakly interacting particles, such as the X particle in my case) are integrated over.

For a sample of N events, the combined likelihood is usually stated in terms of its logarithm, which in the large-N limit can be interpreted as a χ^2 value,

$$\chi^2 = -2\ln(\mathcal{L}) = -2\sum_{n=1}^{N} \ln \mathcal{P}(\mathbf{p}_{n,i}^{\text{vis}}|\alpha), \tag{4.11}$$

where $\mathbf{p}_{n,i}^{\text{vis}}$ are the measured momenta of the nth event.

The MEM is particularly useful for signals that cannot be fully reconstructed due to invisible final-state particles, and it can be applied to determine the masses of both X and Y in processes of the type in eq. (4.1) [34]. Here I will assume that the masses are already known and instead focus on the discrimination between the models in Tab. 4.1.

Matrix elements for all 11 combinations in the table have been computed with the help of CompHEP and implemented into a private code for performing the phase-space integration in (4.10). Similar to section 5.3.2 only parton-level events without cuts have been used in this analysis. Results for model comparisons are listed in Tables 4.8 and 4.9.

As can be seen from Tab. 4.8, the MEM achieves a much higher significance for discriminating between combinations with different s_Y, see Tab. 4.3 for comparison. This is not surprising since several observables, eqs. (4.3)–(4.5), were found to be sensitive to the Y spin, indicating that none of them captures all relevant information. Note also that the results in Tab. 4.8 do not depend strongly on the unknown mass of the t-channel fermion $\hat{Q}$ for combination 11.

The MEM can also distinguish between combinations that all have spin-1/2 Y particles but which differ in the SU(2) representations of X and Y, as shown in Tab. 4.9. It is interesting to note that in most cases the statistical significance achieved by the MEM is the same or only slightly better than the results obtained with the asymmetry $A_{\ell^+\ell^-}$ in Tab. 4.5. An exception is combination 10 which can be distinguished from the other combinations with substantially higher significance using the MEM compared to $A_{\ell^+\ell^-}$. This implies that the asymmetry $A_{\ell^+\ell^-}$ captures essentially all

		model A					
		4	5	6	7	8	9
model B	5	**30**					
	6	7.6	**25**				
	7	*2.5*	**29**	9.1			
	8	**30**	4.1	**27**	**29**		
	9	8.6	**26**	*3.0*	9.0	**27**	
	10	15	**44**	**22**	15	**44**	17

Table 4.9: *Statistical significance, in units of standard deviations, for the discrimination between combinations with fermionic Y in Tab. 4.1 based on the MEM. A sample of 5000 parton-level events without cuts and detector effects has been used. The notation and input parameters are the same as in Tab. 4.5.*

measurable information about the ZYY and $XY\ell$ couplings, except for the special case of model 10.

Similar to the results of the previous section, it is found that one cannot discriminate very well between combinations with Y singlets and Y doublets, *i. e.* between 4 and 7, 5 and 8, or 6 and 9[3]. Likewise, the MEM results for the combinations 1, 2, and 3 with scalar Y differ by less than one standard deviation, and thus are completely indistinguishable.

4.5 Conclusions

This chapter presents a comprehensive analysis of new physics processes of the form $pp \to Y^+Y^- \to \ell^+\ell^- X^0\bar{X}^0\,(\ell = e, \mu)$, where X^0 is stable and weakly interacting, leading to a signature of two opposite-sign same-flavor leptons and missing momentum. To minimize model assumptions, all possible combinations for the spins and weak SU(2) couplings of X and Y have been considered, allowing for spin 0, $\frac{1}{2}$ and 1, and SU(2) iso-singlets, -doublets and -triplets, see Tab. 4.1.

The signal processes have been analyzed with two different and complementary approaches. The first method is based on specific observables. Concretely, I have studied three variables for the measurement of the spins and one asymmetry for the extraction of information about the couplings of the new particles. Secondly, an automated strategy called the Matrix Element Method has been used, which algorithmically computes a likelihood that a given event sample agrees with some model interpretation supplied in the form of a theoretically calculated matrix element.

[3]Note, however, that a better differentiation between these cases would in principle be possible with more statistics, requiring significantly larger amounts of integrated luminosity.

It has been found that the spin s_Y of the parent particle Y can be determined with high statistical significance, so that a sample of a few hundred signal events is sufficient for discrimination at the 5σ-level. Furthermore, it was shown that the asymmetry $A_{\ell^+\ell^-}$ defined in eq. (4.6) is instrumental in distinguishing between model combinations that all have $s_Y = \frac{1}{2}$ but different Y and X couplings. The majority of possible coupling assignments can be differentiated with high significance, but it turns out that for cases 4 and 7, as well as 6 and 9 in Tab. 4.1 one cannot achieve a 3σ discrimination with a realistic number of a few thousand events. This is related to the fact that the relationship between the ZYY coupling strength and the observable asymmetry is not monotonic and can involve degenerate solutions. Remarkably, the same model combinations are also difficult to distinguish with the Matrix Element Method, which demonstrates that the asymmetry $A_{\ell^+\ell^-}$ reflects all relevant information about the couplings of the underlying model.

For $s_Y = 0$ it is generally impossible to discriminate between cases with different couplings or with different spin of the X particles, due to the absence of spin correlations between the production and decay stages of the process. For $s_Y = 1$ the coupling structure of the process is essentially fixed by gauge invariance and thus already uniquely known once the vector nature of Y has been determined.

my findings indicate that even for the challenging case of a process with a short, one-step decay chain it is in general possible to separately determine the spins and couplings of the new heavy particles. The results in this chapter have been presented for the specific choice of masses $m_Y = 300$ GeV and $m_X = 100$ GeV, but I have checked explicitly that the essential features are unchanged for $m_Y = 200$ GeV. While the main goal of this study was the development of the theoretical framework and conceptual ideas, I have also performed a fast detector simulation with selection cuts for the suppression of standard model backgrounds and found that qualitatively my conclusions still hold. Nevertheless, a dedicated experimental simulation with a careful evaluation of systematic errors, including the influence of uncertainties in the Y and X masses, would be required to check the viability of my results under realistic conditions.

Chapter 5

General analysis of decay chains with three-body decays involving missing energy

A large range of models have been proposed that predict new particles within the reach of the LHC. Since there is currently very little evidence for favoring one model over the others, it will be essential to analyze a potential new-physics signal in the LHC data in a model-independent approach, by independently determining the properties of each of the produced particles. Recently, this idea has gained increased interest, and several groups have worked on constructing such model-independent setups for a number of different observable signatures, see *e. g.* Refs. [44–47]. A particularly challenging scenario are processes that result in the production of new weakly interacting massive particles (WIMPs), which are invisible to the detector. WIMPs are predicted in many models as hypothetical dark matter candidates. In these models, the stability of the WIMP is a consequence of some (discrete) symmetry, under which it is charged. As a result, it can be produced only in pairs at colliders, leading to challenging events with at least two invisible objects. At hadron colliders like the LHC there are not enough kinematical constraints in events of this type for the direct reconstruction of the momenta of all particles involved.

One approach to this problem is motivated by the fact that models predict additional new particles, which can decay into the stable WIMP. In this case, one can have cascade decay chains, which go through multiple decay steps before ending with the stable WIMP, so that one can construct invariant-mass distributions of the visible decay products of this cascade. The kinematic endpoints of these distributions yield information about the masses [32, 49, 50] of the new heavy particles, while the shape is sensitive to their spins [44, 45, 51, 52]. Refs. [44, 45] have analyzed decay chains built up from a sequence of two-body decays in a model-independent way, by considering arbitrary spin assignments [44] and also using general parametrizations for the coupling for the new particles [45].

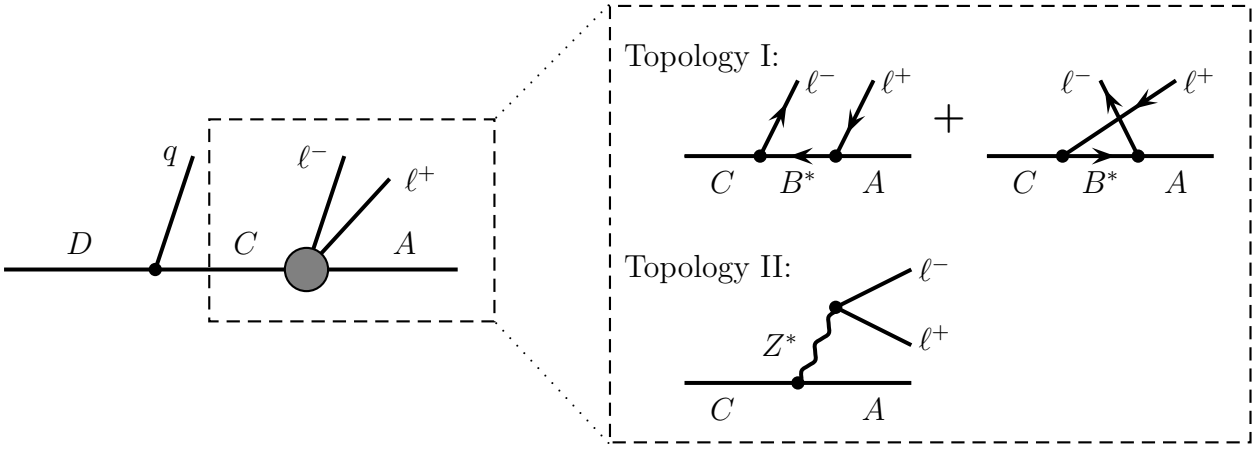

Figure 5.1: *Right: Three-body decays involving an off-shell new-physics particle B (topology I) or an off-shell Z boson (topology II). Left: The three body decay could occur as the last step of a longer decay chain.*

However, for scenarios with relatively small splittings in the mass spectrum of the new-physics particles, it can often happen that the last decay step is a three-body decay mediated by a heavier off-shell particle, see right-hand side of Fig. 4.1. Some typical scenarios where this occurs in the context of supersymmetry are listed in the appendix B. In Ref. [53], three-body decays have been analyzed in order to distinguish gluinos, the supersymmetric partners of gluons, from a Kaluza-Klein (KK) gluons in universal extra dimensions (UED). A model-independent study of three-body decays has been presented in Ref. [54], but only in the limit of an asymptotically large mass of the intermediate off-shell particles. In typical supersymmetry and UED scenarios, however, this limit is often not a good approximation.

In this work, three-body decays of the form $C \to \ell^+\ell^- A$ will be analyzed in a model-independent setup without assumptions about the values of the masses of the new-physics particles. Here C is a massive new particle that decays into the WIMP A and two SM leptons $\ell^\pm = e^\pm, \mu^\pm$ through the off-shell exchange of a third new particle B or the SM Z-boson, see Fig. 5.1[1]. The spins of A, B, and C, their coupling parameters, and the mass m_B of the particle B will be kept as free quantities that have to be extracted from the experimental data. I only impose the constraint $m_B > m_C$, or $m_Z > m_C - m_A$, to ensure that I have an actual three-body decay. Without these constraints the three-body decay would decompose into two two-body decays, which is a scenario that has been discussed in detail in the literature cited above.

Furthermore, I also consider the case that this three-body decay is the second

[1]In general, besides the Z-boson, a bosonic new-physics particle (*e. g.* a Z' or a Higgs boson) may also appear in the decay topology II. However, the branching of such a particle into leptons is strongly constrained by data on four-fermion contact interactions [55], and thus its contribution will be neglected here.

step of a cascade decay of the form $D \to \overset{(-)}{q}\, C \to \overset{(-)}{q}\, \ell^+\ell^- A$, where $\overset{(-)}{q}$ refers to a SM quark (antiquark), see Fig. 5.1. Such a decay chain would lead to two independent observable invariant-mass distributions, a di-lepton ($\ell^+\ell^-$) invariant-mass distribution, and a jet-lepton ($j\ell^\pm$) invariant-mass distribution, where the jet emerges from the fragmentation of the quark or antiquark.

For both of these cases, I investigate the simultaneous determination of the spins and couplings of the new particles A, B, C and D from the shapes of these distributions. The determination of the masses from kinematic endpoints has been discussed elsewhere [32, 49, 82], and here I will simply assume that the masses of the particles A, C and D are already known. On the other hand, the mass m_B of the off-shell intermediate particle B can not be extracted from the kinematic endpoints, and I will study if instead it can be constrained from the shapes of the distributions.

My analysis closely follows the conventions of Ref. [45]. After introducing the relevant spin and coupling representations in section 5.1, the calculation of the $\ell\ell$ and $j\ell$ invariant-mass distributions is described in section 5.2. In section 5.3 I present a procedure for determining the spins and couplings of the new particles, as well as the mass of the intermediate particle B, by fitting the theoretically calculated functions to the experimentally observed distributions. The method is illustrated by applying it in two numerical examples. Finally, the main conclusions are summarized in section 5.4.

5.1 Setup

The three-body decay of a heavy new particle C into two opposite-sign same-flavor leptons and a second new particle A,

$$C \to \ell^+\ell^- A, \qquad (\ell = e, \mu), \tag{5.1}$$

is mediated either by an off-shell heavy new particle B (with $m_B > m_C > m_A$) or a SM Z-boson (with $m_C - m_A > m_Z$). I also consider the possibility that eq. (5.1) occurs as the last step of a longer decay chain,

$$\begin{aligned} D \to q\, C \\ \qquad\quad \hookrightarrow \ell^+\ell^- A. \end{aligned} \tag{5.2}$$

Here D is a QCD triplet, while B and A/C are electrically charged and neutral QCD singlets, respectively. For the purpose of this work, it is assumed that A and C are self-conjugate (*i. e.* they are their own antiparticles)[2]. Furthermore, it is assumed that A, B, C, and D are charged under some symmetry which ensures that A is stable and escapes from the detector without leaving a signal.

[2]Some new physics models predict decay chains with non-self-conjugate neutral heavy particles, which lead to distinct phenomenological features [56], but this case will not be considered here.

	S	D	C	B	A	Example
Topology I	1	S	F	S	F	$\tilde{q} \to \tilde{\chi}_2^0 \to \tilde{\ell}^* \to \tilde{\chi}_1^0$
	2	F	S	F	S	$q_{(1)} \to W_{H,(1)}^0 \to \ell_{(1)}^* \to B_{H,(1)}^0$
	3	F	S	F	V	$q_{(1)} \to W_{H,(1)}^0 \to \ell_{(1)}^* \to B_{\mu,(1)}^0$
	4	F	V	F	S	$q_{(1)} \to W_{\mu,(1)}^0 \to \ell_{(1)}^* \to B_{H,(1)}^0$
	5	F	V	F	V	$q_{(1)} \to W_{\mu,(1)}^0 \to \ell_{(1)}^* \to B_{\mu,(1)}^0$
	6	S	F	V	F	
Topology II	7	F	S		S	$q_{(1)} \to W_{H,(1)}^0 \to B_{H,(1)}^0$
	8	F	S		V	$q_{(1)} \to W_{H,(1)}^0 \to B_{\mu,(1)}^0$
	9	F	V		S	$q_{(1)} \to W_{\mu,(1)}^0 \to B_{H,(1)}^0$
	10	F	V		V	$q_{(1)} \to W_{\mu,(1)}^0 \to B_{\mu,(1)}^0$
	11	S	F		F	$\tilde{q} \to \tilde{\chi}_2^0 \to \tilde{\chi}_1^0$

Table 5.1: *Possible spin configurations of the heavy particles D, C, B, and A in the decay chain of Fig. 5.1 (F=Fermion, S=Scalar, V=Vector). Also shown are examples for realizations of these assignments in the Minimal Supersymmetric Standard Model (MSSM) or in models with one or two universal extra dimension (UED). Here* $\tilde{q}$, $\tilde{\ell}$, *and* $\tilde{\chi}_i^0$ *denote squark, slepton, and neutralino, respectively.* $q_{(1)}$, $\ell_{(1)}$, $\tilde{B}_{\mu,(1)}^0$, *and* $\tilde{W}_{\mu,(1)}^{0,\pm}$ *refer to the first-level KK-excitations of quark, lepton, U(1) gauge field, and SU(2) gauge field, respectively.* $B_{H,(1)}^0$ *and* $W_{H,(1)}^0$ *are scalars stemming from one of the extra components of the higher-dimensional gauge fields in UED. More details of these models can be found in Refs. [12, 20].*

In general, it is difficult to experimentally determine the overall strength of the couplings in the decay chain since the width of weakly decaying particles is typically small compared to the experimental resolution. Consequently, only the *shape* of the observable invariant-mass distributions will be considered here, similar to earlier studies on spin determination [44, 45, 51, 53, 54]. All expressions for these distributions presented in the following sections therefore include an arbitrary, but constant, normalization factor.

Table 5.1 lists all possible spin assignments for the particles $A-D$ in any renormalizable theory with fields of spin 0 (scalars), spin 1/2 (fermions) and/or spin 1 (vector bosons). Also shown are examples for realizations of these assignments in known models.

The chirality of the fermion couplings depend on the details of the new physics and thus are a priori unknown. Following Ref. [45], I introduce arbitrary left- and right-handed components. For scalar-fermion-fermion vertices, the interaction Lagrangians

are defined as

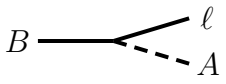

$$\overline{\psi}_B\, A\,(a_L\omega_- + a_R\omega_+)\,\psi_\ell + \text{h.c.}, \tag{5.3}$$

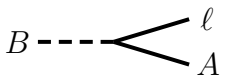

$$\overline{\psi}_A\, B\,(a_L\omega_- + a_R\omega_+)\,\psi_\ell + \text{h.c.}, \tag{5.4}$$

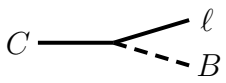

$$\overline{\psi}_C\, B\,(b_L\omega_- + b_R\omega_+)\,\psi_\ell + \text{h.c.}, \tag{5.5}$$

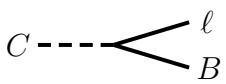

$$\overline{\psi}_B\, C\,(b_L\omega_- + b_R\omega_+)\,\psi_\ell + \text{h.c.}, \tag{5.6}$$

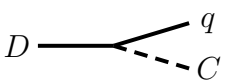

$$\overline{\psi}_D\, C\,(c_L\omega_- + c_R\omega_+)\,\psi_q + \text{h.c.}, \tag{5.7}$$

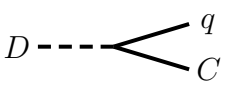

$$\overline{\psi}_C\, D\,(c_L\omega_- + c_R\omega_+)\,\psi_q + \text{h.c.}, \tag{5.8}$$

where $\omega_\pm = \frac{1}{2}(1 \pm \gamma_5)$. For vector-fermion-fermion couplings, A must be replaced by $\not{A}$ in (5.3), *etc.* After normalizing the overall coupling strength to unity, each vertex can be parametrized by a single angle α, β, or γ,

$$\begin{aligned} a_L &= \cos\alpha, \qquad b_L = \cos\beta, \qquad c_L = \cos\gamma, \\ a_R &= \sin\alpha, \qquad b_R = \sin\beta, \qquad c_R = \sin\gamma. \end{aligned} \tag{5.9}$$

As will be shown later, the entire parameter space for the couplings can be covered by restricting the angles to the intervals $\alpha \in [-\pi/2, \pi/2]$, $\beta, \gamma \in [0, \pi/2]$.

The form of the CAZ vertices is uniquely determined by Lorentz symmetry and CP properties (since the Z-boson is CP-odd, while the self-conjugate A and C are C-even):

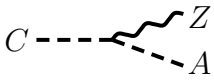

$$iC\overset{\leftrightarrow}{\partial}_\mu A\, Z^\mu, \tag{5.10}$$

$$-\,C_\mu\, A\, Z^\mu, \tag{5.11}$$

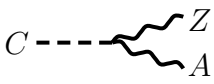

$$-\,C\, A_\mu\, Z^\mu, \tag{5.12}$$

$$(C_\mu A_\nu - A_\mu C_\nu)\partial^\mu Z^\nu + \text{cycl.}, \tag{5.13}$$

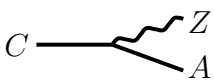

$$\overline{\psi}_C \gamma_\mu \gamma_5 \psi_A\, Z^\mu, \tag{5.14}$$

where again the coupling constants have been normalized to unity.

In an experimental analysis, it is impossible to tell on an event-by-event basis whether a quark or an antiquark is emitted in the first stage of eq. (5.2), *i. e.* whether the cascade decay was initiated by a particle D or its antiparticle $\overline{D}$. However, the observable $j\ell$ invariant-mass distribution may depend significantly on the fraction f of events stemming from D decays versus the fraction $\bar{f}$ of events stemming from $\overline{D}$ decays, with $f + \bar{f} = 1$.

As pointed out in Ref. [45], the ratio of f and $\bar{f}$ is very difficult to determine without model assumption and thus should be treated as a free parameter. The $j\ell$ distribution depends on f and $\bar{f}$ only through the combinations $f|c_L|^2 + \bar{f}|c_R|^2 = f\cos^2\gamma + \bar{f}\sin^2\gamma$ and $f|c_R|^2 + \bar{f}|c_L|^2 = f\sin^2\gamma + \bar{f}\cos^2\gamma$. It is therefore convenient to introduce the parameter $\tilde{\gamma}$, defined by [45]

$$\cos^2\tilde{\gamma} = f\cos^2\gamma + \bar{f}\sin^2\gamma, \tag{5.15}$$

$$\sin^2\tilde{\gamma} = f\sin^2\gamma + \bar{f}\cos^2\gamma. \tag{5.16}$$

From the analysis of the $j\ell$ invariant-mass distribution one can only obtain a constraint on $\tilde{\gamma}$, but not on γ and f independently.

5.2 Invariant-mass distributions

As pointed out above, it is difficult to discriminate experimentally between the decay chain in Fig. 5.1, with a quark emitted in the first stage, and its charge-conjugated version with an antiquark emitted in the first stage, since both quark and antiquark fragment into jets. Therefore the only relevant observable invariant-mass distributions are the $m_{\ell\ell}$ (lepton-lepton) distribution and the $m_{j\ell}$ (jet-lepton) distribution.

There is no distinction between the two leptons in the three-body decay, in contrast to the situation when B can be produced on-shell (*i., e.* for $m_B < m_C$) in which case one can define a "near" and a "far" lepton [32, 44, 45, 49, 51, 52, 82].

Explicit expressions for the $m_{\ell\ell}$ and $m_{j\ell}$ distributions are obtained by computing the squared matrix elements for the different spin configurations S=1–11 in Tab. 5.1 and integrating over the remaining phase space variables. A convenient choice for the phase space integration is given by

$$\frac{1}{\Gamma}\frac{d\Gamma}{dm^2_{\ell\ell}} = N_{\ell\ell}\int_{m^{\min}_{A\ell^-}}^{m^{\max}_{A\ell^-}} dm^2_{A\ell^-}\,|\mathcal{M}_3|^2, \tag{5.17}$$

$$m^{\min,\max}_{A\ell^-} = \tfrac{1}{2}[m_A^2 + m_C^2 - m^2_{\ell\ell} \mp \lambda^{1/2}(m_A^2, m_C^2, m^2_{\ell\ell})],$$

$$\frac{1}{\Gamma}\frac{d\Gamma}{dm^2_{q\ell^+}} = N_{q\ell}\int_{m_A^2}^{m_C^2[1-m^2_{q\ell^+}/(m_D^2-m_C^2)]} dm^2_{A\ell^-}\int_0^{2\pi} d\phi \tag{5.18}$$

$$\times\int_0^{(m^2_{A\ell^-}-m_A^2)(m_C^2-m^2_{A\ell^-})/m^2_{A\ell^-}} dm^2_{\ell\ell}\;\frac{1}{m_C^2 - m^2_{A\ell^-}}\,|\mathcal{M}_4|^2,$$

where $\lambda(a,b,c) \equiv a^2+b^2+c^2-2(ab+ac+bc)$. In these equations, $\mathcal{M}_{3,4}$ denote the matrix elements for the 3-body or (3+1)-body decay processes, respectively, while $m_{A\ell^-}$ is the invariant mass of particle A and one of the leptons, and ϕ is the angle between the plane spanned by the lepton-lepton system and the quark in the reference frame of C. The charge of the lepton in $m_{A\ell^-}$ and $m_{q\ell^+}$ has been specified for definiteness, but one can equally well choose the variables $m_{A\ell^+}$ and $m_{q\ell^-}$. $N_{\ell\ell}$ and $N_{q\ell}$ are unspecified normalization constants.

The observable jet-lepton distribution $d\Gamma/dm^2_{j\ell}$ is obtained from $d\Gamma/dm^2_{q\ell}$ by replacing γ with $\tilde{\gamma}$, see eqs. (5.15),(5.16).

As mentioned above, the endpoints of the invariant-mass distributions can be used to obtain information about the masses m_A, m_C and m_D of the particles that are produced on-shell in the cascade, while the shapes of the distributions depend on the couplings and spins of the particles A–D. Focusing on the latter, it is convenient to define the distributions $d\Gamma/d\hat{m}_{\ell\ell}$ and $d\Gamma/d\hat{m}_{j\ell}$ in terms of unit-normalized invariant masses

$$\hat{m}_{\ell\ell} \equiv \frac{m_{\ell\ell}}{m^{\max}_{\ell\ell}}, \qquad m^{\max}_{\ell\ell} = m_C - m_A, \tag{5.19}$$

$$\hat{m}_{j\ell} \equiv \frac{m_{j\ell}}{m^{\max}_{j\ell}}, \qquad (m^{\max}_{j\ell})^2 = \frac{1}{m_C^2}(m_D^2-m_C^2)(m_C^2-m_A^2). \tag{5.20}$$

For the spin configurations S=1–6, the dependence on the coupling parameters $\alpha, \beta, \tilde{\gamma}$ can be cast into the form

$$\begin{aligned}\frac{1}{\Gamma}\frac{d\Gamma}{d\hat{m}_{\ell\ell}} &= (\cos^2\alpha\,\sin^2\beta + \sin^2\alpha\,\cos^2\beta)\, f_1^{(\ell\ell)}(\hat{m}^2_{\ell\ell};\, m_A^2, m_B^2, m_C^2) \\ &+(\cos^2\alpha\,\cos^2\beta + \sin^2\alpha\,\sin^2\beta)\, f_2^{(\ell\ell)}(\hat{m}^2_{\ell\ell};\, m_A^2, m_B^2, m_C^2) \\ &+(\cos\alpha\,\sin\alpha\,\cos\beta\,\sin\beta)\, f_3^{(\ell\ell)}(\hat{m}^2_{\ell\ell};\, m_A^2, m_B^2, m_C^2),\end{aligned} \tag{5.21}$$

$$\begin{aligned}\frac{1}{\Gamma}\frac{d\Gamma}{d\hat{m}_{j\ell}} &= (\cos^2\alpha\,\sin^2\beta\,\cos^2\tilde{\gamma} + \sin^2\alpha\,\cos^2\beta\,\sin^2\tilde{\gamma})\, f_1^{(j\ell)}(\hat{m}^2_{j\ell};\, m_A^2, m_B^2, m_C^2, m_D^2) \\ &+(\cos^2\alpha\,\sin^2\beta\,\sin^2\tilde{\gamma} + \sin^2\alpha\,\cos^2\beta\,\cos^2\tilde{\gamma})\, f_2^{(j\ell)}(\hat{m}^2_{j\ell};\, m_A^2, m_B^2, m_C^2, m_D^2) \\ &+(\cos^2\alpha\,\cos^2\beta\,\cos^2\tilde{\gamma} + \sin^2\alpha\,\sin^2\beta\,\sin^2\tilde{\gamma})\, f_3^{(j\ell)}(\hat{m}^2_{j\ell};\, m_A^2, m_B^2, m_C^2, m_D^2) \\ &+(\cos^2\alpha\,\cos^2\beta\,\sin^2\tilde{\gamma} + \sin^2\alpha\,\sin^2\beta\,\cos^2\tilde{\gamma})\, f_4^{(j\ell)}(\hat{m}^2_{j\ell};\, m_A^2, m_B^2, m_C^2, m_D^2) \\ &+(\cos\alpha\,\sin\alpha\,\cos\beta\,\sin\beta)\, f_5^{(j\ell)}(\hat{m}^2_{j\ell};\, m_A^2, m_B^2, m_C^2, m_D^2),\end{aligned} \tag{5.22}$$

where the functions $f_i^{(\ell\ell)}$ and $f_i^{(j\ell)}$ are independent of the coupling parameters, but they contain the entire kinematical and spin information, including the dependence on the particle masses. Note that $f_3^{(\ell\ell)}$ and $f_5^{(j\ell)}$ receive contributions only from the interference term between the t- and u-channel diagrams in the upper part of Fig. 5.1, see also Ref. [53].

From eqs. (5.21),(5.22) one can see that without loss of generality the coupling parameters can be restricted to the intervals $\alpha \in [-\pi/2, \pi/2]$, $\beta, \tilde{\gamma} \in [0, \pi/2]$, as already mentioned in the previous section.

For S=7–11, the CAZ coupling is uniquely fixed up to an overall coupling constant, so that there is only one term for the lepton-lepton invariant-mass distribution. However, there are two possible terms for the jet-lepton invariant-mass distribution:

$$\frac{1}{\Gamma}\frac{d\Gamma}{d\hat{m}_{\ell\ell}} = f^{(\ell\ell)}(\hat{m}^2_{\ell\ell};\, m_A^2, m_Z^2, m_C^2), \tag{5.23}$$

$$\frac{1}{\Gamma}\frac{d\Gamma}{d\hat{m}_{j\ell}} = f_{\rm S}^{(j\ell)}(\hat{m}^2_{j\ell};\, m_A^2, m_Z^2, m_C^2, m_D^2) + \cos 2\tilde{\gamma}\, f_{\rm A}^{(j\ell)}(\hat{m}^2_{j\ell};\, m_A^2, m_Z^2, m_C^2, m_D^2), \tag{5.24}$$

The lepton-lepton distribution $d\Gamma/d\hat{m}_{\ell\ell}$ can be expressed in terms of compact analytical formulae. On the other hand, the analytical results for $d\Gamma/d\hat{m}_{q\ell}$ are very lengthy, so that instead I chose to perform the last integration step (over $m^2_{A\ell^-}$) numerically.

Explicit expressions for the functions $f_i^{(xy)}$ are available for free download (see appendix C). Figs. 5.2–5.4 depict the distribution functions for a sample mass spectrum. In the figures, the overall normalization constants have been fixed by requiring that $f_1^{(\ell\ell)}$, $f_1^{(j\ell)}$, $f^{(\ell\ell)}$, and $f_{\rm S}^{(j\ell)}$ are unit-normalized. The right column of Fig. 5.2 also illustrates how the distributions vary with the mass m_B of the off-shell intermediate particle B, for the example of the spin configuration S=1.

5.3 Analysis method

In this section I will discuss the determination of the spins and couplings parameters of the new particles, as well as the mass of the off-shell particle B, by fitting the theoretically calculated distributions to experimental data. The general procedure will be outlined in the next subsection, while its application will be demonstrated in subsection 5.3.2 for two concrete numerical examples.

5.3.1 General procedure

The analysis is based on a binned χ^2 fit for the $\ell\ell$ and $j\ell$ distributions. In this fit, the binned histogram for the data is compared with theoretical histograms obtained by numerically integrating the functions $f_i^{(\ell\ell)}$ and $f_i^{(j\ell)}$, defined in the previous section, over the interval covered by each bin. In the fit, the coupling parameters α, β, $\tilde{\gamma}$ and the mass m_B are kept as free parameters. Varying over these parameters and the spin configuration S, the best-fit result is found as the set of numbers $\{S, \alpha, \beta, \tilde{\gamma}, m_B\}$ that minimizes the χ^2 value.

During the fit procedure, for every given choice of the parameters $\{S, \alpha, \beta, \tilde{\gamma}, m_B\}$, the theoretical histograms for the $\ell\ell$ and $j\ell$ distributions are normalized such that the total number of events in the theoretical histogram agrees with the number of

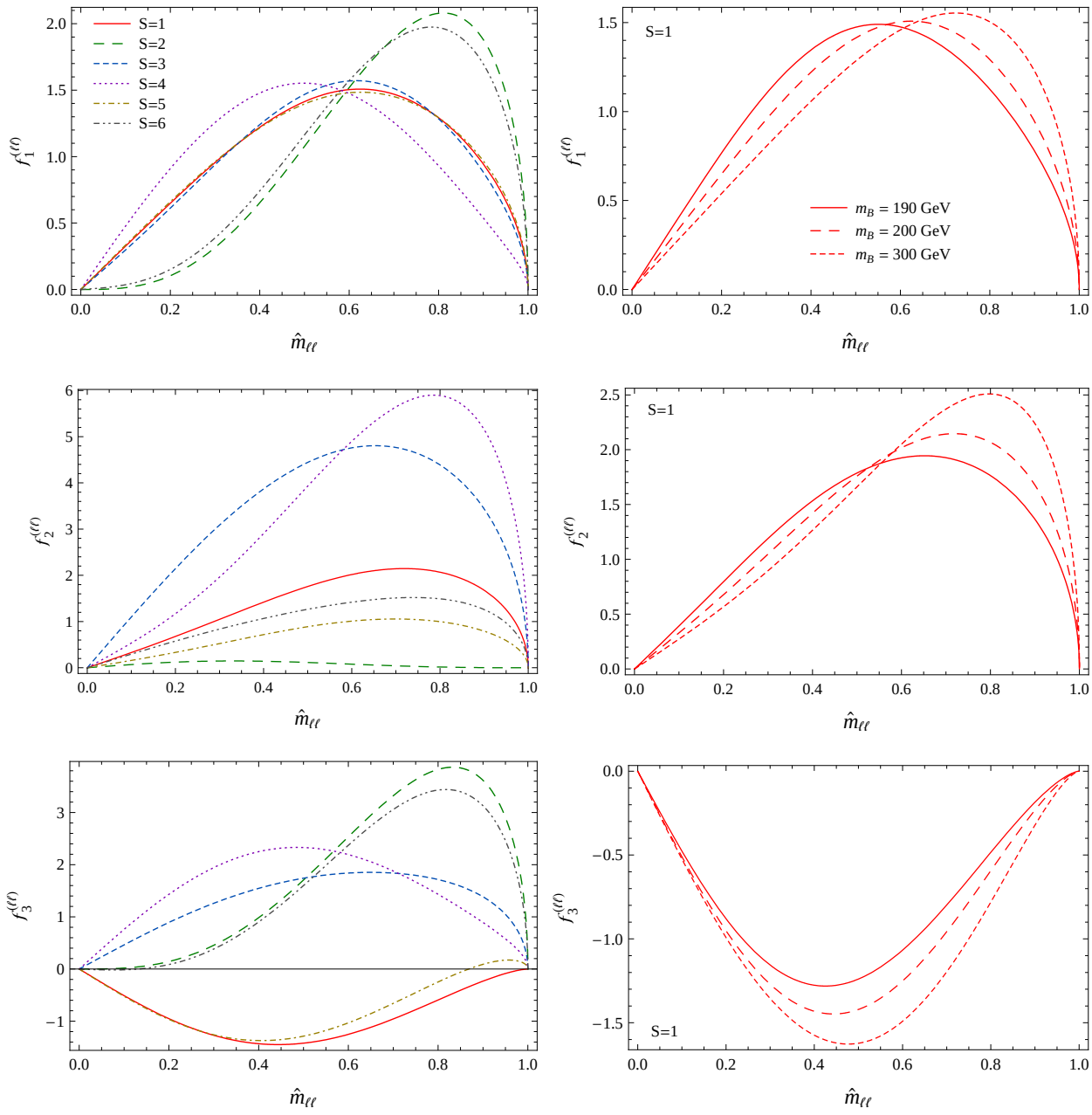

Figure 5.2: *Left: Distribution functions $f_i^{(\ell\ell)}$ $(i = 1,...,3)$ for the spin configurations S=1–6, for $m_B = 200$ GeV. Right: Dependence of $f_i^{(\ell\ell)}$ $(i = 1,...,3)$ on the mass m_B of the intermediate particle for the case S=1. The other mass parameters have been chosen as $m_C = 184$ GeV and $m_A = 98$ GeV. In these plots the overall normalization has been fixed by normalizing $f_1^{(\ell\ell)}$ to unity.*

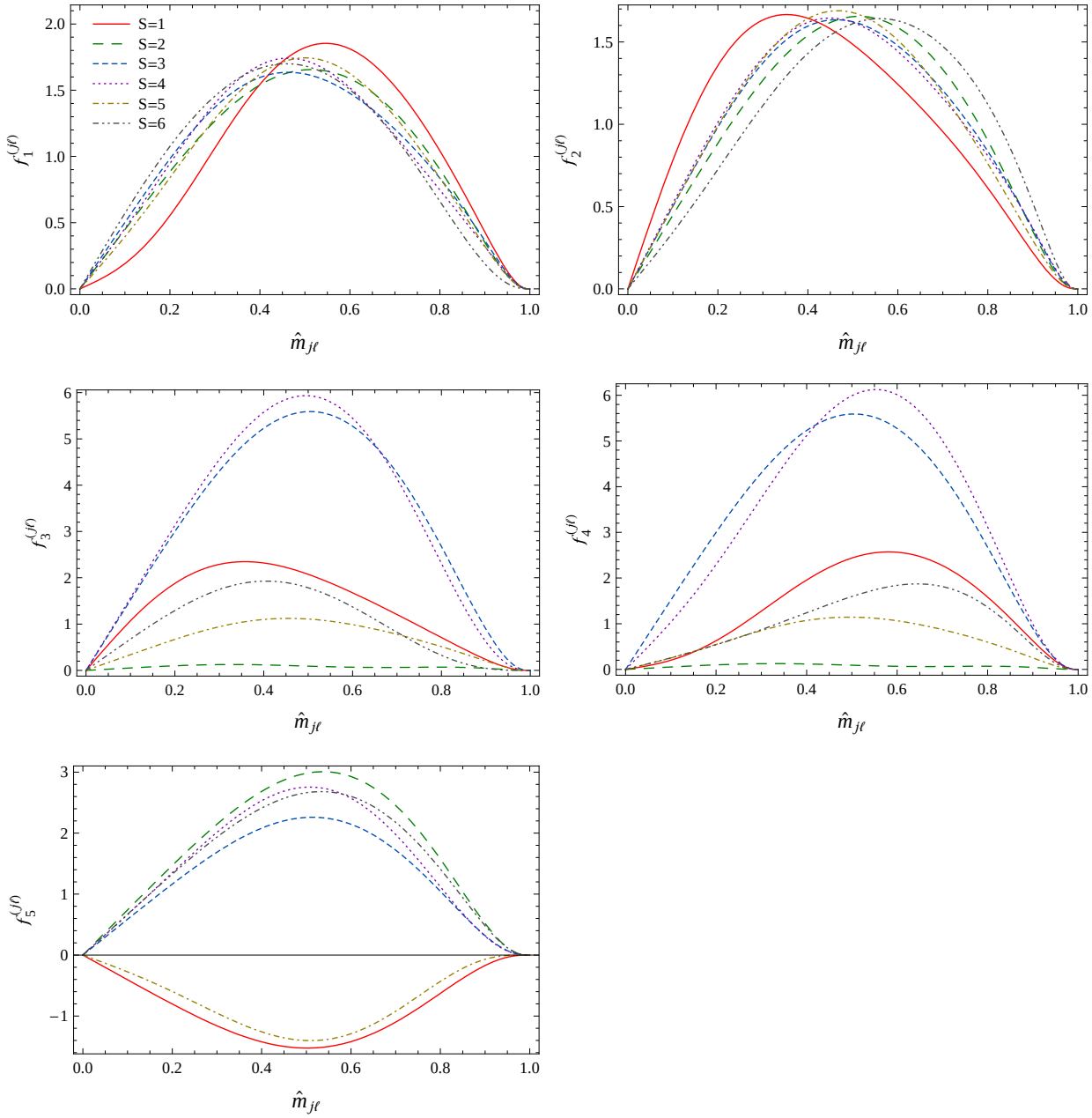

Figure 5.3: *Distribution functions $f_i^{(j\ell)}$ $(i = 1,...,5)$ for the spin configurations S=1–6. The mass parameters have been chosen as $m_D = 565$ GeV, $m_C = 184$ GeV, $m_B = 200$ GeV and $m_A = 98$ GeV. In these plots the overall normalization has been fixed by normalizing $f_1^{(j\ell)}$ to unity.*

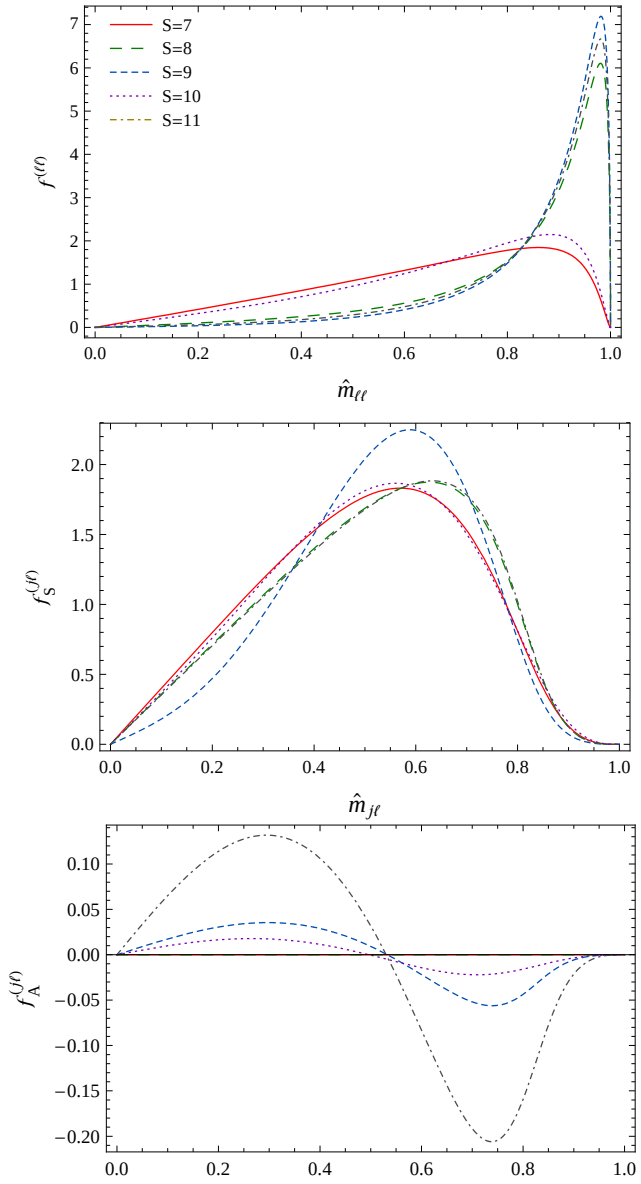

Figure 5.4: *Distribution functions $f^{(\ell\ell)}$ and $f_{\mathrm{S,A}}^{(j\ell)}$ for the spin configurations S=7–11. The mass parameters have been chosen as $m_D = 565$ GeV, $m_C = 184$ GeV and $m_A = 98$ GeV. In these plots the overall normalization has been fixed by normalizing $f^{(\ell\ell)}$ and $f_{\mathrm{S}}^{(j\ell)}$ to unity.*

events in the data histogram. In practice, this normalization is most easily carried out numerically.

In general, it may happen that there is not a unique solution for the minimum χ^2 value, but instead several degenerate best-fit points are obtained. In such a situation, the coupling parameters α, β, $\tilde{\gamma}$ and/or the spin assignment S cannot be determined uniquely from the observable distributions of the decays (5.1),(5.2) alone.

Note that the invariant-mass distributions will also depend on whether the decay proceeds through a three-body topology or a sequence of two-body decays. Therefore one can discriminate between these two possibilities by including formulas for the sequential decay chain from Refs. [44, 45] in the fit, which will however not be investigated further here.

5.3.2 Numerical examples

To illustrate the fitting procedure, its application is demonstrated by performing a fit to mock-up data histograms. This section is based on the parton-level description of the decay processes (5.1),(5.2) as described in the previous sections, thus neglecting issues such as backgrounds, jet combinatorics and energy smearing, which are relevant in a realistic experimental setup. However, earlier studies [32, 49, 57, 82] have shown that, for mass parameters similar to the ones chosen here, it is possible to obtain a clean, almost background-free sample of signal events with relatively simple selection cuts.

The major SM background after some basic cuts stems from $t\bar{t}$ production. It can be removed by using the different-flavor subtraction as described in Ref. [49], which also reduces most of the supersymmetry background. In addition, there is combinatoric background from the signal process itself, due to the difficulty of choosing the correct jet for the decay chain in Fig. 5.1 in an event with several jets. This background can be reduced by a cut on the $j\ell\ell$ invariant mass [49], and the remainder can be subtracted with the mixed event technique of Ref. [48]. Both the different-flavor subtraction and the mixed event technique do not significantly distort the invariant mass distributions (although they somewhat increase the overall statistical uncertainty), so that my analytical results will closely resemble the outcome of a more detailed simulation with cuts.

Let us consider two sample choices for the hypothetical data:

"Data" A: $S = 1, \quad \alpha = 0,\ \beta = \pi/2,\ \tilde{\gamma} = 0,$
$m_D = 565$ GeV, $m_C = 184$ GeV, $m_B = 200$ GeV, $m_A = 98$ GeV
(corresponding to the MSSM decay chain $\tilde{q}_L \to \tilde{\chi}_2^0 \to \tilde{l}_L^* \to \tilde{\chi}_1^0$);

"Data" B: $S = 11, \quad \tilde{\gamma} = 0,$
$m_D = 565$ GeV, $m_C = 184$ GeV, $m_A = 98$ GeV
(corresponding to the MSSM decay chain $\tilde{q}_L \to \tilde{\chi}_2^0 \to \tilde{\chi}_1^0$).

For each case, I have computed "data" histograms with 10 bins each for the $\hat{m}_{\ell\ell}$ and the $\hat{m}_{j\ell}$ distributions, corresponding to a fixed number of 1000 events. Then I have performed a χ^2 fit of the theoretical distribution functions to these fake "data" histogram for each of the spin configurations S=1–11, searching for the minimum χ^2 value as a function of the parameters α, β, $\tilde{\gamma}$, and m_B[3].

[3]For the spin configurations S=7–11, the non-zero Z-boson width has been included although its

a) "Data" A, using only $\hat{m}_{\ell\ell}$ distribution:

S	$N_{3\sigma}$	best-fit parameters α	β	m_B [GeV]
1 [SFSF]	–	0.00	1.57	200.0
2 [FSFS]	$\gg 10000$	-1.22	1.05	209
3 [FSFV]	$\gg 10000$	$+1.14$	0.43	197.7
4 [FVFS]	$\gg 10000$	-1.34	0.23	216
5 [FVFV]	$\gg 10000$	-0.38	0.38	197
6 [SFVF]	$\gg 10000$	-0.65	0.92	191.3

S	$N_{3\sigma}$
7 [FSS]	580
8 [FSV]	26
9 [FVS]	19
10 [FVV]	280
11 [SFF]	22

b) "Data" A, using both $\hat{m}_{\ell\ell}$ and $\hat{m}_{j\ell}$ distributions:

S	$N_{3\sigma}$	best-fit parameters α	β	$\tilde{\gamma}$	m_B [GeV]
1 [SFSF]	–	0.00	1.57	0.00	200.0
2 [FSFS]	300	-0.08	0.07	1.57	754
3 [FSFV]	520	± 1.57	1.57	0.29	210
4 [FVFS]	940	± 1.19	0.00	1.57	220
5 [FVFV]	980	-0.93	0.25	1.57	224
6 [SFVF]	1200	-0.50	0.53	1.57	197.4

S	$N_{3\sigma}$	best-fit $\tilde{\gamma}$
7 [FSS]	360	?
8 [FSV]	23	?
9 [FVS]	17	0.39
10 [FVV]	220	1.57
11 [SFF]	19	1.08

Table 5.2: *Results for fitting all spin configurations S=1–11 to (a) the $\hat{m}_{\ell\ell}$ distribution only, and (b) the $\hat{m}_{\ell\ell}$ and $\hat{m}_{j\ell}$ distributions together, using scenario "data" A for the mock-up data histograms. $N_{3\sigma}$ denotes to the number of events required for a discrimination by three standard deviations. Also shown are the best-fit parameter values, where "?" indicates that the best-fit point is independent of that parameter.*

The results are shown in Tables 5.2 and 5.3, presented in terms of the number of events required to distinguish between the "data" and the model hypothesis at the level of three standard deviations (corresponding to $\chi^2/\text{dof} = 9$). From Tab. 5.2 one can see that when only information about the $\hat{m}_{\ell\ell}$ distribution is available, it is difficult to distinguish the "data" A (based on the spin configuration S=1) from the spin configurations S=2–6. The underlying reason is that for each of these spin configurations there are three unknown continuous parameters, α, β and m_B, which can be adjusted so as to mimic the data distribution.

On the other hand, the spin configurations S=7–11 can be distinguished from "data" A with high significance, using only the $\hat{m}_{\ell\ell}$ distribution. This is a consequence of the fact that there are no free parameters to adjust in $d\Gamma/d\hat{m}_{\ell\ell}$ for S=7–11, and that these spin configurations correspond to a different diagram topology (Topology

numerical impact is not very important for the masses chosen here.

a) "Data" B, using only $\hat{m}_{\ell\ell}$ distribution:

S	$N_{3\sigma}$	best-fit parameters α	β	m_B [GeV]
1 [SFSF]	45	+0.79	0.79	∞
2 [FSFS]	81	?	?	∞
3 [FSFV]	25	?	?	∞
4 [FVFS]	49	?	?	∞
5 [FVFV]	75	$\alpha = \beta = ?$		∞
6 [SFVF]	51	± 1.57	0.00	∞

S	$N_{3\sigma}$
7 [FSS]	51
8 [FSV]	5100
9 [FVS]	9300
10 [FVV]	74
11 [SFF]	–

b) "Data" B, using both $\hat{m}_{\ell\ell}$ and $\hat{m}_{j\ell}$ distributions:

S	$N_{3\sigma}$	best-fit parameters α	β	$\tilde{\gamma}$	m_B [GeV]
1 [SFSF]	38	+0.78	0.77	0.00	∞
2 [FSFS]	65	?	?	?	∞
3 [FSFV]	20	?	?	?	∞
4 [FVFS]	41	± 1.25	0.43	1.32	∞
5 [FVFV]	60	+0.46	0.46	1.57	∞
6 [SFVF]	59	± 1.57	0.00	?	∞

S	$N_{3\sigma}$	best-fit $\tilde{\gamma}$
7 [FSS]	45	?
8 [FSV]	2900	?
9 [FVS]	1200	0.00
10 [FVV]	65	0.00
11 [SFF]	–	0.00

Table 5.3: *Same as Fig. 5.2, but using "data" B for the mock-up data histograms.*

II in Fig. 5.1 instead of topology I).

If both the $\hat{m}_{\ell\ell}$ and $\hat{m}_{j\ell}$ distributions are included in the fit, all possible spin configurations can be discriminated with at least six standard deviations, for the given number of 1000 events.

For the second example, it is evident from Tab. 5.3 that "data" B can be distinguished from all other spin configurations S=1–10 by just using the $\hat{m}_{\ell\ell}$ distribution. In fact, for all combinations except S=8 and S=9 the significance for this discrimination is very high and is not improved substantially by including the $\hat{m}_{j\ell}$ distribution in the fit. Also note that the best-fit results for S=1–6 are obtained for very large values of m_B, since increasing values of m_B shift the $\hat{m}_{\ell\ell}$ distribution toward larger values of $\hat{m}_{\ell\ell}$, see Fig. 5.2 (right), leading to better agreement with the reference case S=11, see Fig 5.4.

In addition to the spin determination, the couplings of the new particles and the mass of the off-shell B particle can in principle be extracted from the fit to the invariant-mass distributions. This is shown in Fig. 5.5 for the example of "data" A. The panels (a) and (b) in the figure depict the constraints on α, β and m_B obtained from fitting the $\hat{m}_{\ell\ell}$ distribution alone, assuming that S=1 is the correct

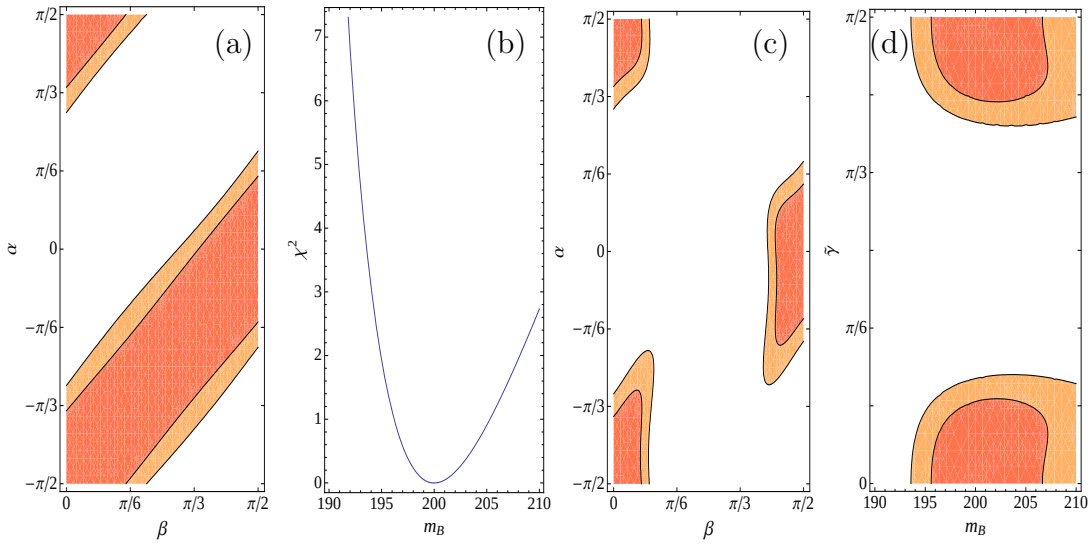

Figure 5.5: *Determination of the parameters α, β, $\tilde{\gamma}$, and m_B using only the $\hat{m}_{\ell\ell}$ distribution (a,b), and using both the $\hat{m}_{\ell\ell}$ and $\hat{m}_{j\ell}$ distributions (c,d). The dark/light bands in the figures correspond to the 68%/95% confidence-level regions. The plots correspond to a sample of 1000 events for the scenario "Data" A.*

spin configuration. If a fit to both the $\hat{m}_{\ell\ell}$ and $\hat{m}_{j\ell}$ distributions is performed, one obtains the results in panels (c) and (d). As evident from the plots, the inclusion of the $\hat{m}_{j\ell}$ distribution does not only lead to a constraint on $\tilde{\gamma}$ (which cannot be obtained from $d\Gamma/d\hat{m}_{\ell\ell}$), but also to improved bounds on α and β.

However, the fit results for the coupling parameters always have a two-fold degeneracy, since the invariant-mass distributions, eqs. (5.21)–(5.24), are invariant under the transformation $\{\alpha,\, \beta,\, \gamma\} \to \{\text{sign}\,\alpha\,(\frac{\pi}{2} - |\alpha|),\, \frac{\pi}{2} - \beta,\, \frac{\pi}{2} - \gamma\}$.

5.4 Summary

In this chapter, a general analysis of three-body decays of the form $C \to \ell^+\ell^- A$, leading to a pair of opposite-sign leptons and one invisible particle A, has been presented. This decay process can occur in many proposed new-physics models, either from direct production of the particle C at the LHC, or from a cascade decay of the type $D \to \overset{(-)}{q}\, C \to \overset{(-)}{q}\, \ell^+\ell^- A$, both of which have been studied here.

No assumptions about the masses, spins and couplings of the participating new-physics particles have been made, including the off-shell particle B mediating the three-body decay. Instead, all possible spin configurations and coupling form factors have been considered. Experimentally, the masses, spins and coupling parameters may be determined from measuring the invariant-mass distributions of the visible

decay products.

In the present case, there are two independent distributions, one with respect to the di-lepton ($\ell^+\ell^-$) invariant mass, and the other with respect to the jet-lepton ($j\ell^\pm$) invariant mass. Results for both have been obtained in terms of relatively compact analytical functions or one-dimensional integral representations.

In two concrete numerical examples, it has been tested how well the properties of the new-physics particles A, B, C and D can be determined from these two invariant-mass distributions. It turns out that the di-lepton invariant-mass distributions alone is sometimes not sufficient to uniquely determine the spins and coupling parameters. However, if the longer two-step cascade decay chain is observed, and one can measure both the $\ell^+\ell^-$ and $j\ell^\pm$ invariant-mass distributions, it is possible to unambiguously discriminate between all possible spin configuration with high significance. Furthermore, one can independently constrain all coupling parameters and the mass of the off-shell mediator B, up to an intrinsic two-fold ambiguity.

The results presented here are based on a parton-level analysis. In a realistic experimental environment, the significance for the model discrimination and the precision for the parameter determination may be diluted by jet energy smearing and combinatorics, but the essential features and main conclusions are not affected substantially by these effects, as demonstrated for example in Refs. [48, 49, 57, 82].

Chapter 6

New Physics from the Top at the LHC

6.1 Introduction

The top quark may be a window to physics beyond the Standard Model (SM). Its mass near the electroweak scale and its large coupling to the Higgs boson may be crucial to understanding the electroweak sector beyond the SM. Now that the SM-like Higgs boson has been observed at the Large Hadron Collider (LHC) [59] with a relatively light mass of about 125 GeV, the assumed "naturalness" of the Higgs sector [60], which states that the quantum corrections to the Higgs mass should be of the same order of magnitude as its physical mass, suggests the existence of a partner of the top quark below or near the TeV scale, motivating theories such as weak-scale supersymmetry, Little Higgs, and extra dimensions (either warped or universal). Vacuum stability of the electroweak potential also indicates the need for new physics to balance the large top-quark contribution. The top quark hence provides a possible early indicator of new physics and a good probe of a wide variety of new-physics scenarios.

The LHC is a top factory, producing a hundred times more $t\bar{t}$ pairs from QCD processes than were produced at the Tevatron. Top-quark production is well understood in the SM. Thus any new physics contributions will be on top of a well-known and well-measured, albeit large, background. With the discovery era ushered in by the LHC, it would be prudent to keep the initial search as general as possible.

In this work, I take a model-independent approach to searching for new physics processes of the form

$$pp \to Y\bar{Y} \to t\bar{t}XX,$$

where Y is a massive new particle with the same gauge quantum numbers as the top quark and X is an electrically and color neutral stable particle. The weakly interacting X could be a constituent of dark matter, which would manifest itself as missing energy in a collider detector. I systematically consider different spin configurations (0, 1/2, and 1) for the new particles Y and X. Each combination is exemplified by particles

in well-motivated new-physics models (see the next section for details). For example, in the Minimal Supersymmetric Standard Model (MSSM) Y could be a scalar top and X the lightest neutralino. This case has been studied extensively in the literature (see, for example, Refs. [61–67]). However, I do not limit myself to specific particles in a particular model; rather, I undertake a general categorization, assuming merely a mass accessible at the LHC and a discrete symmetry that ensure the stability of X. For simplicity, I restrict consideration to processes that involve only the top partner, Y, and the dark-matter candidate, X, as new particles.

In order to distinguish experimentally between the different possibilities, one needs to determine the spins and couplings of the new particles Y and X. In this chapter, several observables for this purpose are proposed and their usefulness is demonstrated in a realistic Monte Carlo simulation. To avoid ambiguities due to model-dependent branching fractions, I do not consider the total cross section in this set of variables.

The chapter is organized as follows. In section 6.2 I introduce the model-independent classification of new-physics top partners and their interactions. The production of these particles at the LHC is discussed in section 6.3, while the current bounds from collider searches are summarized in section 6.4. In section 6.5, the expected reach of the LHC for this class of processes is analyzed through a detailed Monte Carlo simulation. The determination of relevant properties of the new particles, such as mass, spin and couplings, and the discrimination between models are discussed in section 6.6. Finally, conclusions are presented in section 6.7.

6.2 New Particles and their Couplings to the Top

Colored particles can be copiously produced at the LHC by strong QCD interactions. Let Y denote a new color-triplet particle with charge $+2/3$. Y and its antiparticle can be produced at leading order in QCD by the processes shown in Fig. 6.1 (left). I shall not consider the production of a single new particle via Yukawa-type interactions: since they are strongly model-dependent and are subject to strong constraints from flavor physics, it is assumed that such vertices are forbidden by a discrete symmetry. Y decays to a new particle that is a color singlet, denoted X [see Fig. 6.1 (right)], which will show as missing energy in a collider experiment.

There are four possible combinations of spins that allow a coupling between X, Y and the SM top quark, t. These are listed, with the relevant couplings and sample model decays, in Table 6.1. For fermions I allow a general chirality structure. I shall henceforth refer to these scenarios as models i, ii, iii, and iv.

Let us elaborate on the unusual case in which Y is a vector color triplet, possibly arising as a bound state from strong dynamics or from a special kind of supersymmetric model [68]. The kinetic term is

$$\mathcal{L}_{\text{kin}} = -\frac{1}{2}(F_{\mu\nu})^\dagger F^{\mu\nu}\,, \qquad F_{\mu\nu} = D_\mu Y_\nu - D_\nu Y_\mu\,, \tag{6.1}$$

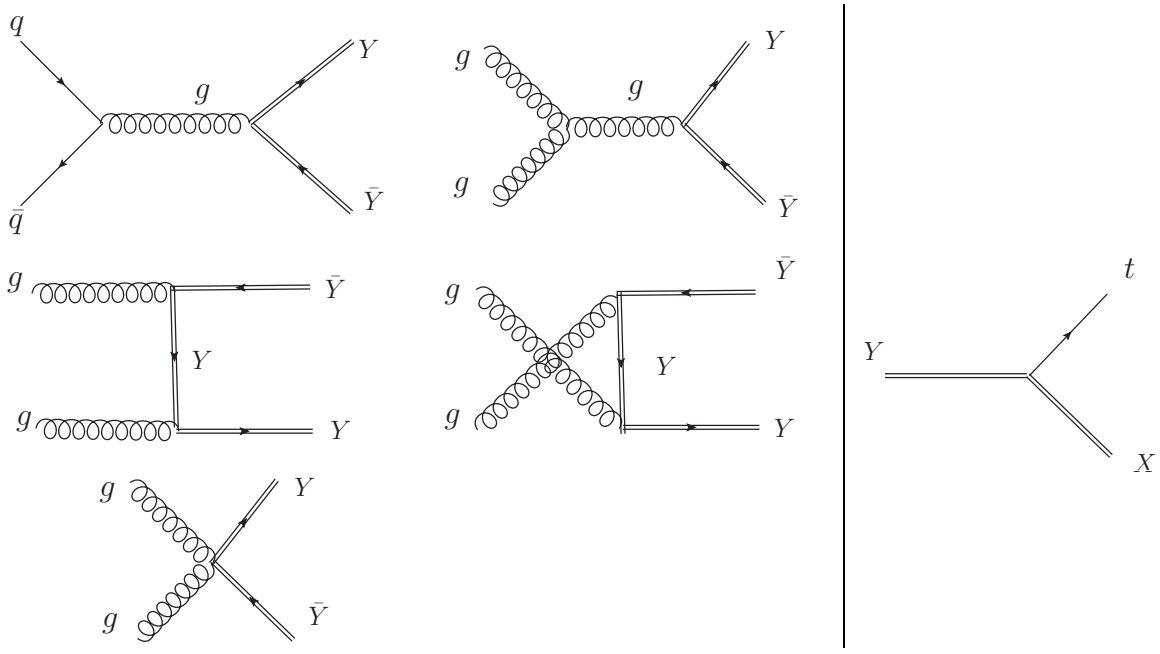

Figure 6.1: *Diagrams corresponding to the pair production (left) and the decay (right) of the color triplet Y. Double lines denote new particles, while single lines denote SM particles.*

	Y $J_Y,\ I_{\mathrm{SU}(3)}$	X $J_X,\ I_{\mathrm{SU}(3)}$	GYY coupling	XYt coupling	sample model and decay $Y \to tX$
i	0, **3**	$\frac{1}{2}$, **1**	$G^{a\mu}Y^*\overleftrightarrow{\partial_\mu}T^aY$	$\overline{X}\Gamma t\,Y^*$	MSSM $\quad \tilde{t} \to t\tilde{\chi}_1^0$
ii	$\frac{1}{2}$, **3**	0, **1**	$\overline{Y}\not{G}^aT^aY$	$\overline{Y}\Gamma t\,X$	UED $\quad t_{\mathrm{KK}} \to t\gamma_{H,\mathrm{KK}}$
iii	$\frac{1}{2}$, **3**	1, **1**	$\overline{Y}\not{G}^aT^aY$	$\overline{Y}\not{X}\Gamma t$	UED $\quad t_{\mathrm{KK}} \to t\gamma_{\mathrm{KK}}$
iv	1, **3**	$\frac{1}{2}$, **1**	$S_3[G,Y,Y^*]$	$\overline{X}\not{Y}^*\Gamma t$	[68] $\quad \vec{Q} \to t\tilde{\chi}_1^0$

$$\Gamma \equiv a_L P_L + a_R P_R\,, \quad A\overleftrightarrow{\partial_\mu}B \equiv A(\partial_\mu B) - (\partial_\mu A)B$$
$$S_3[G,Y,Y^*] \equiv T^a\left[G^a_\mu\, Y^*_\nu \overleftrightarrow{\partial^\mu} Y^\nu + G^a_\mu\, Y^{\mu *}\overleftarrow{\partial^\nu} Y_\nu - G^a_\mu\, Y^*_\nu \overrightarrow{\partial^\nu} Y^\mu\right]$$

Table 6.1: *Quantum numbers and couplings of the new particles X and Y, which interact with the SM top quark, t. In the last column, $\tilde{t}$ and $\tilde{\chi}_1^0$ are the scalar top and lightest neutralino in the MSSM, respectively [20]. t_{KK}, γ_{KK}, and $\gamma_{H,\mathrm{KK}}$ are the first-level Kaluza-Klein excitations of the top, the photon, and an extra-dimensional component of a photon, respectively, in universal extra dimensions (UED) [12]. Finally, $\vec{Q}$ is the vector superpartner in a supersymmetric model with an extended gauge sector [68].*

where $D_\mu = \partial_\mu - igT_a G^a_\mu$. Then the Y-Y-gluon interaction term is

$$\mathcal{L}_{YYG} = \frac{1}{2} ig (T_a)_{ji} \left((\partial^\mu \bar{Y}^\nu_j - \partial^\nu \bar{Y}^\mu_j)(G^a_\mu Y_{\nu i} - G^a_\nu Y_{\mu i}) - \text{h.c.} \right) . \tag{6.2}$$

The resulting Feynman rule is

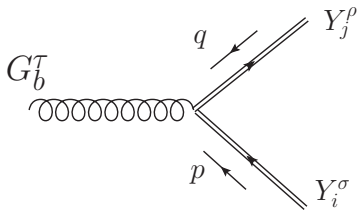

$$= ig (T_b)_{ji} \left((q-p)^\tau g^{\sigma\rho} + p^\rho g^{\sigma\tau} - q^\sigma g^{\rho\tau} \right) . \tag{6.3}$$

Likewise, the Y-Y-gluon-gluon interaction term is

$$\mathcal{L}_{YYGG} = -\frac{g^2}{2} (G^\mu_b \bar{Y}^\nu - G^\nu_b \bar{Y}^\mu) T_b T_a (G^a_\mu Y_\nu - G^a_\nu Y_\mu) . \tag{6.4}$$

The resulting Feynman rule is

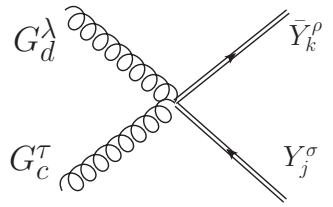

$$= -ig^2 \left((T_c T_d + T_d T_c)_{kj} g^{\tau\lambda} g^{\rho\sigma} - (T_c T_d)_{kj} g^{\tau\sigma} g^{\lambda\rho} - (T_d T_c)_{kj} g^{\tau\rho} g^{\lambda\sigma} \right) . \tag{6.5}$$

6.3 Color-Triplet Top-Partner Production

The dominant modes for production of the top partner in hadronic collisions are the QCD subprocesses

$$q\bar{q} \, , gg \to Y\bar{Y} . \tag{6.6}$$

I restrict myself to the first- and second-generation quarks $q = u, d, c, s$ and use the CTEQ 6L1 parton distribution functions (PDFs) [69], with the factorization scale set to m_Y. For $m_Y \sim$ 200–1000 GeV, the dominant subprocess is $gg \to Y\bar{Y}$, which is about one order of magnitude larger than $u\bar{u}, d\bar{d} \to Y\bar{Y}$. The channels $c\bar{c}, s\bar{s} \to Y\bar{Y}$ are suppressed by roughly one additional order of magnitude.

The total QCD production cross section at the LHC as a function of the mass of the Y is shown in Fig. 6.2, for the cases in which Y has spin 0, 1/2, and 1. The plots include next-to-leading order (NLO) and resummed next-to-leading logarithmic (NLL) QCD corrections for the scalar Y [70] and NLO and NNLL corrections for

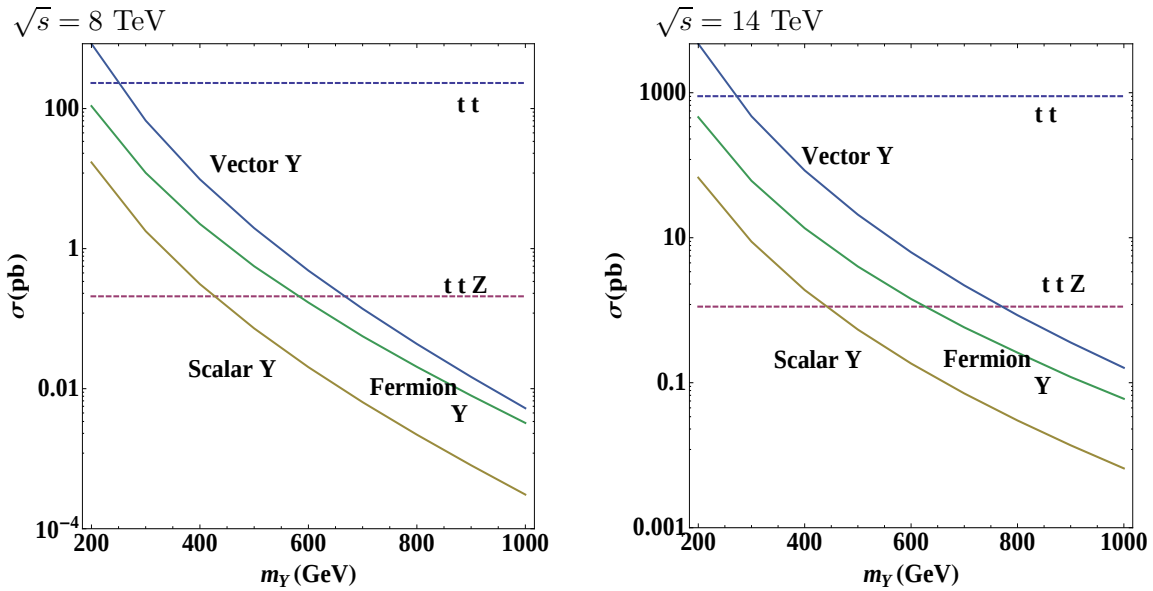

Figure 6.2: *Production cross sections for $pp \to Y\bar{Y}$ at the LHC for 8 TeV (left) and 14 TeV (right), as a function of the mass m_Y, for different Y spins. The leading SM backgrounds are indicated by horizontal lines.*

the fermionic Y [71]. The QCD corrections for vector Y production have not yet been calculated; I use the K-factor for the scalar Y (1.77 at $\sqrt{s} = 8$ TeV, 1.56 at $\sqrt{s} = 14$ TeV), since the two cases share similar leading-order Feynman diagrams.

The cross section for the fermion is about an order of magnitude larger than that of the scalar, because of the fermion's extra spin degrees of freedom and threshold effects. In the s-channel, the scalar is produced as a p-wave with a velocity dependence of $\sigma \sim \beta^3$, whereas the fermion is produced as an s-wave with $\sigma \sim \beta$. Thus, the ratio of the cross sections of the fermion and scalar is larger at small values of β, that is, when the mass of the Y is large. This relative enhancement of the fermionic $Y\bar{Y}$ production is particularly pronounced when the Y particles are produced mostly near the threshold limit. Note that, although the curves for the vector and scalar appear to be parallel on the logarithmic scale, their ratio varies from about 34 to 16 in the mass range shown.

6.4 Current Bounds from the Tevatron and LHC

As Fig. 6.1 indicates, the top-quark partner, Y, decays to a top quark plus a neutral particle, X. The discrete symmetry implies that X is stable and leads to missing-energy events. Thus, the signal is $t\bar{t}$ plus missing energy. Searches for supersymmetric scalar tops at the Tevatron [72, 73] and the LHC [74–76] put constraints on the allowed parameter space for the class of processes considered here. Additional, though

J_Y	Limit on m_Y
0	$\gtrsim 500$ GeV
1/2	$\gtrsim 650$ GeV
1	$\gtrsim 730$ GeV

Table 6.2: *Experimental bounds on the mass of particle Y for different spins, J_Y, under the assumption $m_Y \gg m_X$. These estimates are based on the ATLAS results from Refs. [75].*

generally weaker, bounds also arise from general searches for signals with jets and missing energy [77].

Currently, the strongest constraints arise from scalar top searches at ATLAS using 4.7 fb^{-1} of data taken at $\sqrt{s} = 7$ TeV [75]. For $m_Y \gg m_X$, they put a lower bound $m_Y \gtrsim 500$ GeV on a scalar Y. By taking into account the different production cross sections for scalars, fermions, and vectors (see Fig. 6.2), one can translate the results of Refs. [75] into a limit of $m_Y \gtrsim 650$ GeV for a fermionic top partner and $m_Y \gtrsim 730$ GeV for a vector top.

The bounds are summarized in Table 6.2. It should be pointed out that the limits for fermionic and vector Y are simple estimates from theoretical considerations. For more robust results, a detailed experimental analysis of these scenarios needs to be performed.

For larger values of m_X, that is, smaller mass differences $m_Y - m_X$, the limits become weaker. The excluded region in the m_Y–m_X mass plane for scalar Y particles will be shown in the next section (see Fig. 6.4).

6.5 Signal Observability at the LHC

As the previous section discusses, I consider new physics signals of the type $t\bar{t} + \not{E}$. For the leading channel, in which the top quarks decay hadronically [61], the signal receives large backgrounds from SM processes with multiple QCD jets. To suppress QCD backgrounds, I consider the semileptonic channel [62], in which one of the tops decays hadronically and the other decays leptonically, namely,

$$pp \to Y\bar{Y} \to tX\ \bar{t}X \to bj_1j_2\ \bar{b}\ell^-\bar{\nu}_\ell\ XX + \text{h.c.} \qquad (\ell = e, \mu). \tag{6.7}$$

This channel is beneficial because of its sizeable branching fraction and the identification of both t and $\bar{t}$. The dominant background processes are

$$t\bar{t}, \quad t\bar{t}Z \text{ (with } Z \to \nu\bar{\nu}), \quad \text{and} \quad Wb\bar{b}jj \text{ (with } W \to \ell\nu_\ell). \tag{6.8}$$

The cross sections for the first two backgrounds (without branching fractions) are shown in Fig. 6.2 as horizontal lines, including NLO corrections for $t\bar{t}Z$ [78] and NLO+NNLL effects for $t\bar{t}$ [79].

The separation of signal and background in the semileptonic channel has been studied previously in the literature [62, 63, 72, 74–76]. Here, I reanalyze the signal selection with the purpose of developing optimized selection cuts in a phenomenologically realistic simulation setup. My signal selection follows the strategy of Ref. [62], but I include QCD parton showering and detector smearing effects. As a result, I find that I need to adjust the choice of cuts to account for the effect of QCD radiation[1].

Jets have been clustered via a cone algorithm with cone size 0.4. To simulate detector resolution effects, I have smeared the jet energy with a Gaussian distribution of width $0.5 \times \sqrt{E}$, where E is the jet energy in units of GeV. A b-tagging efficiency of 70% [80] has been assumed. I have applied the following set of cuts to identify the signal signature and reduce the SM backgrounds.

$$\begin{aligned} &\text{exactly one lepton } \ell = e, \mu \text{ with } E_T^\ell > 20 \text{ GeV}, \ |\eta_\ell| < 2.5; \\ &\text{at least two light jets with } E_T^j > 25 \text{ GeV}, \ |\eta_j| < 2.5; \\ \textit{Cut(1):} \quad &\text{exactly two b-tagged jets with } E_T^b > 30 \text{ GeV}, \ |\eta_b| < 2.5; \\ &\Delta R_{jj}, \Delta R_{bj}, \Delta R_{bb} > 0.4, \qquad \Delta R_{\ell j} = \Delta R_{\ell b} = 0.3; \\ &70 \text{ GeV} < m_{jj} < 90 \text{ GeV}, \quad 120 \text{ GeV} < m_t^{\rm had} < 180 \text{ GeV}; \\ &\not{E} > 25 \text{ GeV}. \end{aligned} \tag{6.9}$$

Here b and j stand for a jet with or without a b-tag, and E_T^i and η_i are the transverse energy and pseudorapidity of object i. $\Delta R = \sqrt{(\Delta\eta)^2 + (\Delta\phi)^2}$ describes the angular separation between two jets. $m_t^{\rm had}$ is computed from either the bjj or the $\bar{b}jj$ invariant mass, namely, whichever yields the value closer to the true top-quark mass, m_t, in a given event. $\not{E}$ is the missing transverse energy.

Events for the partonic signal process and $t\bar{t}Z$ background have been generated with CalcHEP 3.2.5 [81] and passed to Pythia 6.4 [42] for parton showering and jet clustering. The $t\bar{t}$ background has been simulated with Pythia. It was shown in Ref. [62] that the $Wb\bar{b}jj$ background can be reduced effectively with invariant-mass cuts on the jj for a W selection and bjj for a top-quark selection. I have thus neglected this process in my simulation.

With the set of cuts in (6.9), which I shall refer to as *Cut(1)*, a good signal-to-background ratio is achieved for small values of m_Y, when the $Y\bar{Y}$ production cross section is large. For larger values of m_Y, additional cuts are required to suppress the SM background sufficiently. It turns out that the following two variables are useful for this purpose: the missing transverse energy, $\not{E}$, and the transverse mass of the lepton–missing-momentum system,

$$M_T^{\ell,\rm miss} \equiv \sqrt{(E_{\ell T} + \not{E})^2 - (\mathbf{p}_{\ell T} + \not{\mathbf{p}}_T)^2}. \tag{6.10}$$

The optimal cut values depend on the collider energy:

[1] Very recently, several papers have appeared that pursue a similar goal in the context of the

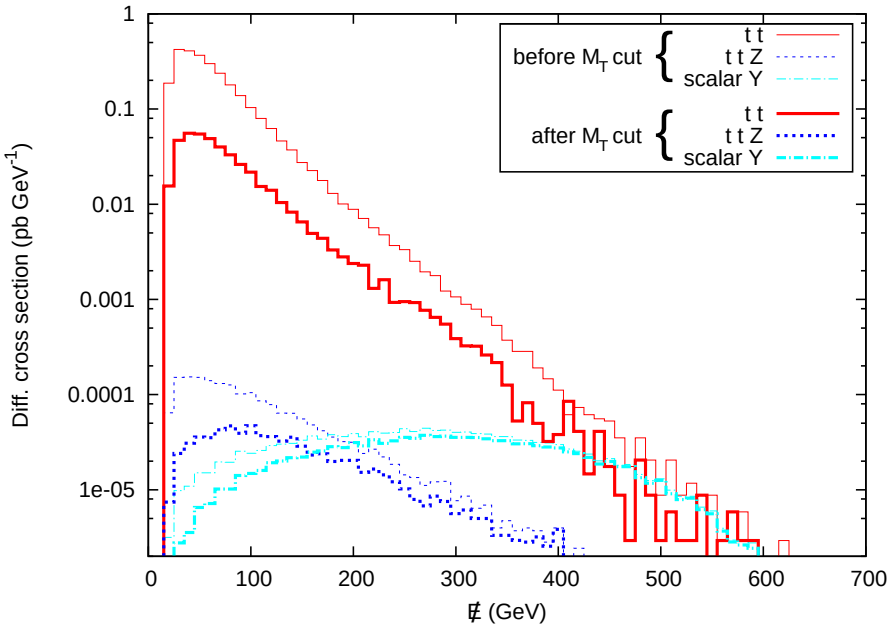

Figure 6.3: *Differential cross sections for the SM backgrounds $t\bar{t}$ (red, solid) and $t\bar{t}Z$ (blue, dashed) and the signal scalar Y with $(M_Y, M_X) = (600, 10)$ GeV (cyan, dash-dotted) before and after the cut $M_T^{\ell,\mathrm{miss}} > 90$ GeV. Distributions after the $M_T^{\ell,\mathrm{miss}}$ cut are shown in bold lines.*

- For $\sqrt{s} = 14$ TeV, the choice

  $$\textit{Cut(2h)} \quad = \quad \textit{Cut(1)} \quad \text{plus} \quad \not{E} > 350 \text{ GeV} \quad \text{and} \quad M_T^{\ell,\mathrm{miss}} > 90 \text{ GeV}$$

  has been found to be effective for $m_Y \sim 600$ GeV. It can be understood as follows. The cut $M_T^{\ell,\mathrm{miss}} > 90$ GeV is necessary because a large amount of missing energy in the SM backgrounds corresponds to neutrinos from the leptonic decay of the W boson. From Fig. 6.3 one can see that the $M_T^{\ell,\mathrm{miss}}$ cut reduces the SM backgrounds dramatically, especially in the low-$\not{E}$ region. However, the signal events remain virtually the same after this cut: only those in the low-$\not{E}$ region are slightly affected. Moreover, for the signal there is a plateau between 200 and 400 GeV in Fig 6.3. The cut $\not{E} > 350$ GeV has been chosen because above 350 GeV the backgrounds are suppressed considerably. In practice, I have applied either *Cut(1)* or *Cut(2h)*, whichever produces the larger statistical significance $S/\sqrt{B}$ for a given parameter point (m_Y, m_X). Here, S and B denote the number of signal and background events after cuts.

- For $\sqrt{s} = 8$ TeV, I have used either *Cut(1)*, or

  $$\textit{Cut(2l)} \quad = \quad \textit{Cut(1)} \quad \text{plus} \quad \not{E} > 200 \text{ GeV} \quad \text{and} \quad M_T^{\ell,\mathrm{miss}} > 145 \text{ GeV},$$

MSSM, using traditional selection cuts [64, 66] and top-jet tagging techniques [65]. The results for the signal observability are comparable to Refs. [64, 65], but significantly better than Ref. [66].

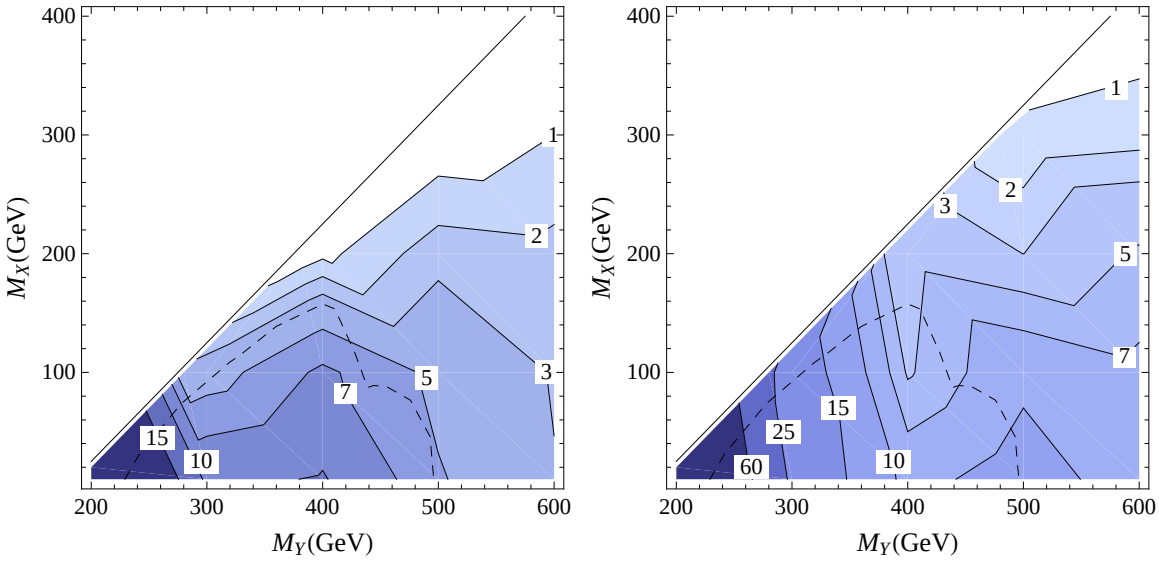

Figure 6.4: *Expected statistical significance for model i, as a function of the masses of X and Y. The left panel corresponds to $\sqrt{s} = 8$ TeV and $\mathcal{L} = 20$ fb^{-1}, while the right panel corresponds to $\sqrt{s} = 14$ TeV and $\mathcal{L} = 100$ fb^{-1}. The dashed line shows the current exclusion limit at the 95% confidence level from Ref. [75].*

or

$$\textit{Cut(2l')} \quad = \quad \textit{Cut(1)} \quad \text{plus} \quad \not{E} > 300 \text{ GeV} \quad \text{and} \quad M_T^{\ell,\text{miss}} > 185 \text{ GeV},$$

whichever results in the largest significance. *Cut(2l)* and *Cut(2l')* have been optimized for $m_Y \sim 400$ GeV and $m_Y \sim 500$ GeV, respectively.

Because the signal cross section is lower for $\sqrt{s} = 8$ TeV than for $\sqrt{s} = 14$ TeV, I have lowered the $\not{E}$ cut to ensure that a sufficient number of signal events passes. However, the looser $\not{E}$ cut also results in a larger background event yield, so that it is advantageous to apply a stronger cut on $M_T^{\ell,\text{miss}}$ to improve the signal significance.

Figure 6.4 shows the statistical significance that can be achieved with these cuts for model i (scalar Y and fermionic X), for different values of m_Y and m_X. The significance is determined according to $S/\sqrt{B}$ if $B > 10$, whereas Poisson statistics is used for very low event yields ($B \lesssim 10$). For the other model combinations, ii–iv, the statistical significance can be obtained by scaling the values in Fig. 6.4 with the production cross sections in Fig. 6.2.

As the figure shows, the statistical significance is relatively large in the following two regions of the mass plane:

1. Small values of m_Y, in which case the signal selection efficiency is almost independent of m_X. Here, the $Y\bar{Y}$ pair, which recoils against an initial-state

$\sqrt{s}$	spin-0	spin-1/2
8 TeV	480 GeV	660 GeV
14 TeV	675 GeV	945 GeV

Table 6.3: *The 5σ discovery reach for spin-0 and spin-1/2 top partners at 8 and 14 TeV with integrated luminosities of 20 and 100 fb^{-1}, respectively. $m_X = 100$ GeV is assumed.*

jet, is typically produced with a sizeable boost. This boost leads to a fairly large missing momentum, which helps to discriminate the signal from the $t\bar{t}$ background.

2. Moderately large values of m_Y, $m_Y \lesssim 600$ GeV, and small values of m_X. For these values of m_Y, the $Y\bar{Y}$ pair is produced mostly at rest and the signal selection becomes difficult for small mass differences $m_Y - m_X$, when the top quark from the decay $Y \to tX$ is quite soft.

In comparison with Ref. [62], I obtain somewhat lower values for the significance $S/\sqrt{B}$, as a consequence of having performed a more realistic simulation that includes QCD radiation (through parton showering) and jet smearing. These effects make it more difficult to devise clean kinematic selection variables for the signal and result in more background from the tail of smeared distributions. I have also explored the mass reconstruction scheme proposed in Ref. [62] and the variable M_{T2} [32]. I have found them to be useful in certain respects and complementary to the combination of my cuts. Further optimization would depend on detailed (experimental) simulations, which I leave for future studies.

In summary, I have found that, at 14 TeV with an integrated luminosity of 100 fb^{-1}, a scalar top partner can be observed at the 5σ level (or better) for a mass up to 675 GeV if $M_X = 100$ GeV. This translates into 945 GeV for a spin-1/2 top partner. At 8 TeV with an integrated luminosity of 20 fb^{-1}, it is possible to achieve a 5σ discovery for a scalar top with a mass up to 480 GeV. This corresponds to 660 GeV for a spin-1/2 top partner. These results are summarized in Table 6.3.

6.6 Determination of Model Properties

6.6.1 Masses

The independent determination of the Y and X masses in processes of the type

$$pp \to Y\bar{Y} \to f\bar{f}XX, \tag{6.11}$$

where f is a SM fermion, is a difficult problem because of the lack of kinematic features for the under-constrained system. Several methods have been proposed in

the literature [32, 49, 82–84], either based on global event variables such as $M_{\text{eff}} = \sum_{i\in\text{vis.}} p_{T,i} + \not{p}_T$, on the variable $M_{\text{T2}} = \min_{\mathbf{p}_{T,X_1}+\mathbf{p}_{T,X_2}=\not{\mathbf{p}}_\text{T}} \left\{\max\left(M_\text{T}^{\ell^+,X_1}, M_\text{T}^{\ell^-,X_2}\right)\right\}$ [11] or variants thereof, or on likelihood fits to the complete event information [39]. It was found that, for $m_Y \sim \mathcal{O}(300\text{ GeV})$ and a sample of a few tens of thousands of signal events at $\sqrt{s} = 14$ TeV, the mass difference $m_Y - m_X$ can be determined to a precision of a few per cent, while the absolute mass scale has an uncertainty of roughly 20–30% [49,83]. If the $Y\bar{Y}$ state could arise from the decay of a new resonance of known mass, it would help to constrain the kinematics and thus to determine the masses of Y and X as well [84]. More details can be found in the cited papers.

6.6.2 Spin

The spin of the Y particle can be probed through the characteristics of the $Y\bar{Y}$ production process. For instance, the $Y\bar{Y}$ production cross section strongly depends on the spin [38]. However, unknown model-dependent branching fractions and the mass uncertainty of order 30% can lead to ambiguities in the determination of the spin from the measured total production rate. Instead, one can largely avoid such problems by investigating the shape of suitable differential distributions. In particular, the two variables described below are effective for this purpose.

(1) Scalar and fermion Y pair production can be distinguished with the observable

$$\tanh(\Delta y_{t\bar{t}}/2), \qquad \Delta y_{t\bar{t}} = |y_{bjj} - y_{b\ell}|, \tag{6.12}$$

which is constructed from the rapidities of the visible decay products of the hadronically decaying and the leptonically decaying top quarks. In general, there is a combinatorial ambiguity in identifying the b-jets and light-flavor jets as the decay products from one of the two top quarks. Given the event reconstruction scheme discussed in the previous section, one can resolve this ambiguity by assuming that the hadronically decaying top quark is made up from the two light-quark jets and the b-jet for which m_{bjj} is closest to m_t. The remaining b-jet and the lepton are then identified as the decay products of the other top quark.

The variable in (6.12) is closely related to the proposal by Barr in Ref. [37], $\tanh(|\eta_f - \eta_{\bar{f}}|/2)$, where η_f is the pseudorapidity of the SM fermion from the decay $Y \to Xf$. This variable approximately traces the production angle θ^* between one Y and the beam axis in the center-of-mass frame. In the $q\bar{q} \to Y\bar{Y}$ channel, the θ^* distribution has a clear dependence on the Y spin, as can be seen in the formulae

$$\frac{d\sigma}{d\cos\theta^*}[q\bar{q} \to Y\bar{Y}] \propto 1 - \cos^2\theta^*, \qquad \text{for scalar } Y \text{ (spin 0)}, \tag{6.13}$$

$$\frac{d\sigma}{d\cos\theta^*}[q\bar{q} \to Y\bar{Y}] \propto 2 + \beta_Y^2(\cos^2\theta^* - 1), \quad \text{for fermionic } Y \text{ (spin } \tfrac{1}{2}\text{)}, \tag{6.14}$$

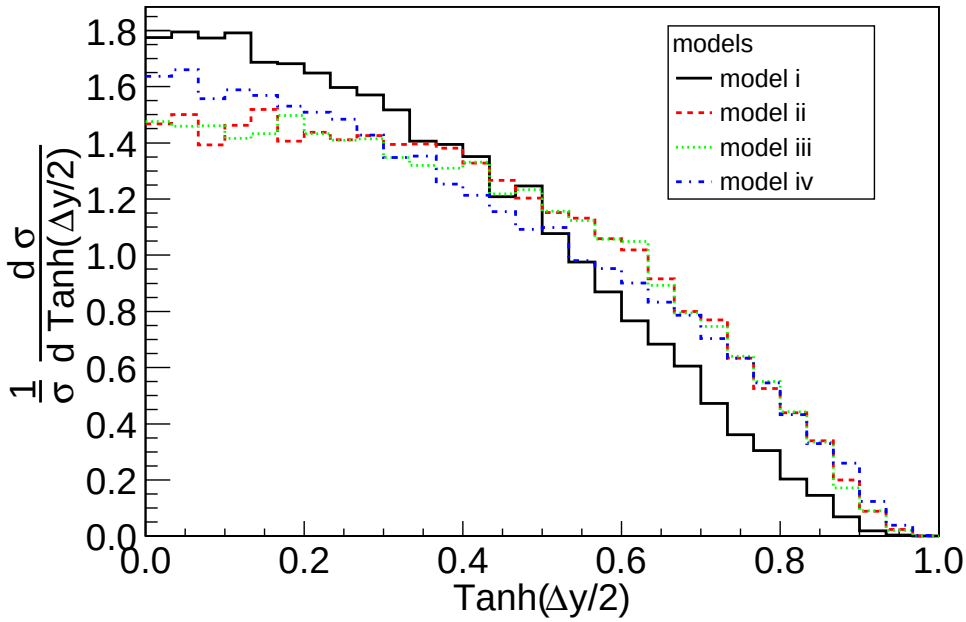

Figure 6.5: *Distribution of* $\tanh(\Delta y_{t\bar{t}}/2)$ *for the different top-partner scenarios listed in Table 6.1, for* $m_Y = 300$ GeV, $m_X = 100$ GeV, *and* $\sqrt{s} = 14$ TeV. *For comparison, all distributions have been normalized to unity.*

where β_Y is the velocity of the produced Y particles. The difference stems from the fact that scalars are produced in a p-wave, whereas for fermions the s-wave contribution is dominant. In contrast to Ref. [37], the definition (6.12) is based on the rapidities rather than the pseudorapidities, to account for the fact that the produced top quarks are massive.

In the physical process $pp \to Y\bar{Y}$, only a subdominant fraction of the events originates from $q\bar{q}$ annihilation, but as can be seen in Fig. 6.5 the effect is still noticeable (compare the lines for model i with the other cases).

(2) There is no appreciable difference between fermionic and vector Y pair production in the $\tanh(\Delta y_{t\bar{t}}/2)$ distribution. However, these two cases can be disentangled by means of a variable that measures the effective hard scattering energy [46]. One such observable is the effective mass, a scalar sum over momenta:

$$M_{\text{eff}} = \sum_{i \in \text{vis.}} p_{T,i} + \not{p}_T, \tag{6.15}$$

where the sum runs over all visible objects (jets and leptons in this case).

The usefulness of this variable follows from the fact that the partonic cross section for the pair production of massive vector particles grows with the partonic

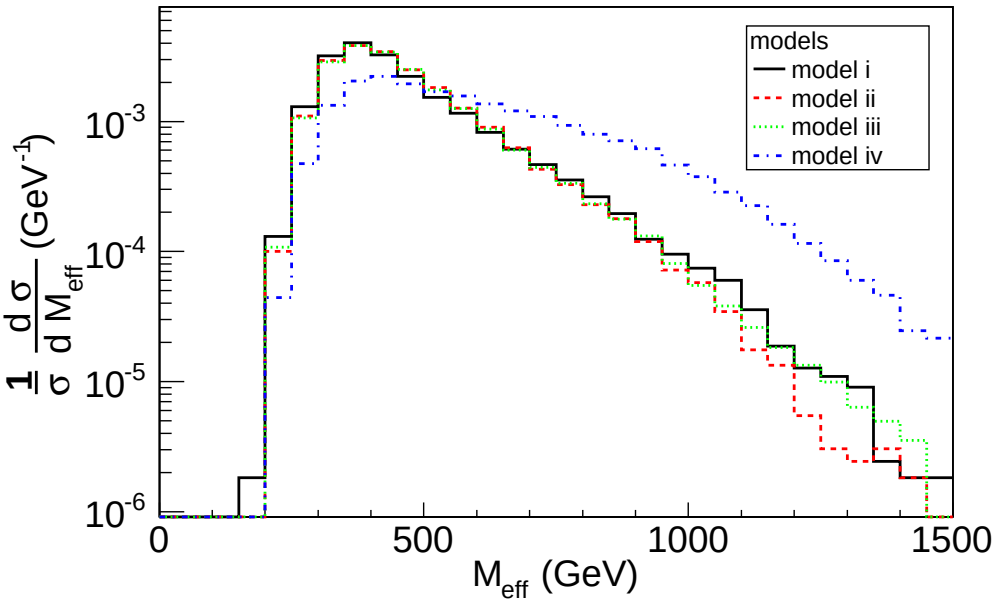

Figure 6.6: *Distribution of M_{eff} for the different top-partner scenarios listed in Table 6.1, for $m_Y = 300$ GeV, $m_X = 100$ GeV, and $\sqrt{s} = 14$ TeV. For comparison, all distributions have been normalized to unity.*

center-of-mass energy like $\hat{s}/m_Y^4$, whereas for fermions it has the usual $1/\hat{s}$ behavior in the high-energy limit. In fact, for very large values of $\hat{s}$ the vector $Y\bar{Y}$ production would violate the perturbative unitarity limit, a sign that additional new massive resonances will appear and modify the production amplitude. The presence of such resonances is generally expected in dynamical models such as the one proposed in Ref. [68]. However, their masses may be beyond the reach of the LHC, depending on the value of $\hat{s}$ when the unitarity limit is eventually reached. I have estimated this limit for vector Y pair production, conservatively assuming s-channel dominance in obtaining $\hat{s} \gtrsim (4.8 \text{ TeV})^2$. Thus, one can assume that the new heavy resonances have masses of $\mathcal{O}(5 \text{ TeV})$, which make their potential contribution to the process $pp \to Y\bar{Y}$ completely negligible, since only a fraction of order 10^{-6} of events have partonic center-of-mass energy of this size or larger at $\sqrt{s} = 14$ TeV.

The M_{eff} distribution is shown in Fig. 6.6 for the different model scenarios. A very distinctive difference can be observed between the cases of vector and fermionic or scalar top partners.

Let us quantify the discriminative power of these variable in an example: the process $pp \to Y\bar{Y} \to t\bar{t}XX$ for $m_Y = 300$ GeV and $m_X = 100$ GeV at $\sqrt{s} = 14$ TeV. The simulation and event selection have been performed as described in the previous section, with *Cut(1)* in Eq. (6.9). I have assumed the cross section for scalar Y pair

production (model i). Note that this scenario is not ruled out by current LHC results. I have not used the total event rate for model discrimination, to avoid ambiguities due to unknown branching fractions.

I have carried out the discrimination between two different spin assignments by computing the χ^2 value for the binned $\tanh(\Delta y_{t\bar{t}}/2)$ and M_{eff} distributions, using three bins in both cases. The result can be expressed in terms of the integrated luminosity $\mathcal{L}_{5\sigma}$ necessary for achieving a 5σ statistical significance:

$$\begin{aligned} \text{14 TeV:}\quad & \text{scalar } Y \text{ versus fermion } Y\text{:} && \mathcal{L}_{5\sigma} = 9.4 \text{ fb}^{-1}, \\ & \text{scalar } Y \text{ versus vector } Y\text{:} && \mathcal{L}_{5\sigma} = 0.8 \text{ fb}^{-1}, \\ & \text{fermion } Y \text{ versus vector } Y\text{:} && \mathcal{L}_{5\sigma} = 0.7 \text{ fb}^{-1}. \end{aligned}$$

For the current 8 TeV run, a 5σ discrimination requires the following integrated luminosities:

$$\begin{aligned} \text{8 TeV:}\quad & \text{scalar } Y \text{ versus fermion } Y\text{:} && \mathcal{L}_{5\sigma} = 72 \text{ fb}^{-1}, \\ & \text{scalar } Y \text{ versus vector } Y\text{:} && \mathcal{L}_{5\sigma} = 8.1 \text{ fb}^{-1}, \\ & \text{fermion } Y \text{ versus vector } Y\text{:} && \mathcal{L}_{5\sigma} = 5.2 \text{ fb}^{-1}. \end{aligned}$$

The numbers refer to the purely statistical significance. However, at this level of precision, systematic errors may be important. A potentially large systematic effect stems from the uncertainty of the new-particle masses, m_Y and m_X. While the mass difference $m_Y - m_X$ can be determined rather precisely, the overall mass scale can be measured with only 20–30% accuracy; see section 6.6.1. I have estimated the effect of this uncertainty by comparing two event samples with $(m_Y, m_X) = (300, 100)$ GeV and $(m_Y, m_X) = (400, 200)$ GeV, which differ in m_Y by roughly 30%. I have found that this mass uncertainty reduces the statistical significance of the spin discrimination by about 20%; the values of $\mathcal{L}_{5\sigma}$ that account for this systematic error are about 50% greater than those quoted above.

In conclusion, the determination of the spin of the top partner, Y, is possible with very moderate amounts of data. On the other hand, the distinction between models ii and iii, which both have a fermionic Y but differ in the spin of the singlet X, is much more difficult. After surveying more than a dozen different kinematic variables based on the top-quark momenta, I found no significant difference between scenarios ii and iii for any of them. This finding agrees with the results of Ref. [46].

However, more information can be obtained from observables that are sensitive to the top-quark polarization, as will be discussed next.

6.6.3 *XY* Couplings

The chirality structure of the decay $Y \to tX$ (that is, the relative contributions of left- and right-handed chiral couplings) leaves an imprint on the polarization of the top quark, which can be analyzed through angular distributions of the top-quark decay products. This method is particularly effective when the mass difference between Y

and X is large ($m_Y - m_x \gg m_t$), so that the top quark is energetic and therefore the helicity is preserved, reflecting the chirality. For instance, one can look at the angle θ'_b (θ'_ℓ) of the b quark (lepton) with respect to the top-quark boost direction in the top rest frame. Because the b quark is always left-handed, it is emitted predominantly in the forward direction ($\cos\theta'_b > 0$) if the top quark is left-handed, but mostly in the backward direction ($\cos\theta'_b < 0$) if the top quark is right-handed.

In practice, even if the top quark is produced fully polarized in the decay $Y \to tX$, some of the polarization is washed out by the mass of the top, but the $\cos\theta'_b < 0$ distribution will still exhibit a characteristic difference between left- and right-handed XYt couplings.

In the following, I shall illustrate this behavior using a parton-level simulation with CalcHEP[2]. I shall focus on the leptonically decaying top quark, since it has a cleaner final state. The top-quark rest frame cannot be reconstructed because of the unobserved neutrino momentum, so I analyze the angular distribution in the rest frame of the visible $b\ell$ system instead. The results are shown in Fig. 6.7.

As Fig. 6.7 shows, the distribution is skewed to smaller values of $\cos\theta'_\ell$ or, equivalently, larger values of $\cos\theta'_b$ in the case of a left-handed XYt coupling (black curves) than in the right-handed case (red curves). For a mixed case with non-zero left- and right-handed components, one obtains a distribution that lies between the black and red curves. This qualitative behavior is the same for all four spin combinations in Table 6.1, although they differ from each other in the detailed shape of the distribution. In particular, cases ii and iii have distinctly different shapes; hence, the analysis of this observable may allow one to determine not only the chirality of the XYt coupling but also the spin of the X particle. Such a determination is not possible with observables that treat the top quarks as basic objects.

Furthermore, one can probe the chirality even with limited statistics by using two bins and forming the asymmetry

$$A(x) = \frac{\sigma(\cos\theta'_\ell > x) - \sigma(\cos\theta'_\ell < x)}{\sigma(\cos\theta'_\ell > x) + \sigma(\cos\theta'_\ell < x)}\,. \tag{6.16}$$

From Fig. 6.7, one can see that when x is about -0.5 $A(x)$ will be most sensitive to the chirality of the coupling. Table 6.4 shows the asymmetry $A(-0.5)$ for models i–iv with two choices of the masses m_Y and m_X. The usefulness of $A(-0.5)$ for the determination of the coupling is enhanced by its relative insensitivity to the spin and mass combinations.

[2]A more realistic simulation at the level of the previous section, including parton showering and signal selection cuts, would require the modification of Pythia to include top-quark spin correlation effects, which I have not attempted to carry out.

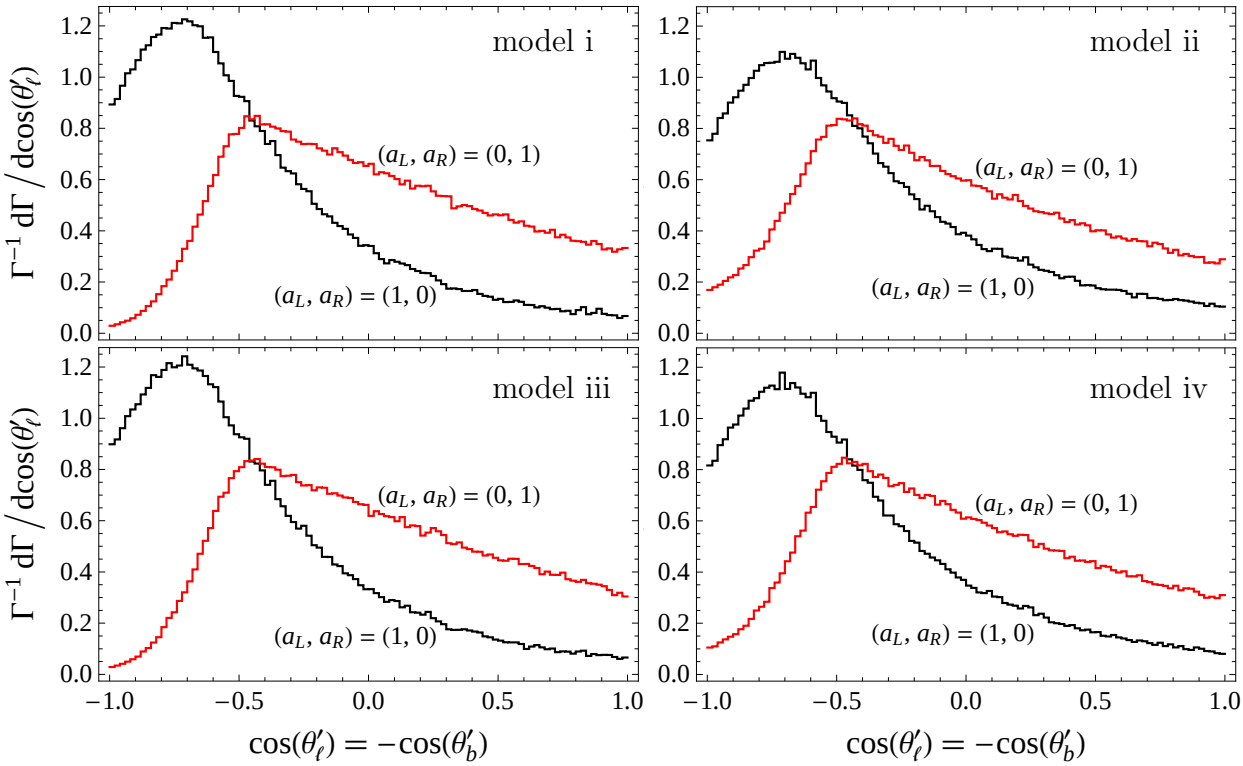

Figure 6.7: *Parton-level angular distribution of the top-quark decay products in the $b\ell$ rest frame, for the decay chain $Y \to Xt \to Xb\ell^+\nu$. The four panels show the results for the four scenarios in Table 6.1, for the two coupling choice $a_L = 1$, $a_R = 0$ (black) and $a_L = 0$, $a_R = 1$ (red). The input mass parameters are $m_Y = 400$ GeV and $m_X = 10$ GeV. The distributions have been normalized to unity.*

	$m_Y = 400$ GeV, $m_X = 10$ GeV				$m_Y = 300$ GeV, $m_X = 100$ GeV			
	Model				Model			
a_L, a_R	i	ii	iii	iv	i	ii	iii	iv
1, 0	−0.10	0.02	−0.10	−0.03	0	0.15	0.04	0.10
0, 1	0.68	0.55	0.68	0.61	0.54	0.39	0.50	0.45
1, 1	0.29	0.28	0.29	0.29	0.28	0.27	0.28	0.27

Table 6.4: *Asymmetry $A(-0.5)$ for models i–iv and two choices of the masses m_Y and m_X.*

6.7 Conclusions

The SM-like Higgs boson has been observed at the LHC with a relatively light mass of about 125 GeV. The "naturalness" argument of the Higgs sector suggests the existence of partners of the SM particles, especially the heavy top quark. The top quark may

thus hold the key to new physics associated with the electroweak symmetry-breaking sector, because of its enhanced coupling to the Higgs sector. In this chapter, I have systematically categorized the generic interactions of a new particle that couples to the top quark and a stable neutral particle, which serves as a candidate for cold dark matter. I have considered all possible assignments of spin 0, $\frac{1}{2}$ and 1 for either of the two new particles.

In the search for new physics involving top quarks and its partners at the LHC, the experimental signatures may be distinctive, but challenging to disentangle. Pair production of the massive top partners leads to a signature of a $t\bar{t}$ pair plus missing energy, which is difficult to separate from the large SM $t\bar{t}$ background. I have presented a set of optimized selection cuts for isolating this new physics signal at the 8 and 14 TeV runs of the LHC. I have found that, at 14 TeV with an integrated luminosity of 100 fb^{-1}, a spin-zero top partner can be observed at the 5σ level up to a mass of 675 GeV, while for a spin-$\frac{1}{2}$ top partner the reach extends to 945 GeV.

If a process of this type is discovered at the LHC, it will be imperative to determine the spins and couplings of the new particles, in order to understand the underlying physics mechanism. I have proposed a strategy to extract these properties from experimental data by means of suitable differential distributions of the final-state products. With this approach, a spin-0 top partner with mass of about 300 GeV can be discriminated from spin-$\frac{1}{2}$ and spin-1 particles at the 5σ level with a luminosity of 10 fb^{-1} at 14 TeV. Furthermore, the structure of the coupling that mediates the decay of the top partner into a top quark and a massive neutral particle can be analyzed by measurement of the polarization of the final-state top quarks. This method allows one to distinguish clearly between left-handed, right-handed, and vector couplings. Most importantly, the proposed observables for spin and coupling determination are insensitive to unknown branching fractions and depend only mildly on the masses of the new particles.

In conclusion, the LHC will allow us to observe and study top partners with mass up to about 1 TeV. This program will shed light on the interplay of the Higgs-boson and top-quark sectors and may elucidate the concept of naturalness.

Appendix A

Model cross sections

The following table lists the tree-level parton-level production cross sections σ_{prod} for the process $pp \to Y^+Y^- \to \ell^+\ell^- X^0 \bar{X}^0$ ($\ell = e, \mu$), for the 11 independent combinations from Tab. 4.1. Also shown are the measurable cross sections σ_{meas} after inclusion of detector effects and the cuts in eq. (4.9). The cross sections have been computed with CompHEP.

Combination	σ_{prod} [fb]	σ_{meas} [fb]
1	3.62	1.45
2	8.50	3.36
3	9.65	3.11
4	41.4	11.45
5	41.4	11.70
6	41.4	14.05
7	89.6	25.0
8	29.9	8.47
9	89.6	31.4
10	112	31.2
11 [$M_{\hat{Q}}$=0.5 TeV]	179	48.3
11 [$M_{\hat{Q}}$=1 TeV]	445	137

Appendix B

Sample supersymmetry scenarios

In supersymmetric models, large regions of parameter space can lead to sizeable branching fractions for the decay chain in Fig. 5.1. Here two explicit examples are given, one involving a dominant contribution from the exchange of a new-physics particle B in the three-body decay, and a second where the decay is dominantly mediated by the Z boson. The branching fractions have been calculated with the program SUSY-HIT [58].

a) $A = \tilde{\chi}_1^0, \quad B = \tilde{e}_L, \tilde{\mu}_L, \quad C = \tilde{\chi}_2^0, \quad D = \tilde{q}_L$
$M_1 = 102$ GeV, $\quad M_2 = 192$ GeV, $\quad \mu = 435$ GeV, $\quad \tan\beta = 3$,
$m_{\tilde{\chi}_1^0} = 96$ GeV, $\quad m_{\tilde{\chi}_2^0} = 181$ GeV,
$m_{\tilde{e}_R} = m_{\tilde{e}_R} = 197$ GeV $\approx m_{\tilde{\tau}_1}$, $\quad m_{\tilde{e}_L} = m_{\tilde{e}_L} = 242$ GeV $\approx m_{\tilde{\tau}_2}$, $\quad \tilde{q}_L = 570$ GeV;

$\mathrm{BR}[\tilde{\chi}_2^0 \to e^+e^-\tilde{\chi}_1^0] = \mathrm{BR}[\tilde{\chi}_2^0 \to \mu^+\mu^-\tilde{\chi}_1^0] = 9.7\%, \qquad \mathrm{BR}[\tilde{q}_L \to q\tilde{\chi}_2^0] = 33\%$

b) $A = \tilde{\chi}_1^0, \quad B = \tilde{e}_L, \tilde{\mu}_L, \quad C = \tilde{\chi}_2^0, \quad D = \tilde{q}_L$
$M_1 = 95$ GeV, $\quad M_2 = 179$ GeV, $\quad \mu = 547$ GeV, $\quad \tan\beta = 10$,
$m_{\tilde{\chi}_1^0} = 94$ GeV, $\quad m_{\tilde{\chi}_2^0} = 182$ GeV,
$m_{\tilde{e}_R} = m_{\tilde{e}_R} = 500$ GeV $\approx m_{\tilde{\tau}_1}$, $\quad m_{\tilde{e}_L} = m_{\tilde{e}_L} = 510$ GeV $\approx m_{\tilde{\tau}_2}$, $\quad \tilde{q}_L = 570$ GeV;

$\mathrm{BR}[\tilde{\chi}_2^0 \to e^+e^-\tilde{\chi}_1^0] = \mathrm{BR}[\tilde{\chi}_2^0 \to \mu^+\mu^-\tilde{\chi}_1^0] = 2.7\%, \qquad \mathrm{BR}[\tilde{q}_L \to q\tilde{\chi}_2^0] = 33\%$

Appendix C

Formulae for invariant-mass distributions

Explicit expressions for the functions $f_i^{(\ell\ell)}$ and $f_i^{(j\ell)}$ are available in MATHEMATICA format at `http://www.pitt.edu/~afreitas/dec3.tgz`. Note that the expressions in this file are not normalized, since in practice the normalization is best carried out numerically as described in section 5.3.1. The results for $f_i^{(\ell\ell)}$ are given as analytical formulae, while $f_i^{(j\ell)}$ are presented in terms of one-dimensional integral representations of the form

$$f_i^{(j\ell)} = \int_{m_A^2}^{m_C^2[1-m_{q\ell^+}^2/(m_D^2-m_C^2)]} dm_{A\ell^-}^2 \, F_i^{(j\ell)}. \tag{C.1}$$

Bibliography

[1] J. L. Hewett, H. Weerts, R. Brock, J. N. Butler, B. C. K. Casey, J. Collar, A. de Govea and R. Essig *et al.*, arXiv:1205.2671 [hep-ex].

[2] P. Nath, B. D. Nelson, H. Davoudiasl, B. Dutta, D. Feldman, Z. Liu, T. Han and P. Langacker *et al.*, Nucl. Phys. Proc. Suppl. **200-202**, 185 (2010) [arXiv:1001.2693 [hep-ph]];
G. L. Bayatian *et al.* [CMS Collaboration], J. Phys. G **34**, 995 (2007);
G. Aad *et al.* [ATLAS Collaboration], arXiv:0901.0512 [hep-ex].

[3] R Davis Jr., Phys. Rev. Lett. **12**, 303-305 (1964)

[4] Y. Fukuda *et al.* [Super-Kamiokande Collaboration], Phys. Rev. Lett. **82**, 2430 (1999) [hep-ex/9812011].

[5] Q. R. Ahmad *et al.* [SNO Collaboration], Phys. Rev. Lett. **87**, 071301 (2001) [nucl-ex/0106015]. Q. R. Ahmad *et al.* [SNO Collaboration], Phys. Rev. Lett. **89**, 011302 (2002) [nucl-ex/0204009].

[6] K. Abe *et al.* [T2K Collaboration], Phys. Rev. Lett. **107**, 041801 (2011) [arXiv:1106.2822 [hep-ex]].

[7] P. Adamson *et al.* [MINOS Collaboration], Phys. Rev. Lett. **107**, 181802 (2011) [arXiv:1108.0015 [hep-ex]].

[8] Y. Abe *et al.* [DOUBLE-CHOOZ Collaboration], Phys. Rev. Lett. **108**, 131801 (2012) [arXiv:1112.6353 [hep-ex]].

[9] F. P. An *et al.* [DAYA-BAY Collaboration], Phys. Rev. Lett. **108**, 171803 (2012) [arXiv:1203.1669 [hep-ex]].

[10] J. K. Ahn *et al.* [RENO Collaboration], Phys. Rev. Lett. **108**, 191802 (2012) [arXiv:1204.0626 [hep-ex]].

[11] C. G. Lester and D. J. Summers, Phys. Lett. B **463**, 99 (1999);
A. Barr, C. Lester and P. Stephens, J. Phys. G **29**, 2343 (2003).

[12] T. Appelquist, H. C. Cheng and B. A. Dobrescu, Phys. Rev. D **64**, 035002 (2001); B. A. Dobrescu and E. Pontón, JHEP **0403**, 071 (2004); G. Burdman, B. A. Dobrescu and E. Pontón, JHEP **0602**, 033 (2006).

[13] N. Arkani-Hamed, A. G. Cohen and H. Georgi, Phys. Lett. B **513**, 232 (2001) [hep-ph/0105239]; N. Arkani-Hamed, A. G. Cohen, E. Katz, A. E. Nelson, T. Gregoire and J. G. Wacker, JHEP **0208**, 021 (2002) [hep-ph/0206020]; N. Arkani-Hamed, A. G. Cohen, E. Katz and A. E. Nelson, JHEP **0207**, 034 (2002) [hep-ph/0206021]; I. Low, W. Skiba and D. Tucker-Smith, Phys. Rev. D **66**, 072001 (2002) [hep-ph/0207243]; D. E. Kaplan and M. Schmaltz, JHEP **0310**, 039 (2003) [hep-ph/0302049]; S. Chang and J. G. Wacker, Phys. Rev. D **69**, 035002 (2004) [hep-ph/0303001]; W. Skiba and J. Terning, Phys. Rev. D **68**, 075001 (2003) [hep-ph/0305302]; S. Chang, JHEP **0312**, 057 (2003) [hep-ph/0306034]; M. Schmaltz, JHEP **0408**, 056 (2004) [hep-ph/0407143].

[14] B. Abbott *et al.* [D0 Collaboration], Phys. Rev. D **60**, 052001 (1999); V. M. Abazov *et al.* [D0 Collaboration], Nature **429**, 638 (2004); A. Abulencia *et al.* [CDF Collaboration], Phys. Rev. D **74**, 032009 (2006); V. M. Abazov *et al.* [D0 Collaboration], Phys. Rev. D **78**, 012005 (2008); T. Aaltonen *et al.* [CDF Collaboration], Phys. Rev. Lett. **101**, 252001 (2008); F. Fiedler, A. Grohsjean, P. Haefner and P. Schieferdecker, Nucl. Instrum. Meth. A **624**, 203 (2010).

[15] L. Wolfenstein, Phys. Rev. Lett. **51**, 1945 (1983).

[16] S. R. Coleman and J. Mandula, Phys. Rev. **159**, 1251 (1967).

[17] D. I. Kazakov, hep-ph/0012288.

[18] S. Ferrara, L. Girardello and F. Palumbo, Phys. Rev. D **20**, 403 (1979).

[19] L. Girardello and M. T. Grisaru, Nucl. Phys. B **194**, 65 (1982).

[20] S. P. Martin, in "Perspectives on supersymmetry II," ed. G. L. Kane, World Scientifc, Singapore (2010), pp. 1–153 [hep-ph/9709356].

[21] B. C. Allanach, M. Battaglia, G. A. Blair, M. S. Carena, A. De Roeck, A. Dedes, A. Djouadi and D. Gerdes *et al.*, Eur. Phys. J. C **25**, 113 (2002) [hep-ph/0202233].

[22] T. Appelquist, B. A. Dobrescu, E. Ponton and H. U. Yee, Phys. Rev. Lett. **87**, 181802 (2001) [arXiv:hep-ph/0107056].

[23] B. A. Dobrescu and E. Poppitz, Phys. Rev. Lett. **87**, 031801 (2001) [arXiv:hep-ph/0102010].

[24] E. Ma, Phys. Rev. D **70**, 031901 (2004) [hep-ph/0404199]. S. Dev, R. R. Gautam and L. Singh, Phys. Lett. B **708**, 284 (2012) [arXiv:1201.3755 [hep-ph]]. P. V. Dong, H. N. Long, C. H. Nam and V. V. Vien, Phys. Rev. D **85**, 053001 (2012) [arXiv:1111.6360 [hep-ph]]. G. -J. Ding, L. L. Everett and A. J. Stuart, Nucl. Phys. B **857**, 219 (2012) [arXiv:1110.1688 [hep-ph]]. L. L. Everett and A. J. Stuart, Phys. Lett. B **698**, 131 (2011) [arXiv:1011.4928 [hep-ph]]. S. Morisi and E. Peinado, Phys. Rev. D **80**, 113011 (2009) [arXiv:0910.4389 [hep-ph]].

[25] R. Jora, S. Nasri and J. Schechter, Int. J. Mod. Phys. A **21**, 5875 (2006) [arXiv:hep-ph/0605069] and references therein; O. Felix, A. Mondragon, M. Mondragon and E. Peinado, AIP Conf. Proc. **917**, 383 (2007) [Rev. Mex. Fis. **S52N4**, 67 (2006)] [arXiv:hep-ph/0610061]; S. L. Chen, M. Frigerio and E. Ma, Phys. Rev. D **70**, 073008 (2004) [Erratum-ibid. D **70**, 079905 (2004)] [arXiv:hep-ph/0404084]; W. Grimus and L. Lavoura, JHEP **0508**, 013 (2005) [arXiv:hep-ph/0504153]; R. N. Mohapatra, S. Nasri and H. B. Yu, Phys. Lett. B **639**, 318 (2006) [arXiv:hep-ph/0605020]; F. Caravaglios and S. Morisi, arXiv:hep-ph/0503234; H. Fritzsch and Z. z. Xing, Phys. Rev. D **61**, 073016 (2000) [arXiv:hep-ph/9909304]; M. Picariello, arXiv:hep-ph/0611189; N. Haba, A. Watanabe and K. Yoshioka, Phys. Rev. Lett. **97**, 041601 (2006) [arXiv:hep-ph/0603116].

[26] L. Wolfenstein, Phys. Rev. D **18**, 958 (1978).

[27] H. Fritzsch and Z. z. Xing, Phys. Lett. B **440**, 313 (1998) [arXiv:hep-ph/9808272]; X. G. He and A. Zee, Phys. Lett. B **560**, 87 (2003) [arXiv:hep-ph/0301092]; P. F. Harrison, D. H. Perkins and W. G. Scott, Phys. Lett. B **458**, 79 (1999) [arXiv:hep-ph/9904297]; P. F. Harrison, D. H. Perkins and W. G. Scott, Phys. Lett. B **530**, 167 (2002) [arXiv:hep-ph/0202074]; P. F. Harrison and W. G. Scott, Phys. Lett. B **557**, 76 (2003) [arXiv:hep-ph/0302025].

[28] E. Ma, Phys. Lett. B **632**, 352 (2006) [arXiv:hep-ph/0508231]; G. Altarelli, arXiv:0705.0860 [hep-ph]; W. Grimus and L. Lavoura, Phys. Lett. B **572**, 189 (2003) [arXiv:hep-ph/0305046]; K. A. Hochmuth, S. T. Petcov and W. Rodejohann, Phys. Lett. B **654**, 177 (2007) [arXiv:0706.2975 [hep-ph]]; Y. Koide and E. Takasugi, arXiv:0706.4373 [hep-ph]; W. Rodejohann and M. A. Schmidt, Phys. Atom. Nucl. **69**, 1833 (2006) [arXiv:hep-ph/0507300].

[29] M. C. Gonzalez-Garcia and M. Maltoni, arXiv:0704.1800 [hep-ph].

[30] S. Hannestad and G. G. Raffelt, JCAP **0611**, 016 (2006) [arXiv:astro-ph/0607101]; M. Fukugita, K. Ichikawa, M. Kawasaki and O. Lahav, Phys. Rev. D **74**, 027302 (2006) [arXiv:astro-ph/0605362]; U. Seljak, A. Slosar and P. McDonald, JCAP **0610**, 014 (2006) [arXiv:astro-ph/0604335]; A. Goobar, S. Hannestad, E. Mortsell and H. Tu, JCAP **0606**, 019 (2006) [arXiv:astro-ph/0602155].

[31] B. C. Chauhan, M. Picariello, J. Pulido and E. Torrente-Lujan, Eur. Phys. J. C **50**, 573 (2007) [hep-ph/0605032]. K. A. Hochmuth, S. T. Petcov and W. Rodejohann, Phys. Lett. B **654**, 177 (2007) [arXiv:0706.2975 [hep-ph]]. Y. H. Ahn, H. -Y. Cheng and S. Oh, arXiv:1105.4460 [hep-ph].

[32] W. S. Cho, K. Choi, Y. G. Kim and C. B. Park, Phys. Rev. Lett. **100**, 171801 (2008);
A. J. Barr, B. Gripaios and C. G. Lester, JHEP **0802**, 014 (2008);
W. S. Cho, K. Choi, Y. G. Kim and C. B. Park, JHEP **0802**, 035 (2008);
D. R. Tovey, JHEP **0804**, 034 (2008);
H. C. Cheng and Z. Han, JHEP **0812**, 063 (2008);
A. J. Barr, B. Gripaios and C. G. Lester, JHEP **0911**, 096 (2009).

[33] G. Polesello and D. R. Tovey, JHEP **1003**, 030 (2010);
K. T. Matchev and M. Park, arXiv:0910.1584 [hep-ph];
P. Konar, K. Kong, K. T. Matchev and M. Park, Phys. Rev. Lett. **105**, 051802 (2010);
T. Cohen, E. Kuflik and K. M. Zurek, JHEP **1011**, 008 (2010).

[34] J. Alwall, A. Freitas and O. Mattelaer, AIP Conf. Proc. **1200**, 442 (2010);
P. Artoisenet, V. Lemaitre, F. Maltoni and O. Mattelaer, arXiv:1007.3300 [hep-ph];
J. Alwall, A. Freitas and O. Mattelaer, in preparation.

[35] W. S. Cho, K. Choi, Y. G. Kim and C. B. Park, Phys. Rev. D **79**, 031701 (2009); D. Horton, arXiv:1006.0148 [hep-ph].

[36] M. R. Buckley, H. Murayama, W. Klemm and V. Rentala, Phys. Rev. D **78**, 014028 (2008);
M. R. Buckley, S. Y. Choi, K. Mawatari and H. Murayama, Phys. Lett. B **672**, 275 (2009).

[37] A. J. Barr, JHEP **0602**, 042 (2006) [arXiv:hep-ph/0511115].

[38] G. L. Kane, A. A. Petrov, J. Shao and L. T. Wang, J. Phys. G **37**, 045004 (2010).

[39] K. Kondo, J. Phys. Soc. Jap. **57**, 4126 (1988), J. Phys. Soc. Jap. **60**, 836 (1991); R. H. Dalitz and G. R. Goldstein, Phys. Rev. D **45**, 1531 (1992).

[40] E. Boos *et al.* [CompHEP Collaboration], Nucl. Instrum. Meth. A **534**, 250 (2004).

[41] S. Schael *et al.*, Phys. Rept. **427**, 257 (2006).

[42] T. Sjöstrand, S. Mrenna and P. Z. Skands, JHEP **0605**, 026 (2006).

[43] J. Conway, PGS 4, http://www.physics.ucdavis.edu/~conway/research/software/pgs/pgs4-general.htm.

[44] C. Athanasiou, C. G. Lester, J. M. Smillie, B. R. Webber, JHEP **0608**, 055 (2006);
J. M. Smillie, Eur. Phys. J. **C51**, 933-943 (2007).

[45] M. Burns, K. Kong, K. T. Matchev, M. Park, JHEP **0810**, 081 (2008).

[46] C.-Y. Chen, A. Freitas, JHEP **1102**, 002 (2011).

[47] T. Han, I. Lewis, Z. Liu, JHEP **1012**, 085 (2010);
J. Andrea, B. Fuks, F. Maltoni, arXiv:1106.6199 [hep-ph];
J. Kumar, A. Rajaraman, B. Thomas, arXiv:1108.3333 [hep-ph];
B. Grinstein, A. L. Kagan, M. Trott, J. Zupan, arXiv:1108.4027 [hep-ph].

[48] I. Hinchliffe, F. E. Paige, M. D. Shapiro, J. Soderqvist, W. Yao, Phys. Rev. **D55**, 5520-5540 (1997).

[49] B. K. Gjelsten, D. J. Miller, P. Osland, JHEP **0412**, 003 (2004).

[50] B. C. Allanach, C. G. Lester, M. A. Parker, B. R. Webber, JHEP **0009**, 004 (2000);
K. Kawagoe, M. M. Nojiri, G. Polesello, Phys. Rev. **D71**, 035008 (2005);
B. K. Gjelsten, D. J. Miller, P. Osland, JHEP **0506**, 015 (2005).

[51] A. J. Barr, Phys. Lett. **B596**, 205-212 (2004);
J. M. Smillie, B. R. Webber, JHEP **0510**, 069 (2005);
A. Alves, O. Eboli, T. Plehn, Phys. Rev. **D74**, 095010 (2006);
L.-T. Wang, I. Yavin, JHEP **0704**, 032 (2007);
C. Kilic, L.-T. Wang, I. Yavin, JHEP **0705**, 052 (2007);
W. Ehrenfeld, A. Freitas, A. Landwehr, D. Wyler, JHEP **0907**, 056 (2009).

[52] D. J. Miller, P. Osland, A. R. Raklev, JHEP **0603**, 034 (2006).

[53] C. Csaki, J. Heinonen, M. Perelstein, JHEP **0710**, 107 (2007).

[54] L. Edelhäuser, W. Porod, R. K. Singh, JHEP **1008**, 053 (2010).

[55] J. Alcaraz *et al.* [ALEPH and DELPHI and L3 and OPAL and LEP Electroweak Working Group Collaborations], hep-ex/0612034.

[56] S. Y. Choi, M. Drees, A. Freitas, P. M. Zerwas, Phys. Rev. **D78**, 095007 (2008);
S. Y. Choi, D. Choudhury, A. Freitas, J. Kalinowski, J. M. Kim, P. M. Zerwas, JHEP **1008**, 025 (2010).

[57] B. K. Gjelsten *et al.*, in G. Weiglein *et al.* [LHC/LC Study Group Collaboration], Phys. Rept. **426**, 47-358 (2006).

[58] A. Djouadi, M. M. Mühlleitner, M. Spira, Acta Phys. Polon. B **38**, 635 (2007).

[59] J. Incandela [for the CMS Collaboration] and F. Gianotti [for the ATLAS Collaboration], talks at CERN LHC seminar, July 4, 2012 [`http://indico.cern.ch/event/197461`].

[60] G. F. Giudice, in "Perspectives on LHC physics," eds. G. Kane, A. Pierce, 155–178 [arXiv:0801.2562 [hep-ph]].

[61] P. Meade and M. Reece, Phys. Rev. D **74**, 015010 (2006).

[62] T. Han, R. Mahbubani, D. G. E. Walker and L. T. E. Wang, JHEP **0905**, 117 (2009).

[63] T. Plehn, M. Spannowsky, M. Takeuchi and D. Zerwas, JHEP **1010**, 078 (2010); T. Plehn, M. Spannowsky and M. Takeuchi, JHEP **1105**, 135 (2011).

[64] Y. Bai, H.-C. Cheng, J. Gallicchio and J. Gu, arXiv:1203.4813 [hep-ph];
D. S. M. Alves, M. R. Buckley, P. J. Fox, J. D. Lykken and C. -T. Yu, arXiv:1205.5805 [hep-ph];
Z. Han, A. Katz, D. Krohn and M. Reece, arXiv:1205.5808 [hep-ph];
D. E. Kaplan, K. Rehermann and D. Stolarski, arXiv:1205.5816 [hep-ph].

[65] T. Plehn, M. Spannowsky and M. Takeuchi, arXiv:1205.2696 [hep-ph].

[66] J. Cao, C. Han, L. Wu, J. M. Yang and Y. Zhang, arXiv:1206.3865 [hep-ph].

[67] B. Dutta, T. Kamon, N. Kolev, K. Sinha and K. Wang, arXiv:1207.1873 [hep-ph].

[68] H. Cai, H.-C. Cheng and J. Terning, Phys. Rev. Lett. **101**, 171805 (2008).

[69] J. Pumplin, D. R. Stump, J. Huston, H. L. Lai, P. M. Nadolsky and W. K. Tung, JHEP **0207**, 012 (2002).

[70] W. Beenakker, S. Brensing, M. Krämer, A. Kulesza, E. Laenen and I. Niessen, JHEP **1008**, 098 (2010).

[71] M. Cacciari, M. Czakon, M. L. Mangano, A. Mitov and P. Nason, Phys. Lett. B **710**, 612 (2012).

[72] T. Aaltonen *et al.* [CDF Collaboration], Phys. Rev. Lett. **106**, 191801 (2011).

[73] V. M. Abazov *et al.* [D0 Collaboration], Phys. Lett. B **693**, 95 (2010);
M. S. Carena, J. Hubisz, M. Perelstein and P. Verdier, Phys. Rev. D **75**, 091701 (2007).

[74] G. Aad *et al.* [ATLAS Collaboration], Phys. Rev. Lett. **108**, 041805 (2012).

[75] G. Aad *et al.* [ATLAS Collaboration], ATLAS-CONF-2012-071;
G. Aad *et al.* [ATLAS Collaboration], ATLAS-CONF-2012-073;
G. Aad *et al.* [ATLAS Collaboration], ATLAS-CONF-2012-074.

[76] S. Sharma [for the CMS Collaboration], talk at the 36th International Conference for High Energy Physics (ICHEP 2012), Melbourne, Australia, 4–11 July 2012;
C. Rogan [for the CMS Collaboration], talk at the 36th International Conference for High Energy Physics (ICHEP 2012), Melbourne, Australia, 4–11 July 2012.

[77] R. Essig, E. Izaguirre, J. Kaplan and J. G. Wacker, JHEP **1201**, 074 (2012);
Y. Kats, P. Meade, M. Reece and D. Shih, JHEP **1202**, 115 (2012);
M. Papucci, J. T. Ruderman and A. Weiler, arXiv:1110.6926 [hep-ph];
X.-J. Bi, Q.-S. Yan and P.-F. Yin, Phys. Rev. D **85**, 035005 (2012);
C. Brust, A. Katz, S. Lawrence and R. Sundrum, JHEP **1203**, 103 (2012);
N. Desai and B. Mukhopadhyaya, JHEP **1205**, 057 (2012);
A. Choudhury and A. Datta, arXiv:1207.1846 [hep-ph].

[78] A. Lazopoulos, T. McElmurry, K. Melnikov and F. Petriello, Phys. Lett. B **666**, 62 (2008);
A. Kardos, Z. Trocsanyi and C. Papadopoulos, Phys. Rev. D **85**, 054015 (2012);
M. V. Garzelli, A. Kardos, C. G. Papadopoulos and Z. Trocsanyi, Phys. Rev. D **85**, 074022 (2012).

[79] M. Beneke, P. Falgari, S. Klein and C. Schwinn, Nucl. Phys. **B855**, 695 (2012).

[80] G. Aad *et al.* [ATLAS Collaboration], arXiv:1205.2067 [hep-ex].

[81] A. Pukhov, hep-ph/0412191;
A. Pukhov, A. Belyaev, N. Christensen,
`http://theory.sinp.msu.ru/~pukhov/calchep.html`.

[82] For an overview, see
sect. 4 in A. J. Barr and C. G. Lester, J. Phys. G **37**, 123001 (2010), and refs. therein;
sect. X in A. J. Barr, T. J. Khoo, P. Konar, K. Kong, C. G. Lester, K. T. Matchev and M. Park, Phys. Rev. D **84**, 095031 (2011), and refs. therein.

[83] P. Konar, K. Kong, K. T. Matchev and M. Park, Phys. Rev. Lett. **105**, 051802 (2010);
T. Cohen, E. Kuflik and K. M. Zurek, JHEP **1011**, 008 (2010).

[84] T. Han, I. -W. Kim and J. Song, Phys. Lett. B **693**, 575 (2010); arXiv:1206.5633 [hep-ph]; arXiv:1206.5641 [hep-ph].